Fe-based bulk metallic glasses: alloy optimization, focused on understanding the influences of impurities on the glass formation

Thesis by Assoc. Prof. Dr. Mihai Stoica

Politehnica University Timisoara, Romania

and

Institute for Complex Materials (IKM) at the Leibniz Institute for Solid State and Materials Research (IFW) Dresden, Germany

Submitted in partial fulfillment of the requirements for the Habilitation degree

Politehnica University Timisoara, Romania

2015

Thesis abstract

The actual habilitation thesis is a part of an extended research project conducted and performed by the author- and therefore the Leibniz Institute for Solid State and Materials Research (IFW) Dresden, Germany- for OCAS N.V. Zelzate, Belgium. OCAS (Onderzoeks Centrum voor de Aanwending van Staal, ArcelorMittal Global R&D Gent) is an advanced, market-oriented research center for steel applications. Based in Belgium, it is a joint venture between the Flemish Region and ArcelorMittal, the world's largest steel group.

The work is dedicated to the Fe-based bulk metallic glasses (BMGs). Generally, the BMGs establish a new class of advanced materials with amazing properties, discovered around 1988, and they are metallic alloys with amorphous structure. Among them, the Fe-based BMGs were synthesized for the first time in 1995 and since then tremendous efforts were put to create new classes of amorphisable alloys. Despite their relatively complicated chemical compositions, the low price of the used elements, as well as the possibility to use industrial pre-alloys, make the Fe-based BMGs very attractive for industrial application. Therefore, a clear image of what may affect the glass-forming ability (GFA) of these BMGs with the emphasis on the impurities which may be present in the master alloy is strongly required.

The thesis is structured in 7 Chapters and starts with theoretical consideration about metallic glasses. There the basic thermodynamical and kinetic aspects of the glass formation are presented, together with the historical development of BMGs in general and Fe-based BMGs in particular.

Chapter 2 presents the methodology and the model alloys chosen for investigations, as well as the strategy for assessing the GFA and the role of impurities. This must be done by corroborating experimental data obtained upon several types of investigations: differential scanning calorimetry, X-ray diffraction (room temperature and *in-situ* upon heating), magnetic measurements, high-resolution transmission electron microscopy (HR-TEM). As starting alloys $[(Fe_{0.5}Co_{0.5})_{0.75}B_{0.2}Si_{0.05}]_{96}Nb_4$ and $Fe_{74}Mo_4P_{10}C_{7.5}B_{2.5}Si_2$ (at.%) were chosen. Further, it is proposed to assess the role of Yttrium additions (because it was shown in literature that Yttrium may enhance the GFA by acting- eventually- as an oxygen scavenger and, because of its big atomic radius, frustrating further the formation of the crystalline network). Following the route

used to design the FeCoBSiNb BMGs, the brand new $(Fe_{77.5}P_{12.5}C_{10})_{96}Nb_4$ and $[(Fe_{0.9}Co_{0.1})_{77.5}P_{12.5}C_{10}]_{96}Nb_4$ compositions are proposed as well.

Chapter 3 describes in details the experiments and their particularities, showing pictures of actually used devices. A consistent part is dedicated to the X-ray diffraction in transmission configuration using high intensity high-energy monochromatic synchrotron radiation, research field in which the author was a pioneer and has numerous highly cited contributions.

The experimental results are presented starting with Chapter 4. Here it is shown that in the case of $[(Fe_{0.5}Co_{0.5})_{0.75}B_{0.2}Si_{0.05}]_{96}Nb_4$, 8 dissimilar master alloys (plus few additional ones, but with ingredients and techniques as before) were prepared using different elements and pre-alloys. Their chemical composition, as well as the composition of the used pre-alloys, was analyzed. The actual chemical compositions of all master alloys are very close to the target composition, but the small deviations affect in different ways the results. Upon experimental assessment of the maximum rod diameter achievable by copper mold injection casting it is concluded that the alloy with the best GFA is the one made using pure elements. The thermal and magnetic behavior of several as-cast samples are presented in the very last details and the results are discussed in regard with the real chemical composition of the used master alloys.

The influence of Yttrium additions is discussed as well in Chapter 4. Despite the data presented in literature, it is concluded that in this actual case the Yttrium does not enhance the GFA. Then the influence of the casting atmosphere is evaluated. The casting experiments upon which the best results were obtained took place when the casting atmosphere was not very clean, i.e. by casting in air. The content of Oxygen and Nitrogen in selected samples were analyzed. Interesting, both Oxygen and Nitrogen content have a descendent trend as the partial air pressure in the casting chamber increases and the lowest values were found in the samples cast in air. However, there is no evident trend regarding the amorphicity and the Oxygen or Nitrogen content.

The studies of the $[(Fe_{0.5}Co_{0.5})_{0.75}B_{0.2}Si_{0.05}]_{96}Nb_4$ BMGs are continued in Chapter 5. There the time-resolved XRD and crystallization behavior is presented. By using the Kissinger approach, as well as the Johnson-Mehl-Avrami (JMA) plots, it was found that the activation energy for crystallization is around 536 kJ/mol, which is very high and therefore indicates a good thermal stability against crystallization. Also, the

Avrami exponent takes the average value of 1.43. Together with a short incubation time (i.e. less than one minute) it is concluded that the glassy samples crystallize through a primary crystallization reaction and the mechanism is athermal and diffusion controlled. These findings are proved further by the XRD studies and the primary phase which forms there is of the $Fe_{23}B_6$-type having an fcc-like structure and with a large lattice parameter of about 1.2 nm, including 96 atoms in its volume unit. Further it is seen that the as-cast BMGs may contain small nuclei, which do not affect the macroscopic properties. When the $[(Fe_{0.5}Co_{0.5})_{0.75}B_{0.2}Si_{0.05}]_{96}Nb_4$ samples do not become fully amorphous upon copper mold casting, the crystalline phases which form there are the equilibrium phases, not the metastable $Fe_{23}B_6$-type. Therefore, the foreign elements which may deteriorate GFA are those that stabilize the corresponding equilibrium crystalline phases.

The other model alloy, $Fe_{74}Mo_4P_{10}C_{7.5}B_{2.5}Si_2$, is analyzed in Chapter 6. 11 different master alloys were prepared using diverse combination of ingredients, pure elements and ferroalloys. The GFA of all master alloys was evaluated from experimental point of view and a ranking was established. This time the purity of the used ingredients does not play a very important role. Moreover, the master alloy needs a small content of foreign elements in order to retain the glassy state at room temperature, as for example Manganese. These important findings were patented, details are given in: Nele Van Steenberge, Daniel Ruiz-Romera, Mihai Stoica, Uta Kühn and Jürgen Eckert, world patent WO 2013087627 A1 or European patent EP2791376A1.

As for the FeCoBSiNb alloy, also in this case the detailed DSC and XRD analyses are presented. The crystallization behavior of $Fe_{74}Mo_4P_{10}C_{7.5}B_{2.5}Si_2$ BMGs is much more complicated as the one find for $[(Fe_{0.5}Co_{0.5})_{0.75}B_{0.2}Si_{0.05}]_{96}Nb_4$ BMGs. Due to the complexity of crystallization, data from magnetic measurements were put together with the DSC and XRD results. Finally, it was found that the initially fully amorphous sample crystallizes through several exothermic events, forming first fcc γ-Fe, together with Mo-P, Mo-C, Mo-B and/or Mo-Si. The residual amorphous matrix crystallizes then through the formation of $(Fe,Mo)_3P$, which will coexist with already formed Mo-P, Mo-C, Mo-B and/or Mo-Si. At the end the fcc γ-Fe will transform in bcc α-Fe (event clearly visible upon thermomagnetic measurements), the $(Fe,Mo)_3P$ will be depleted in Mo, some $Fe_{23}B_6$ forms (consuming Fe from its γ phase) plus whatever quantities of Mo-P, Mo-C, Mo-B and/or Mo-Si.

Transferring the knowledge accumulated by studying the role of the impurities on the glass-formation in the case of $[(Fe_{0.5}Co_{0.5})_{0.75}B_{0.2}Si_{0.05}]_{96}Nb_4$ and $Fe_{74}Mo_4P_{10}C_{7.5}B_{2.5}Si_2$ alloys, two new BMG forming alloy compositions were designed: $(Fe_{77.5}P_{12.5}C_{10})_{96}Nb_4$ and $[(Fe_{0.9}Co_{0.1})_{77.5}P_{12.5}C_{10}]_{96}Nb_4$. The master alloys are prone to form NbC and this was seen in few cases. However, after optimization of the fabrication procedure, as well as by partial substitution of Fe with Co, the amount and the dimensions of the intermetallic NbC is drastically reduced. Therefore, the master alloy should be made in two steps: eutectic 25Fe 75Nb (wt.%) by arc-melting and then FeP pre-alloy together with pure Co, eutectic FeNb and graphite particles can be melt in induction furnace. As a possible development toward industrial up-scaling, the industrially known procedure of arc melting with a consumable graphite electrode may be used. In this way a higher amount of Carbon can be alloyed and the formation of carbides could be avoided.

Rezumatul tezei

Conţinutul acestei Teze de Abilitare a rezultat în urma unui proiect de cercetare condus şi executat de autor- şi prin extensie de Institutul Leibniz de Cercetare a Fizicii Corpului Solid şi a Materialelor (IFW) din Dresda, Germania, pentru OCAS N.V. Zelzate, Belgia. OCAS (Onderzoeks Centrum voor de Aanwending van Staal, ArcelorMittal Global R&D Gent) este un centru avansat de cercetare în domeniul aplicaţiilor pentru oţel, orientat către piaţa de consum. Situat în Belgia, OCAS este o societate mixtă dintre Regiunea Flamandă şi ArcelorMittal, cel mai mare producător de oţel din lume.

Teza este dedicată sticlelor metalice masive care au în compoziţie ca element principal fierul. În general, sticlele metalice masive stabilesc o nouă clasă de materiale avansate cu proprietăţi deosebite. Ele au fost descoperite în 1988 şi sunt în esenţă aliaje metalice cu structură amorfă. Dintre ele, cele cu fier ca element majoritar au fost create pentru prima oară în 1995 şi din acel moment eforturi mari au fost canalizate către creerea de noi clase de aliaje amorfizabile. În ciuda compoziţiilor chimice complicate, totuşi preţul mic al elementelor folosite precum şi posibilităţile folosirii prealiajelor industriale fac sticlele metalice masive cu fier ca element majoritar foarte atractive pentru aplicaţii industriale. Ca urmare este imperios necesară o imagine clară a ceea ce le poate afecta abilitatea de vitrificare, cu accentul pe impurităţile care pot fi prezente în aliajul primar.

Teza de faţă este structurată în 7 capitole şi se deschide cu consideraţii teoretice despre sticlele metalice. În acest capitol sunt prezentate în special aspectele termodinamice şi cinetice fundamentale ale tranziţiei vitroase. Mai departe este prezentată dezvoltarea cronologică a sticlelor metalice masive, cu accentul pe cele care conţin fier ca element majoritar.

Capitolul 2 prezintă metodologia şi aliajele model alese pentru investigaţiile ulterioare, precum şi strategia de evaluare a abilităţii de tranziţie vitroasă şi a rolului impurităţilor. Aceasta trebuie facută prin coroborarea datelor experimentale obţinute în urma mai multor investigaţii: calorimetria diferenţială, difracţia de radiaţii X (la temperatura camerei precum şi *in-situ* în timpul încălzirii), măsuratori magnetice, microscopie electronică (în transmisie) de înaltă rezoluţie. Ca punct de plecare au fost alese aliajele $[(Fe_{0.5}Co_{0.5})_{0.75}B_{0.2}Si_{0.05}]_{96}Nb_4$ şi $Fe_{74}Mo_4P_{10}C_{7.5}B_{2.5}Si_2$ (compoziţia este exprimată în procente atomice). Mai departe este propusă evaluarea adiţiilor de ytrium

(pentru că în literatură a fost deja arătat că ytriumul poate să crească abilitatea de tranziţie vitroasă, fie datorită efectului de asanare al oxigenului din aliajul primar, fie datorită faptului că raza lui atomică mare nu îl face dorit în reţeaua cristalină). Mergând pe drumul urmat pentru creerea sticlelor metalice masive FeCoBSiNb, au fost sintetizate noi aliaje cu compoziţiile chimice $(Fe_{77.5}P_{12.5}C_{10})_{96}Nb_4$ şi $[(Fe_{0.9}Co_{0.1})_{77.5}P_{12.5}C_{10}]_{96}Nb_4$.

Capitolul 3 descrie în detaliu particularităţile experimentale, cu imagini ale instalaţiilor folosite. O parte consistentă e dedicată difracţiei de radiaţii X în transmisie folosind radiaţia monocromatică synchrotron, de intensitate şi energie înaltă. Acesta este un domeniu de cercetare în care autorul a fost pionier şi a publicat un număr consistent de lucrări ştiinţifice care atrag numeroase citări.

În capitolul 4 se discută despre turnarea a 8 aliaje primare diferite (plus alte câteva similare, când cantitatea iniţială nu a fost deajuns pentru turnările de probe amorfe ulterioare) având compoziţia ţintă $[(Fe_{0.5}Co_{0.5})_{0.75}B_{0.2}Si_{0.05}]_{96}Nb_4$. Compoziţia lor chimică reală, precum şi a prealiajelor folosite, a fost analizată cu grijă. Compoziţia chimică reală a tuturor aliajelor primare nu este departe de cea ţintă, însă micile deviaţii afectează rezultatele în mod diferit. În urma evaluărilor experimentale a diametrului maxim al unei bare ce se poate obţine prin turnarea aliajului primar în cochilă de cupru s-a ajuns la concluzia că aliajul cu cea mai mare abilitate de tranziţie vitroasă este cel fabricat numai din elemente pure. În continuare este prezentată în cele mai mici detalii comportarea termică şi magnetică a unora din probele turnate, iar rezultatele sunt discutate în raport cu compoziţia chimică reală a aliajului primar respectiv.

Tot în capitolul 4 este discutată si influenţa adiţiilor de ytrium asupra aliajului $[(Fe_{0.5}Co_{0.5})_{0.75}B_{0.2}Si_{0.05}]_{96}Nb_4$. În ciuda datelor prezentate în literatură, în cazul de faţă s-a gasit că ytriumul nu creşte abilitatea de tranziţie vitroasă. Apoi a fost evaluată influenţa atmosferei de turnare. S-a observat că cele mai bune rezultate s-au obţinut când atmosfera nu a fost foarte curată, mai precis după turnarea în aer. Apoi a fost analizat conţinutul de oxigen şi cel de azot în diferite probe. Atât conţinutul oxigenului cât şi cel al azotului tind să descrească pe măsură ce presiunea parţială de aer creşte în camera de turnare. Oricum, nu a fost observată o legatură clară între amorficitate şi conţinutul de oxigen sau azot din probe.

Studiile sticlelor metalice masive $[(Fe_{0.5}Co_{0.5})_{0.75}B_{0.2}Si_{0.05}]_{96}Nb_4$ continuă în capitolul 5. Aici se prezintă datele culese în urma difracţiei de radiaţii X în funcţie de temperatură, precum şi modul de cristalizare. Prin folosirea teoriei lui Kissinger, ca şi

prin studiul curbelor Johnson-Mehl-Avrami, s-a gasit că energia de activare pentru cristalizare este de 536 kJ/mol. Aceasta este o valoare relativ mare şi ca urmare indică o stabilitate termică ridicată a aliajului amorf. De asemenea, exponentul Avrami ia valoarea 1.43. Împreună cu un timp de incubaţie scurt (mai puţin de un minut) se concluzionează că probele amorfe cristalizează în urma unei reacţii primare cu mecanism atermic şi controlat de difuzie. Aceste rezultate sunt confirmate în continuare de studiile de difracţie. Astfel s-a găsit că faza primară cristalizată care se formează este de tipul $Fe_{23}B_6$ şi are o structură similară cubului centrat pe feţe. Parametrul laticei este aproximativ 1.2 nm şi are 96 de atomi în celula sa unitate. Mai departe se arată că imediat după preparare probele amorfe pot conţine chiar mici nuclee cristaline, dar care nu afectează proprietăţile macroscopice. Dacă probele din aliajul $[(Fe_{0.5}Co_{0.5})_{0.75}B_{0.2}Si_{0.05}]_{96}Nb_4$ nu se amorfizează complet în urma turnării, fazele cristaline care cresc în matricea amorfă sunt cele de echilibru şi nu metastabilul $Fe_{23}B_6$. Aşadar, elementele străine (impurităţile) care pot deteriora abilitatea de tranziţie vitroasă sunt de fapt cele care stabilizează fazele de echilibru corespunzătoare.

Cel de-al doilea aliaj model, $Fe_{74}Mo_4P_{10}C_{7.5}B_{2.5}Si_2$, este analizat în capitolul 6. În total au fost turnate 11 aliaje primare folosind diverse combinaţii de elemente pure şi feroaliaje. Abilitatea de tranziţie vitroasă a fost evaluată din punct de vedere experimental şi a fost stabilită o ierarhie între aliajele primare. De această dată s-a dovedit că puritatea elementelor folosite nu mai este aşa de importantă. Mai mult, acest aliaj are nevoie de elemente străine, precum manganul, pentru amorfizarea completă. Aceste rezultate importante au fost patentate, iar detalii se pot găsi în: Nele Van Steenberge, Daniel Ruiz-Romera, Mihai Stoica, Uta Kühn and Jürgen Eckert, patent internaţional WO 2013087627 A1 sau patent european EP2791376A1.

Precum pentru aliajul FeCoBSiNb şi în acest caz au fost făcute analize termice detaliate şi difracţie de radiaţii X. Modul de cristalizare al probelor masive amorfe din aliajul $Fe_{74}Mo_4P_{10}C_{7.5}B_{2.5}Si_2$ este mult mai complicat decât cel observat pentru probele amorfe $[(Fe_{0.5}Co_{0.5})_{0.75}B_{0.2}Si_{0.05}]_{96}Nb_4$. Din cauza complexităţii şi pentru a nu exista dubii, datele actuale au fost comparate cu datele culese în urma măsuratorilor magnetice. Aşadar s-a observat că probele complet amorfe cristalizează în mai mulţi paşi după cum urmează. Întâi se formează faza austenitică a fierului, împreună cu compuşi de tipul Mo-P, Mo-C, Mo-B şi/sau Mo-Si. Matricea reziduală amorfă cristalizează apoi prin formarea compusului $(Fe,Mo)_3P$, care coexistă cu cei descrişi mai înainte. La sfârşit, faza austenitică se transformă în ferită (eveniment observat cu

mare claritate în curbele termomagnetice), compusul $(Fe,Mo)_3P$ va fi sărăcit în Mo, e posibil să se formeze şi o fază de tipul $Fe_{23}B_6$ (având ca bază faza austenitică) plus ce mai rămâne din Mo-P, Mo-C, Mo-B şi/sau Mo-Si.

Transferând cunoştiinţele acumulate studiind rolul impurităţilor asupra abilităţii de tranziţie vitroasă în cazul aliajelor $[(Fe_{0.5}Co_{0.5})_{0.75}B_{0.2}Si_{0.05}]_{96}Nb_4$ şi $Fe_{74}Mo_4P_{10}C_{7.5}B_{2.5}Si_2$, au fost create două compoziţii noi (neprecizate în literatura de specialitate) care s-ar putea amorfiza, formând sticle metalice masive: $(Fe_{77.5}P_{12.5}C_{10})_{96}Nb_4$ şi $[(Fe_{0.9}Co_{0.1})_{77.5}P_{12.5}C_{10}]_{96}Nb_4$. Aliajele primare sunt susceptibile de a precipita NbC şi aceast aspect a fost observat în câteva cazuri. Oricum, după optimizarea procedurii de obţinere, precum şi prin substituţia parţială a fierului cu cobalt, cantitatea şi dimensiunile intermetalicului NbC a fost drastic redusă. Ca urmare s-a concluzionat că aliajul primar trebuie fabricat în doi paşi. Mai intâi eutecticul 25Fe75Nb (procente masice) trebuie obţinut prin topire în arc, iar după aceea cantităţile necesare de elemente pure, împreună cu un prealiaj FeP, se pot topi în inducţie. Ca alternativă la procedeul de laborator se poate imagina un proces de fabricare în care toate elementele (precum şi prealiajul FeP), mai puţin carbonul, sunt topite în cuptorul cu arc folosind tehnica electrodului consumabil. În acest fel carbonul din electrodul de grafit se va alia în topitură treptat, împiedicând formarea carburilor intermetalice.

Table of Content

Motivation

Fe-based bulk metallic glasses (BMGs) have a **high application potential** because of their **unique soft magnetic properties**, combined with **extremely high strength and high hardness** and **significant corrosion resistance**. Also, they can be obtained directly in the **final shape** suitable for use as magnetic sensors, magnetic valves and actuators, magnetic clutches etc. in different devices. Fe-based alloys able to form magnetic BMGs are of the type transition metal – metalloid and often contain 5 or more elements. Usually, the metalloid content is around 22-25 atomic %. A big problem, observed in fact for all BMGs, is related to the **manufacturing conditions** and the degree of **purity of the used elements**. This resides from the amorphous nature of the BMGs, which is a **metastable state** and the presence of certain elements, even in very small quantities, can regress the amorphization. The amorphous state is basically a kinetic freezing of the liquid structure, in other words the liquid alloy solidifies without passing through the crystallization. Usually, there are two ways in which the impurity elements affect the glass-forming ability (GFA): they may act as **seeds for heterogeneous nucleation** or they can **lower the energy barrier** between amorphous and crystalline structure. Both mechanisms are complex and cannot be generalized from one class of alloys to other class of alloys, i.e. what affects a Zr-based alloy may not distress an Fe-based alloy etc.

Despite of numerous reports available in scientific literature, the influence of impurities on the glass formation, from practical point of view as casting repeatability and/or microscopic properties, was **neither studied, nor precisely understood**. There are only few reports, which deal mainly with the oxygen influence (because the oxides are the main products that promote the heterogeneous nucleation), but also these are not systematic studies. The second problem is that generally a scientific report presents the results obtained upon investigation of the best sample(s) from a given composition (or compositional class), obtained in **laboratory conditions**, and in many cases this does not reflect the reality, i.e. the reproducibility of the BMG preparation in industrial conditions is very poor.

The actual thesis is a part of an extended research project and long-standing collaboration between the author- and therefore the Leibniz Institute for Solid State and Materials Research (IFW) Dresden- and the OCAS N.V. Zelzate, Belgium. OCAS (Onderzoeks Centrum voor de Aanwending van Staal, ArcelorMittal Global R&D Gent) is an advanced, market-oriented research center for steel applications. Based in Belgium, it is a joint venture between the Flemish Region and ArcelorMittal, the world's largest steel group.

Chapter 1
Theoretical consideration about metallic glasses

1.1 Metallic glasses

In common practice, the term “Glass” refers to an amorphous (non-crystalline) oxide, made up mostly of silica (SiO_2) and oxides of metals like Al, Ca, Mg, K, Na etc. In general “Glasses” are characterized as “hard, brittle and transparent” substances, used for windows materials and household glassware. It is prepared by the rapid cooling of the molten mixture of silicates and metallic oxides in order to prevent crystallization. During this progressive transition from liquid to solid, which takes place at fast cooling rate, the atoms in the liquid do not rearrange themselves into regular periodic three dimensional structure i.e., crystalline solid. Thus it is possible to say that the atomic arrangement in the glass is similar to that of the liquid with the same composition and hence sometimes referred to as “Super-cooled Liquid” [Ana87]. By analogy, the term “Metallic Glass” refers to an amorphous metallic alloy prepared by the rapid solidification of molten metallic alloy, hence it lacks the long range order symmetry and results in an amorphous liquid-like structure or sometimes called “Super-cooled Metallic Liquid” at room temperature.

Since the discovery of the first “Metallic Glass” of composition $Au_{75}Si_{25}$ in 1960 by Pol Duwez et al. [Kle60] at the California Institute of Technology, Pasadena, USA, it has become a very interesting topic for metallurgists and material scientists to study the rapidly solidified alloys in different parts of the world. They used splat-quenching or gun technique to produce amorphous alloys in form of thin foils. In this process, a small liquid globule was propelled into small droplets by means of a shock wave and the droplets were sprayed on a cold copper substrate. Though it was an unexpected and surprising development, the properties of metallic glasses were found to be better than the crystalline alloys of identical compositions. The cooling rate required to produce these glasses were of the order of 10^6 K/s, thereby restricting the specimen geometry to thin ribbons, foils and powders [Ana87]. The required cooling rate for producing metallic glass was too high in order to suppress normal solidification, because the latent heat of solidification for metals i.e. thermal energy released during the phase transformation from the liquid to the solid phase is very high.

The earliest technique applied for the fabrication of metallic glasses in shape of wires or tapes for the technical application was reported by Chen and Miller in 1970 [Che70]. In this technique a molten alloy is put into the gap between a pair of rapidly rotating rollers which creates very high cooling rates. But the most commonly used process for the fabrication of amorphous alloy in form of ribbon is the well-known technique patented by Strange and Pim in 1908 [Str08], in which the molten stream is cast on the outer surface of very high speed rotating copper wheel. The quenching rates achieved by these techniques are of the order of 10^6 K/s and hence widely used as industrial manufacturing process as well as for research laboratory and allows to continuously produce glassy ribbons of 20-100 μm thickness and with a width in the centimeter range.

Generally, Fe-based and Co-based glassy alloys are well known for their good magnetic properties like soft ferromagnetic or hard ferromagnetic depending on compositions, constituents and subsequent heat treatment of alloy. The Fe- and Co-based bulk metallic glasses (BMGs) have soft magnetic properties because of absence of any crystalline anisotropy. The Fe- and Co- based BMGs- or, better, glassy alloys, may display also hard magnetic properties with high remanence after annealing at appropriate temperature because of the formation of some hard magnetic crystalline phases inside the amorphous matrix and hence has very good exchange interaction between soft magnetic amorphous phases and hard magnetic crystalline phases.
Since the preparation of amorphous alloys in Fe-metalloid systems which exhibit good soft-magnetic properties in ’70ies [Fuj74, Han76], a large number of studies on the development of soft-magnetic amorphous alloys have been carried out for the subsequent decade. However, the shape and dimension of the Fe- and Co-based amorphous magnetic alloys have been limited to thin ribbon form with thicknesses below 30 μm because of the necessity of a high cooling rate of almost 10^6 K/ s for the formation of an amorphous phase [Cah93].

More recently, since 1988, Akihisa Inoue and his group from Institute of Materials Research (IMR) Sendai, Japan, have succeeded in finding new multi-component alloy system with much lower critical cooling rates in the Mg-, Ln-, Zr-, Fe- , (Pd-Cu)-, (Pd-Fe)-, Ti- and Ni-based alloy systems [Ino00]. This fact makes possible the use of other preparation routes- like, for example, the copper mold casting method.

In 1995, a distinct glass transition before crystallization was found in the $Fe_{72}Al_5Ga_2P_{11}C_6B_4$ rapidly solidified alloy [Ino95a], and an $Fe_{73}Al_5Ga_2P_{11}C_5B_4$

ferromagnetic bulk metallic glass (BMG) was synthesized through the stabilization of supercooled liquid [Ino95b]. Subsequently, a variety of Fe-based ferromagnetic BMGs have been developed because of their potential magnetic applications [She99, She02]. Now, the development of Fe- and Co-based BMGs with high glass forming ability (GFA) has become a very hot research topic not only because of the soft-magnetic properties [Paw03, Sto05b] but also of the high fracture strength (σ_f) [Ino03, She05].

The IFW Dresden plays a pioneer role in the investigation and development of BMGs since they were discovered [Sto05a]. The author itself focuses his research activities on the study of mechanical and magnetic properties of bulk amorphous alloys, as well as on the structural evolution and the relations between structure and properties. The amorphous samples are prepared through liquid metallurgy (melt-spinning, copper mold casting, injection casting, centrifugal casting system etc.) and powder metallurgy routes. The structure and properties correlation of BMGs are investigated by using various characterization tools like differential scanning calorimetry (DSC), X-ray diffraction (XRD), scanning electronic microscopy (SEM), transmission electronic microscopy (TEM), vibrating sample magnetometer (VSM) etc. As a result of research activity, a large number of scientific papers were published in international peer-reviewed journals [IFW]. Also, new amorphous and nanocomposite non-ferrous alloy with excellent mechanical properties were produced, subjects of several new patents issued in the last decade [IFW].

1.2 Metallic alloys in the glassy state- thermodynamic and kinetic considerations

A glass lacks three-dimensional atomic periodicity beyond a few atomic distances. It is characterized by a limited number of diffuse halos in X-ray, electron and neutron diffraction and no sharp diffraction contrast in high-resolution electron microscopy. Glasses have been found in every category of materials and of various bond type: covalent, ionic, van der Waals, hydrogen and metallic [Tur69]. The glass-forming tendency varies widely. Some oxide mixtures form a glass at normal slow cooling rates of ~1 K/min, while monoatomic metals with possible incorporation of impurities require rates as high as ~10^{10} K/s [Dav73].

During the solidification no essential change in spatial atomic configuration occurs. A glass may be considered as a **solid with frozen-in liquid structure**. It is in

general not in an internal equilibrium state and thus relaxes structurally to a more stable equilibrium state whenever atoms attain an appreciable mobility. Furthermore, a glass is **metastable** with respect to crystalline phase(s) and transform to the latter through nucleation and growth. On heating, a glass would transform to the liquid phase provided that the rates of crystallization are sluggish enough- or the heating rate is high enough, compared with the cooling rate upon which the glass was obtained. The most important fact necessary to be fulfilled during cooling from the liquid state is that **the crystal nucleation and/or growth is avoided**. In this conditions any metallic liquid would become a glass.

The viscosities of most common liquids above their melting point are of the order of 10^{-3} Pa·s [Tur69]. It is evident that, to change from this value to 10^{14} Pa·s, the viscosity must increase very rapidly over some part of the temperature range in the transition from liquid to glass. In fact, the viscosities of glass-forming liquids are fairly well described, at least between 10^{-3} and 10^{6} Pa·s, by the Fulcher [Ful25] equation:

$$\eta = A\exp\left(\frac{a}{T - T_0}\right), \tag{1.1}$$

where A, a and T_0 are constants depending on the material and T is the absolute temperature. When $T_0 = 0$, the equation changes to the Arrhenius form. η will increase very rapidly with falling temperature either when a is very large relative to T or, if a is small, when T has fallen nearly to T_0. The viscosities of pure silica (SiO_2) or of germania (GeO_2) are quite well described [Coh59] by an Arrhenius equation ($T_0 \sim 0$). In contrast, the viscosities of such glass formers as toluene or isobutyl chloride are described by rather small values of a but with T_0 being a substantial fraction (1/2 to 2/3) of the melting temperature T_m. This means that upon cooling the viscosity increases slowly with falling temperature close to T_m, but it increases extremely rapidly when the temperature approaches T_0. The change from the liquid with low viscosity to a rigid glass with very high viscosity takes place within a quite narrow temperature interval above T_0.

Turnbull [Tur69] explained that the crystallization of a fluid occurs by the formation, called “nucleation”, of crystallization centers (nuclei) and the growth of these centers at the expense of the adjacent fluid. In contrast, a glass forms homogeneously by kinetic freezing of atoms throughout the entire liquid. However, the extraction of heat, which usually drives glass formation, is normally through the external surface of

the liquid. The crystallization rate of an undercooled liquid is then specified by the rate of crystal nucleation and by the speed u with which the crystal-liquid interface advances. Both of these rates strongly depend on the reduced temperature T_r and the undercooling ΔT_r, which are defined as [Tur69]:

$$T_r = \frac{T}{T_m}, \qquad \Delta T_r = \frac{T_m - T}{T_m}. \tag{1.2}$$

The velocity of the crystallization front is inversely proportional to an average jump time τ_i of the atoms in the interfacial region and directly proportional to some function $f(\Delta T_r)$ of the undercooling, which drives crystallization. This function must increase with ΔT_r from 0 at $\Delta T_r = 0$ in the following way: at small ΔT_r it is linear in the limit that all crystal surface sites are suitable for the reception of atoms and it rises as a higher power of ΔT_r in the other cases.

Nucleation in an undercooled liquid is almost always heterogeneous on seeds which are either present accidentally or deliberately injected into the system [Tur69]. These seeds may be **crystals of the material itself** or **other solid materials**, such as the container walls or particles suspended in the liquid. At a given cooling rate the undercooling required for heterogeneous nucleation varies widely with composition and structure of the seed material [Tur69].

Nucleation within the liquid and without the help of seeds is called **homogeneous**. Experimentally it is difficult to circumvent the effects of seeds and thereby realize homogeneous nucleation behavior. Liquids commonly contain 10^5 to 10^6 suspended particles per cm^3 [Tur69]. When the liquid is undercooled, nucleation will occur first on the most effective seed and then, unless the crystal growth rate is very small, recalescence will cut off the possibility of any further independent nucleation either on other seeds or homogeneously [Tur69], because during the recalescence the temperature may increases as an effect of latent heat release. **The heterogeneous nucleation cannot be controlled, but it can be avoided during preparation of amorphous samples**.

Upon phase transitions, such as solidification, the transformation process cannot occur at any arbitrarily small undercooling. The reason arises from the small curvature of the interface associated with a crystal of atomic dimension. This curvature lowers the equilibrium temperature so that, the smaller the crystal, the lower is its

melting point. The critical size, r_0, of a crystal can be easily calculated [Tur69], as it will be shown later.

The first attempts to describe nucleation processes were done by Volmer and Weber [Vol26] who treated the condensation of a supersaturated vapor. This model has been later extended by Becker and Döring [Bec35]. Fisher and Turnbull applied the basic concepts of this theory to the liquid-solid phase transition [Tur49, Tur61].

In liquid metals, random fluctuations may create minute crystalline regions (clusters, embryos) even at temperatures above the melting point, but these will not be stable. They continue to be metastable also below the melting point because of the relatively large excess energy required for surface formation, which tends to weight the energy balance against their survival when they are small. The interface term, G_i, and the volume term, G_v, of the Gibbs free energy, at a temperature below the melting point T_m, are shown in Fig. 1.1. The critical condition for the nucleation of 1 mole is derived summing the interface G_i and the volume G_v terms of the Gibbs free energy [Kur89]:

$$\Delta G = \Delta G_i + \Delta G_v = \sigma \cdot A + \Delta g \cdot v \,, \tag{1.3}$$

where σ is the solid/liquid interfacial energy, A is the area of the solid/liquid interface, Δg is the Gibbs free energy difference between the liquid and the solid per unit volume and v is the volume of the formed solid nucleus. For a nucleus with a spherical shape of radius r, ΔG becomes:

$$\Delta G = \sigma \cdot 4 \cdot \pi \cdot r^2 + \frac{\Delta g \cdot 4 \cdot \pi \cdot r^3}{3} \,. \tag{1.4}$$

The Gibbs free energy per unit volume Δg can be considered to be proportional to ΔT [Kur89]:

$$\Delta g = -\Delta s_f \cdot \Delta T \,, \tag{1.5}$$

where Δs_f is the difference in the slopes of the $G(T)$ functions of the liquid and the solid phase at the melting point of the system.

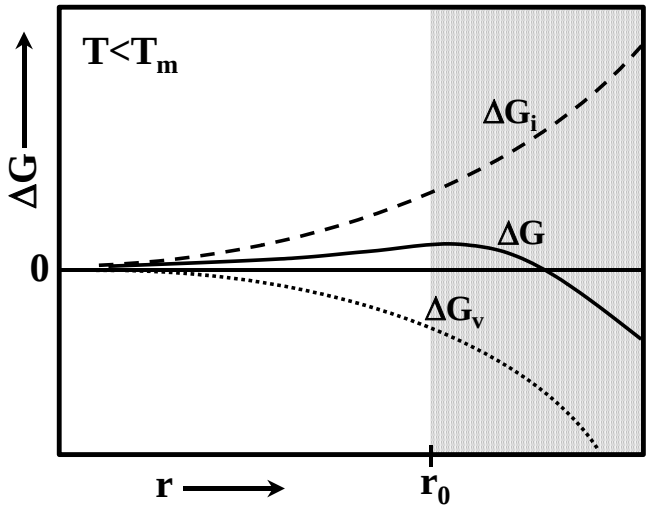

Fig. 1.1 Free energy of a crystal cluster as a function of its radius.

The value of σ is always positive whereas Δg depends on ΔT and is negative if ΔT is positive (Fig. 1.1). This behavior leads to the occurrence of a maximum for $\Delta G(r)$ when the melt is undercooled. This maximum value, which occurs at the critical radius r_0, can be regarded as the activation energy, which has to be exceeded in order to form a stable crystal nucleus, which will continue to grow spontaneously. The criterion for the maximum is:

$$\frac{d(\Delta G)}{dr} = 0\,. \tag{1.6}$$

This can be regarded as the condition for equilibrium between a liquid and a solid with a curvature such that the driving force for solidification is equal to that for melting. Using equations (1.3) to (1.6), the critical radius r_0 and the activation energy ΔG_0, become:

$$r_0 = -\frac{2\cdot\sigma}{\Delta g} \tag{1.7}$$

$$\Delta G_0 = \left(\frac{16\cdot\pi}{3}\right)\cdot\left(\frac{\sigma^3}{\Delta g^2}\right). \tag{1.8}$$

This model is developed for pure metals without impurity particles. It can also be applied to alloys. In this case, the Gibbs free energy is not only a function of

nucleus size, but also of composition *c*. As a first approximation, the critical size and composition would be found in this case from the conditions $d(\Delta G)/dr = 0$ and $d(\Delta G)/dc = 0$, which define a saddle point.

As was previously mentioned, this model refers only to pure metallic melts without impurities, or when the undercooling is so high that the nucleation is completely avoided. Unfortunately, in most practical cases the crystallization occurs via **heterogeneously nucleation**. Let's consider now the case of heterogeneously nucleation, as described by Fig. 1.2. There a catalytic surface (the heteronucleant) is present in a liquid, a surface which is considered to be flat (because the catalyst is much larger than the new embryo), and a solid crystalline embryo which is forming from liquid. Further, beside σ which is the solid-liquid interfacial energy, other two terms must be considered, σ_{cL} and σ_{cS}, which are the catalyst-liquid interfacial free energy and the catalyst-solid interfacial free energy, respectively. If θ is the angle made by the embryo with the substrate (see Fig. 1.2), one can write:

$$\sigma_{cL} - \sigma_{cS} = \sigma \cos\theta \,. \tag{1.9}$$

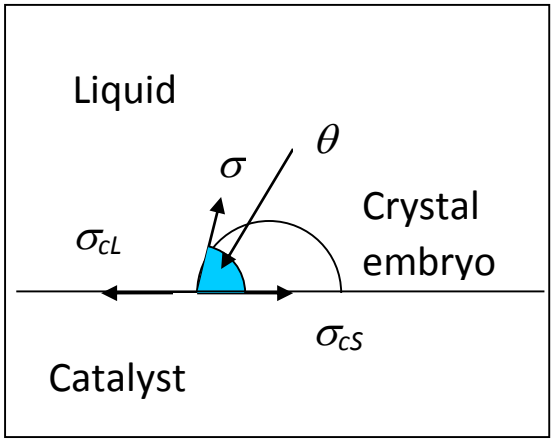

Fig. 1.2 Schematic explanation of heterogeneous nucleation of a crystal embryo in an undercooled liquid.

The critical radius of the spherical cap is given by the eq. (1.7), but the number of atoms in the critical nucleus is smaller than that for homogeneous nucleation as a consequence of the catalytic substrate. The thermodynamic barrier to nucleation ΔG_0 from eq. (1.8) is reduced by a factor $f(\theta)$ to:

$$\Delta G^* = \left(\frac{16\pi}{3}\right) \cdot \left(\frac{\sigma^3}{\Delta g^2}\right) \cdot f(\theta) \tag{1.10}$$

where

$$f(\theta) = \frac{(2+\cos\theta)(1-\cos\theta)^2}{4}. \tag{1.11}$$

If one consider λ the latent heat per unit volume, ΔT is the undercooling (so it is a negative term) and T_m the melting temperature, eq. (1.5) becomes:

$$\Delta g = -\Delta s_f \cdot \Delta T = \frac{\lambda \Delta T}{T_m}. \tag{1.12}$$

Together with equations (1.11) and (1.12) the new energy barrier become:

$$\Delta G^* = \left(\frac{16\pi}{3}\right) \cdot \left(\frac{\sigma^3 \cdot T_m^2}{\lambda^2 \Delta T^2}\right) \cdot \frac{(2+\cos\theta)(1-\cos\theta)^2}{4} \tag{1.13}$$

and the critical radius given by eq. (1.7) changes to:

$$r^* = \frac{2T_m}{\lambda \Delta T} \cdot \frac{\sigma_{cL} - \sigma_{cS}}{\cos\theta} \tag{1.14}$$

It is clear that the nucleation barrier is smaller in the case of heterogeneous nucleation than in the case of homogeneous nucleation. This is why the **heterogeneous nucleation** may take place **before** the **homogeneous nucleation** starts. If nucleation occurs in a scratch or a cavity of the catalytic substrate, the number of atoms in a critical nucleus and the value of ΔG^* can be reduced even more. For a planar catalytic surface, the reduction in the free energy barrier compared to that for homogeneous nucleation depends on the contact angle. Any value of θ between 0° and 180° corresponds to a stable angle. When θ = 180°, the solid does not interact with the substrate, $f(\theta)$ = 1 and the homogeneous nucleation is obtained. When θ = 0°, the solid "wets" the substrate, $f(\theta)$ = 0 and ΔG^* = 0. As a result, solidification can begin immediately when the liquid cools to the freezing point. From the classical

heterogeneous nucleation point of view, a good nucleant corresponds to a small contact angle between the nucleating particle and the growing solid. According to eq. (1.9) this implies that σ_{cS} must be much lower than σ_{cL}. However, in general, the values of both σ_{cS} and σ_{cL} are not known and, therefore it is rather difficult to predict the potential catalytic effectiveness of a nucleant. **In fact, there is no clear insight into what determines θ and how it varies with (i) lattice mismatch between substrate and the stable phase, (ii) topography of the catalytic substrate surface, (iii) chemical nature of the catalytic surface and (iv) absorbed films on the catalytic substrate surface.**

In order to obtain a glass the crystallization must be avoided. Consider now what conditions must be fulfilled by the crystal nucleation frequency and the cooling rate of the liquid if crystallization should be bypassed. The actual number δn of crystal nuclei, which appear isothermally in a volume v_1 of the liquid in time δt is [Tur69]:

$$\delta n = I \cdot v_1 \cdot \delta t \,, \tag{1.15}$$

where I is the nucleation frequency / (volume × time). In a liquid with a low viscosity the crystal growth rate is so large that the cooling rate will be limited by the recalescence after a single nucleus has appeared. Under these conditions nucleation would have to be suppressed completely for crystallization to be bypassed. This means that n would have to be less than 1 [Tur69], where

$$n = v_1 \int_0^t I dt \,. \tag{1.16}$$

t is the time in which the liquid is cooled, I is a function of temperature, and the variation of v_1 with temperature is neglected. Relations (1.15) and (1.16) indicate that the probability of forming a nucleus will decrease with decreasing volume of the liquid, with decreasing nucleation frequency and with increasing cooling rate.

A kinetic analysis based on simple nucleation theory [Tur69] leads to the following expression for the steady frequency of nucleus formation:

$$I = \frac{k_n}{\eta} \exp\left[- \frac{b\alpha^3 \beta}{T_r (\Delta T_r)^2} \right], \tag{1.17}$$

where k_n is a constant specified by the model, b is a constant determined by the shape of the nucleus, and α and β are dimensionless parameters defined as:

$$\begin{aligned} \alpha &= \frac{\left(N\bar{V}^2\right)^{1/3} \cdot \sigma}{\Delta H_m} \\ \beta &= \frac{\Delta H_m}{R T_m} = \frac{\Delta S_m}{R} \end{aligned}, \tag{1.18}$$

where N is Avogadro's number, R is the gas constant, ΔH_m is the molar heat of fusion, $\Delta S_m = \Delta H_m / T_m$ is the entropy of fusion, ΔC_p is the molar difference in heat capacity between the crystal and the liquid and $\bar{V}$ is the molar volume of the crystal. The principal resistance of a fluid to nucleation is limited to α, which is proportional to the liquid-crystal interfacial energy σ. Physically α is the number of monolayers/area of a crystal, which would be melted at T_m by an enthalpy ΔH equal to σ.

Fig. 1.3 [Tur69] shows the calculated variation of the logarithm of the frequency of homogeneous nucleation of crystals in an undercooled liquid with reduced temperature for various assignments of $\alpha\beta^{1/3}$. For numerical modelling the number b was assigned its value for a sphere ($16\pi/3$), η was set equal to 10^{-3} Pa·s, independent of temperature, and k_n was given the value 10^{23} N·m [Tur69]. It is possible to see that I is negligible at small undercooling. In fact, I must become 10^{-6} $cm^{-3}s^{-1}$ ($1\ m^{-3}s^{-1}$) or larger in order to be observable under common experimental conditions. This means that the part of the $I - \Delta T_r$ relation closest to equilibrium where the simple theory is most valid is practically inaccessible to the experiment. With increasing ΔT_r, I increases to a broad maximum at $T_r = 1/3$ and falls to zero at $T = 0$ K. Liquids with $\alpha\beta^{1/3} > 0.9$ would practically not crystallize at any undercooling, unless they are seeded. Thus, they would form glasses for sufficient undercooling. In contrast, it should be practically impossible to suppress, upon cooling to 0 K, the crystallization of fluids with small $\alpha\beta^{1/3}$ (see fig. 1.3).

Experience indicates that β lies between 1 and 10 for most substances and it is near one for most simple monoatomic liquids, such as metals [Tur69]. α has been

measured directly only in a few instances [Buc60, Gli69] and there is no rigorous theory for predicting it. It is reasonable to assume that it may be not greater than 1, i. e. one melted monolayer.

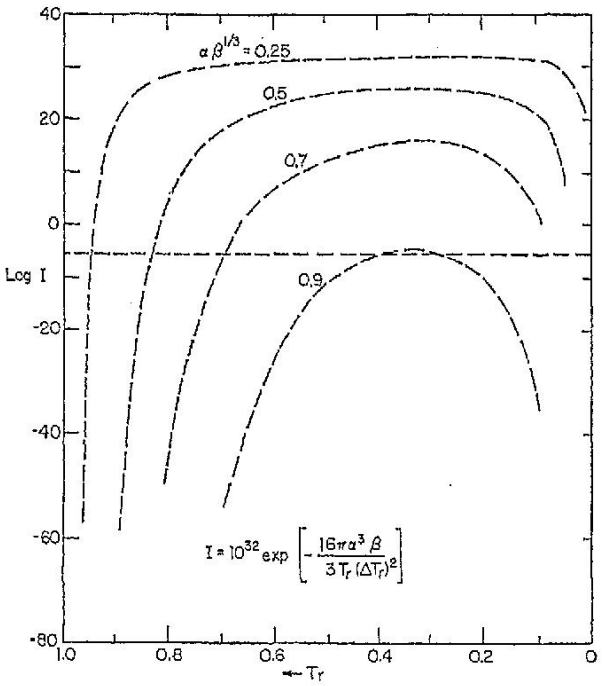

Fig. 1.3 Calculated dependence of the logarithm of the frequency (in $cm^{-3}s^{-1}$) of homogeneous nucleation of crystals in an undercooled liquid as a function of the reduced temperature for various values of $\alpha\beta^{1/3}$ (reproduced from [Tur69]).

Further, Turnbull explained that the glass-forming tendency should increase with the reduced glass temperature $T_{rg} = T_g/T_m$ [Tur69]. The effect of different assignments of T_{rg} on the nucleation frequency, calculated from the simple theory, with $\alpha\beta^{1/3} = 1/2$, is shown in Fig. 1.4. The viscosity was calculated from an equation of the Fulcher form (eq. 1.1) with constants typical for a number of simple molecular liquids. T_g was considered that temperature where η became 10^{14} Pa·s.

From Fig. 1.4 it is possible to see that the effect of increasing T_{rg} is to lower, sharpen and shift the peak in the $I - T_r$ relation to higher T_r values. Liquids with a glass temperature as high as $(2/3)T_m$, if seed-free, would practically crystallize only within a narrow temperature range and then only slowly. Thus, they could be easily undercooled to the glassy state. Liquids with a glass temperature $T_g = T_m/2$ could be chilled to the glassy state only in relative small volumes and at high cooling rates, according to these relations. For example, at a cooling rate $R_c \sim 10^6$ K/s they would

form glasses provided $v_1 < 10^{-7}$ cm^3, i.e. in droplets with a diameter smaller than 60 µm. Of course, the value of T_{rg} required to form a glass at a given cooling rate will be the lower the higher $\alpha\beta^{1/3}$ is.

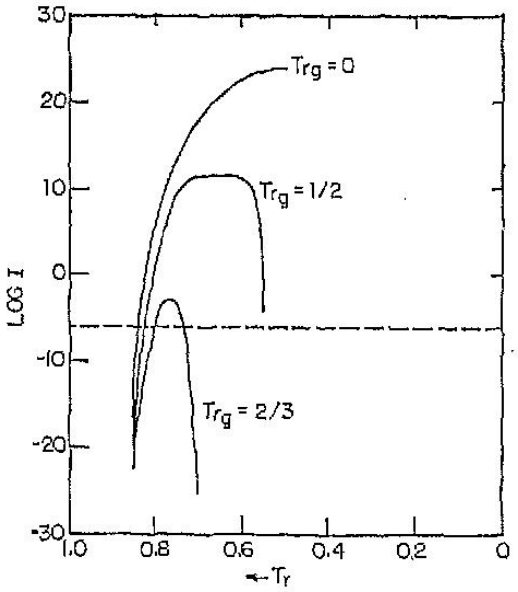

Fig. 1.4 Variation of the logarithm of frequency (in cm^{-3}s^{-1}) of homogeneous nucleation of crystals in liquids with reduced temperature calculated from eqn. (1.17). $\alpha\beta^{1/3}$ was set equal to 1/2 and the viscosity was calculated from the Fulcher equation (reproduced from [Tur69]).

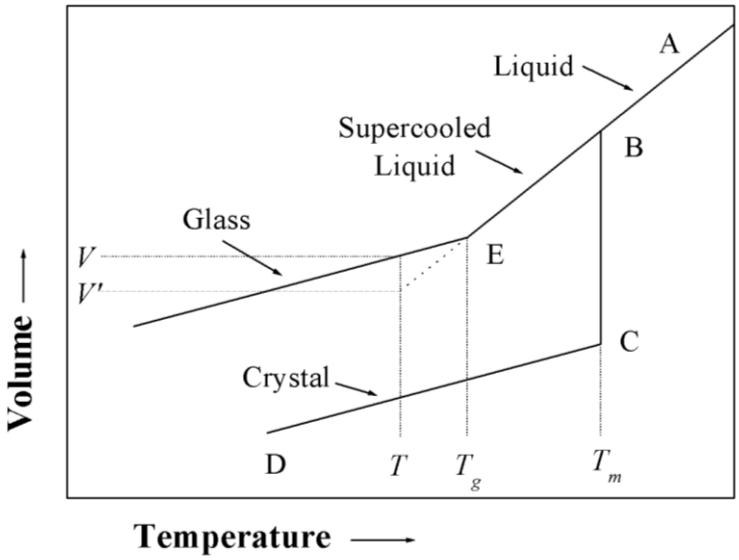

Fig. 1.5 Relationship between glassy, liquid and solid states.

The variation of the volume with temperature for a liquid is shown in Fig. 1.5. On cooling from the initial state A, the volume will decrease steadily along AB. If the rate of cooling is slow and nuclei are present, crystallization will take place at the melting temperature T_m. The volume will decrease sharply from B to C; thereafter, the solid will contract with falling temperature along CD. If the rate of cooling is sufficiently rapid, crystallization does not take place at T_m. The volume of the supercooled liquid decreases along BE, which is a smooth continuation of AB. At a certain temperature T_g the volume-temperature graph undergoes a significant change in slope and continues almost parallel to the contraction graph CD of the crystalline form. Only below T_g the material is a glass. The location of E, the point corresponding to T_g, varies with the rate of cooling and thus it is appropriate to call it a transformation range rather than a fixed point. At T_g, the viscosity of the material is about 10^{14} Pa·s. If the temperature of the glass is held constant at T a little below T_g, the volume V will continue to decrease slowly. It may reach the equilibrium level V' on the dotted line (see fig. 1.5), which is a smooth continuation of the contraction graph BE of the supercooled liquid.

Other properties of the glass also change with time in the vicinity of T_g [Pau90]. This process by which the glass reaches a more stable condition is known as relaxation [Pau90]. Above T_g no such time-dependence of properties is observed. As a result of the existence of relaxation effects, the properties of a glass depend to a certain extent on the rate at which it has been cooled and on heat treatments, particularly in the transformation range.

1.3 Relaxation and crystallization of metallic glasses

Regardless of the processing route used for their production, metallic glasses are not in a state of internal equilibrium and, when heated to a sufficiently high temperature, they tend to a more stable condition. Upon annealing below the glass transition temperature, the glass initially relaxes towards a state corresponding to the ideal frozen liquid with lower energy [Cah93]. The structure evolves to one with higher density, which could be considered characteristic of glass formation at a slower cooling rate [Cah93] and finally, above the glass transition temperature, the glass crystallizes. A metallic glass can be considered as a metastable deeply undercooled liquid and, consequently, has the tendency to crystallize. The driving force for crystallization is the

Gibbs free energy difference between the metastable glass and the more stable crystalline or quasicrystalline phase(s). The dimensions and morphologies of the crystallization products strongly depend on the transformation mechanism, which is closely related to the chemical composition of the amorphous phase and to the thermodynamic properties of the corresponding crystalline phase [Lu96]. According to Köster and Herold [Kös80] the crystallization reaction that may occur during devitrification can be classified depending on the composition change involved. In **polymorphous crystallization** the glass transforms to a single phase with different structure but same composition with respect to the amorphous matrix. This reaction can occur only in concentration ranges near those of pure elements or stable compounds and needs only single jumps of atoms across the crystallization front. Crystallization of a single phase accompanied by a composition change is referred as **primary crystallization**. During this reaction, a concentration gradient occurs at the interface between the particle and the matrix until the reaction reaches the metastable equilibrium. Finally, a crystallization in which two phases simultaneously and cooperatively precipitate from the glass is termed **eutectic crystallization**. There is no difference in the overall concentration across the reaction front and diffusion takes place parallel to the reaction front. This reaction has the largest driving force and can occur in the whole concentration range between two stable phases.

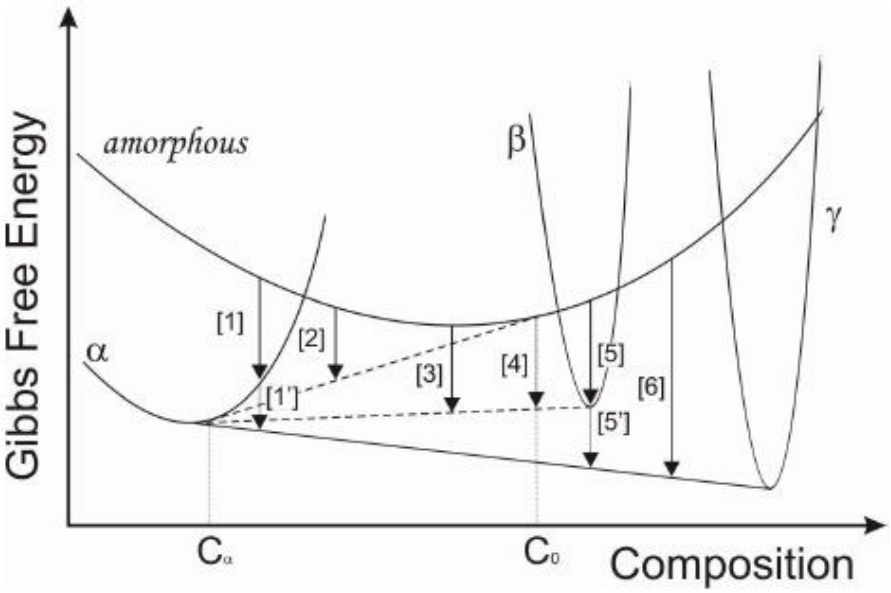

Fig. 1.6 Schematic free energy diagram as a function of composition for the metastable amorphous and β phases, and for the stable crystalline α and γ phases, displaying the possible crystallization reactions (after [Kös80, Sco83]).

The possible crystallization reactions are illustrated by the hypothetical free energy diagram in Fig. 1.6, where the free energy curves for the metastable amorphous and β phases are plotted as a function of the composition, together with those of the stable crystalline phases α and γ. Examples of **polymorphous transformations are reactions 1 and 5** in which the glass crystallizes to the α and β phases, respectively, without change in composition. The devitrification products of the polymorphous reactions **can** subsequently **decompose to the equilibrium mixture of α and γ (reactions 1' and 5')**. Alternatively, the glass can reduce its free energy to a point on the common tangent between α and β or α and γ (reactions 3 and 6, respectively) via an **eutectic mechanism** with the simultaneous precipitation of two crystalline phases. **Reaction 2 illustrates an example of primary transformation**. The glass crystallizes by the precipitation of the phase α with composition C_α, which is different from the composition of the parent glassy phase. As a consequence, solute partitioning takes place and the residual glassy matrix of changed composition (C_0) may subsequently transform by one of the mechanisms described above (e.g., reaction 4).

1.4 Metallic glasses and the glass-forming ability (GFA)

The terms noncrystalline, amorphous, or glassy refer to similar (random) atomic arrangements in solid materials, and therefore these terms have been used interchangeably (quite understandably so) in the literature leading to some confusion [Sur11]. Further, some researchers have been preferably using the term "amorphous," while others have been using "glassy," and a few others "noncrystalline." Added to this, some researchers refer to the thin ribbon glassy materials as amorphous and the bulk glassy alloys only as glasses. Like this, several terms have been used to describe these noncrystalline materials. To avoid the ambiguity and confusion, in the following we will consider that **a glass is an amorphous solid which exhibit a glass transition**. Note that this definition intentionally does not include any reference to the processing route, reflecting the fact that several different techniques may be successfully used for the production of glasses. However, it mentions the most important properties that characterize any glass: the **amorphous** structure, characterized by a lack of periodicity in the atomic arrangement typical of crystals, and the **glass transition**, that reversible phenomenon during which the behavior of the system changes from liquid-like to solid-like or vice versa. From the above definition

follows that **a glass has always an amorphous structure** but **an amorphous material not always displays a glass transition** and thus it is not necessarily a glass. The main parameters which define the GFA are (according to [Tur69, Ino00]):

- The extension of the supercooled liquid region (SLR) ΔT_x, defined as the difference between glass transition temperature T_g and the crystallization temperature T_x. For a good GFA, it should be as large as possible. The reported values may take even more than 100 K for some Zr-, (Zr-Cu)- or Pd-based alloy systems [Ino00], for Fe- or (Fe,Co)-based BMGs being no larger than 40K. However, it is worth to mention that very recently Co-based BMGs with ΔT_x as large as 74 K were synthesized [Tag13]. The **new BMGs** were **prepared at IFW Dresden under the supervision of the author**, using powder metallurgy methods, i.e. hot compaction of milled metallic glass ribbon flakes.
- The reduced glass transition temperature T_{rg}, defined as the ratio between T_g and the melting temperature T_m ($T_{rg} = T_g / T_m$). The melting temperature is usually measured as the onset of melting upon heating, which in general instance is liquidus temperature T_{liq}. A good GFA is characterized by a high T_{rg}, which should approach a theoretical value of 0.66 [Tur69]. The Fe-based BMGs usually do not overcome 0.55.
- The enthalpy of crystallization ΔH_x, which should be high. In fact, ΔH_x is not strictly related to the GFA, but it is rather linked with the degree of amorphicity of a sample. A higher value will always indicate a “more amorphous” sample.

Beside those parameters, the stability of a glass against crystallization can be characterized by calculating the activation energy for crystallization E_a using the Kissinger approach [Kis57] or by using the Johnson-Mehl-Avrami (JMA) plots [Avr39], techniques which will be described later.

In the last decade several other parameters, more or less legitimate, were proposed in order to characterize or predict the GFA. However, is worth to mention here at least the γ-parameter proposed by Lu *et al*. [Lu02, Lu03a], defined as $T_x / (T_g+T_{liq})$. Usually, the γ values of BMGs range between 0.35 and 0.50 [Lu02]. Also, they linked the new dimensionless γ parameter to the critical cooling rate R_c as well as to a maximum achievable thickness t_{max} by studying the data available in literature for representative **non-ferrous** BMGs. The proposed relationships are:

$$R_c = 5.1 \cdot 10^{21} \exp(-117.19 \cdot \gamma) \tag{1.19}$$

and

$$t_{max} = 2.80 \cdot 10^{-7} \exp(41.70 \cdot \gamma), \tag{1.20}$$

respectively, where R_c is in K/s and t_{max} in mm.

All GFA parameters have a common weak point: one needs **first to prepare** the glassy sample(s) **and after to investigate** them in order to extract the characteristic temperatures. Therefore, it is almost impossible to predict the GFA of a new alloy. In practice, the GFA is described as the maximum achievable geometrical dimensions upon direct casting. Furthermore, one speaks about the **maximum achievable diameter** of a cylindrical-shaped sample upon copper mold casting, regardless the method (injection, centrifugal, suction etc.).

1.5 Known BMGs in general, Fe-based BMGs in particular

BMGs are those noncrystalline solids obtained by continuous cooling from the liquid state, which have a section thickness of at least a few millimeters. More commonly, metallic glasses with at least a diameter or section thickness of 1 mm are considered “bulk.” Nowadays researchers tend to consider 10 mm as the minimum diameter or section thickness at which a glass is designated bulk [Sur11], dimension which in the opinion of the author is exaggerated (the majority of BMGs can be produced in mm-range and only few particular compositions allow their production in cm-range).

Along the last almost 20 years, several Fe-based BMGs were developed. Usually, the GFA of these glasses is very limited, much lower when compared to the non-ferrous BMGs. Typical alloy systems, which may form bulk metallic glasses (BMGs), reported up to date, are summarized in Table 1.1, together with the year when the first corresponding paper and/or patent was published. It is apparent that the first bulk glassy alloys, which were developed, were non-ferrous systems followed by the Fe- and Co-based alloy systems. Furthermore, it can be seen that the Cu-based bulk

glassy alloys defined by Cu contents above 50 atomic % were developed most recently, though other bulk glassy alloys also contain Cu as a main additive.

Table 1.1 Typical bulk glassy alloy systems reported up to date together with the calendar year when the first paper or patent of each alloy system was published.

1. Nonferrous alloy systems		2. Ferrous alloy systems	
Mg-Ln-M (M = Ni,Cu,Zn)	1988	Fe-(Al,Ga)-(P,C,B,Si,Ge)	1995
Ln-Al-TM (TM = the VI – VIII group transition metal)	1989	Fe-(Nb,Mo)-(Al,Ga)-(P,B,Si)	1995
		Co-(Al,Ga)-(P,B,Si)	1996
Ln-Ga-TM	1989	Fe-(Zr,Hf,Nb)-B	1996
Zr-Al-TM	1990	Co-(Zr,Hf,Nb)-B	1996
Zr-Ti-TM-Be	1993	Ni-(Zr,Hf,Nb)-B	1996
Zr-(Ti,Nb,Pd)-Al-TM	1995	Fe-Co-Ln-B	1998
Pd-Cu-Ni-P	1996	Fe-(Nb,Cr,Mo)-(C,B)	1999
Pd-Ni-Fe-P	1996	Fe-(Cr,Mo,Ga)-(P,C,B)	1999
Pd-Cu-B-Si	1997	Co-Ta-B	1999
Ti-Ni-Cu-Sn	1998	Fe-Ga-(P,B)	2000
Cu-(Zr,Hf)-Ti	2001	Ni-Zr-Ti-Sn-Si	2001
Cu-(Zr,Hf)-Ti-(Y,Be)	2001	Fe-Cr-Mo-(Y,Ln)-C-B	2004
Cu-Zr	2004	Fe-Cr-Co-Mo-Mn-C-B-Y	2004

Another interesting aspect resides in the fact that the last decade was dedicated more to the understanding of the properties and to the structural refinement rather than to “discover” new compositions which may be amorphised. This is reasonable if one takes in account the development of new methods and techniques for structural investigation, as, for example, the use of *in-situ* and *in-operando* X-ray diffraction in transmission configuration [Sto09, Sto10a, Sto10b]. However, related to magnetic BMGs, the author cast in 2006 an $Fe_{66}Nb_4B_{30}$ BMG with diameter up to 2 mm [Sto06], the first **Fe-based BMG with only 3 elements**, as well as the preparation in 2013 of $Co_{40}Fe_{22}Ta_8B_{30}$ as **BMG pellets with 10 mm** diameter and several mm thicknesses [Tag13], dimensions never attained up to now by a Co-based BMG. The newest alloy developments, not published yet but presented by W.L. Johnson from Caltech

(Pasadena, USA) at International peer-reviewed Conferences (MRS 2013, TMS 2014) seems to be $Ni_{68.6}Cr_{8.7}Nb_3P_{16}B_{3.2}Si_{0.5}$, with a maximum achievable diameter of 20 mm.

Examining the compositions listed in Table 1.1 in detail, it is possible to divide these alloys in five groups, as summarized in Table 1.2. The transition metals belonging to the group numbers I to IV of the periodic table are named ETM (early transition metals), the group VIII transition metals LTM (late transition metals), simple metals are used for Mg and Be, and the metalloids are B, C, Si and P. The first group (i) of bulk glassy alloys consists of ETM (or Ln), Al and LTM, as exemplified for the Zr-Al-Ni and Ln-Al-Ni systems. **The second group (ii) is composed of LTM, ETM and metalloid, as for example Fe-Zr-B and Co-Nb-B systems.** The third group (iii) are LTM (Fe)-(Al,Ga)-metalloid systems and the fourth group (iv) are Mg-Ln-LTM and ETM(Zr,Ti)-simple metal(Be)-LTM alloys. The Pd-Cu-Ni-P and Pd-Ni-P systems (v) are composed only of LTM and metalloid, which are different from the combination of the three types of group elements for the alloys belonging to the four previous groups (i)-(iv). It is important to point out that all the alloys belonging to groups (i) to (iv) are based on the following three empirical rules, summarized by Inoue [Ino00]: **(1) multicomponent systems consisting of more than three elements; (2) significant difference in atomic size ratios above about 12 % among the three main constituent elements;** and **(3) negative heats of mixing of the three main constituent elements.**

Table 1.2 The five groups of composition able to form bulk metallic glasses.

i	(Ln or ETM) – (Al or Ga) – LTM
ii	LTM – ETM – Metalloid
iii	LTM – (Al and/or Ga) – Metalloid
iv	Simple Metal – Ln – LTM or Simple Metal – ETM – LTM
v	LTM – Metalloid

The three empirical rules can be derived from the kinetic and thermodynamic considerations. An alloy, which meets these empirical rules will have a **high degree of dense random packed structure**, from topological and chemical point of view (increased relative density), which leads to **a particular atomic configuration and a multicomponent interaction on a short-range scale**. Upon cooling, the undercooled liquid will have a high solid-liquid interfacial energy, which is favorable for **suppression**

of nucleation of a crystalline phase. The impossibility of atomic rearrangement on a long-range scale for crystallization will **suppress the growth of a crystalline phase.** The difficulty of atomic rearrangement will decrease the atomic diffusivity and increase the viscosity. The multicomponent alloys, which meet the three empirical rules, always have a deep eutectic with a low melting temperature, leading to high T_g/T_m and large ΔT_x values. Therefore, a high thermal stability of the supercooled liquid is observed. Before Inoue [Ino00], in 1993 A.L. Greer [Gre93] explained this behavior in a simpler and concise way: **the alloy has a low chance to select a crystalline structure when a wide variety of elements is present in its composition, it is *"too confused to crystallize"***.

The Pd-Cu-Ni-P and Pd-Ni-P amorphous alloys do not satisfy the three empirical rules (the heats of mixing are nearly zero for Pd-Cu and Pd-Ni [Boe89, Tak05] and the atomic size ratio between Pd and Cu or Ni is less than 10 % [ASM92]). The origin of high stability of the supercooled liquid against crystallization for $Pd_{40}Cu_{30}Ni_{10}P_{20}$ and $Pd_{40}Ni_{40}P_{20}$ bulk amorphous alloys was explained [Ino00] by assuming that the Pd-Cu-Ni-P amorphous alloy is composed of two large clustered units, one corresponding to the Pd-Ni-P region and the other to the Pd-Cu-P region. The coexistence of the two large clustered units seems to play an important role in the stabilization of the supercooled liquid for the Pd-based alloys, because of the strong bonding nature of metal-metalloid atomic pairs in the clustered units, the high stability of metal-metalloid clustered units and the difficulty of rearrangement among the clustered units [Ino00].

The compositions summarized in Table 1.1 exhibit a rather high reduced glass transition temperature and a large extension of the supercooled liquid region. They also need only a relatively low cooling rate for glass formation. Figure 1.7 shows the relationship between the critical cooling rate R_c (which is defined as the minimum rate at which an alloy must be cooled from its liquid state in order to retain the amorphous structure), maximum sample thickness t_{max} and reduced glass transition temperature $T_{rg} = T_g/T_m$ for amorphous alloys reported up to date [Ino00].

The lowest R_c is as low as 0.1 K/s for $Pd_{40}Cu_{30}Ni_{10}P_{20}$ and t_{max} reaches values as large as about 100 mm [Ino97]. It is also noticed that the recent improvement of the GFA reaches 6-7 orders for the critical cooling rate and 3-4 orders for the maximum thickness. There is a clear tendency for the GFA to increase with increasing T_g/T_m. Figure 1.8 shows the relationship between R_c, t_{max} and ΔT_x. One can see a clear

tendency for the GFA to increase with increasing ΔT_x. The values of ΔT_x exceed 100 K for several amorphous alloys in the Zr-Al-Ni-Cu and Pd-Cu-Ni-P systems and the largest ΔT_x reaches 127 K for the Zr-Al-Ni-Cu base system [Zha91].

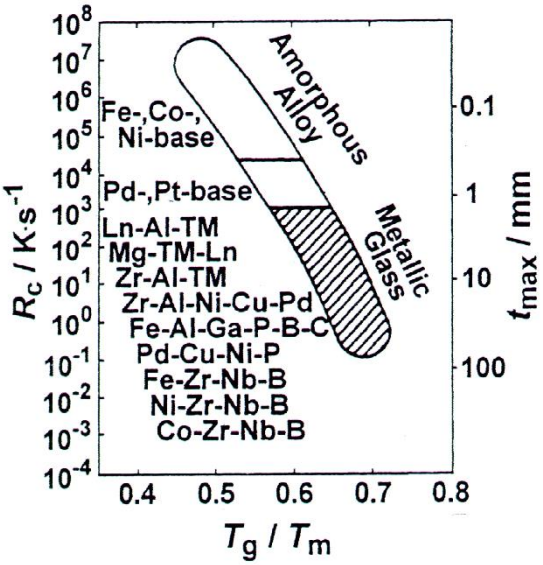

Fig. 1.7 Relationship between the critical cooling rate for glass formation (R_c), the maximum sample thickness of the glass (t_{max}) and the reduced glass transition temperature (T_g/T_m) for amorphous alloys (reproduced from [Ino00]).

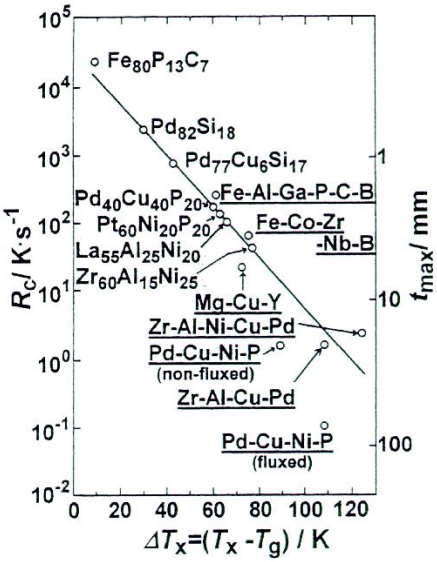

Fig. 1.8 Relationship between the critical cooling rate for glass formation (R_c), the maximum sample thickness of the glass (t_{max}) and the supercooled liquid region (ΔT_x) for amorphous alloys (reproduced from [Ino00]).

As it is shown in Fig. 1.8, the achievable thickness in the case of Fe-based BMGs is limited to few mm. Only in some extremely cases the Fe-based BMGs can reach a diameter up to 12 mm, but those glasses are not magnetic and contain a lot of elements [Pon04, Lu04].

Chapter 2
Methodology and the model alloys

2.1 Structural particularities of Fe-based BMGs

In a BMG the atoms are randomly distributed. Despite that, many BMGs show a kind of a particular short-range order. In most of the cases such order enhances the stability of a glass, as for example the group of Pd-based glasses [Ino00]. The Fe-based BMGs of the type LTM-ETM-Metalloid (as, for example, FeCo-Nb-SiB) behave also in a particular way. Inoue et al. showed that the presence of the ETM (i.e. Nb) up to 4–6 at.% may enhance the GFA by stabilizing the SLR [Ino04]. In fact, starting from $Fe_{80}B_{20}$ and adding Nb, a new behavior was discovered. The stable (equilibrium) crystalline phases which are expected to appear upon devitrification of such glasses are α-Fe and Fe_2B. The presence of Nb changes the succession of crystallization. The first phase which form upon heating from the glassy state is a complex one, of the type $Fe_{23}B_6$. It is a metastable phase which further will transform in the equilibrium products, but at a much higher temperature. This phase is basically fcc-like and has a large lattice parameter of about 1.2 nm, including 96 atoms in its volume unit. Its formation requires a high energy, as well as long diffusion path, and this explain why the amorphous precursors show such good thermal stability and relatively high GFA. Structural, the glass itself develops a kind of short range order, a unique network-like structure in which trigonal prisms consisting of Fe and B atoms are connected with each other in an edge- and plane-shared configuration modes through glue atoms of Nb [Ima01, Ino04]. Furthermore, Poon et al. [Poo03] have pointed out that the large (L) and small (S) atoms may form a strong L–S percolating network or reinforced ‘backbone’ in the amorphous structure, and presumably, this backbone structure can enhance the stability of the undercooled melt, which further suppresses crystallization. In fact, the local triangular unit is quite similar to Fe_3B crystal, as demonstrated by Matsubara et al. [Mat01].

Let’s discuss the above statements in more details. In the Fe_3B crystal, the triangular prisms are connected in two different ways as it is schematically shown in Fig. 2.1. One third of Fe atoms are connected by sharing Fe at the vertex of the prism

and the others by sharing the edge. The Nb elements occupy the vertices in a random manner, and not only Nb can be used but also other large ETM elements like Zr or Cr.

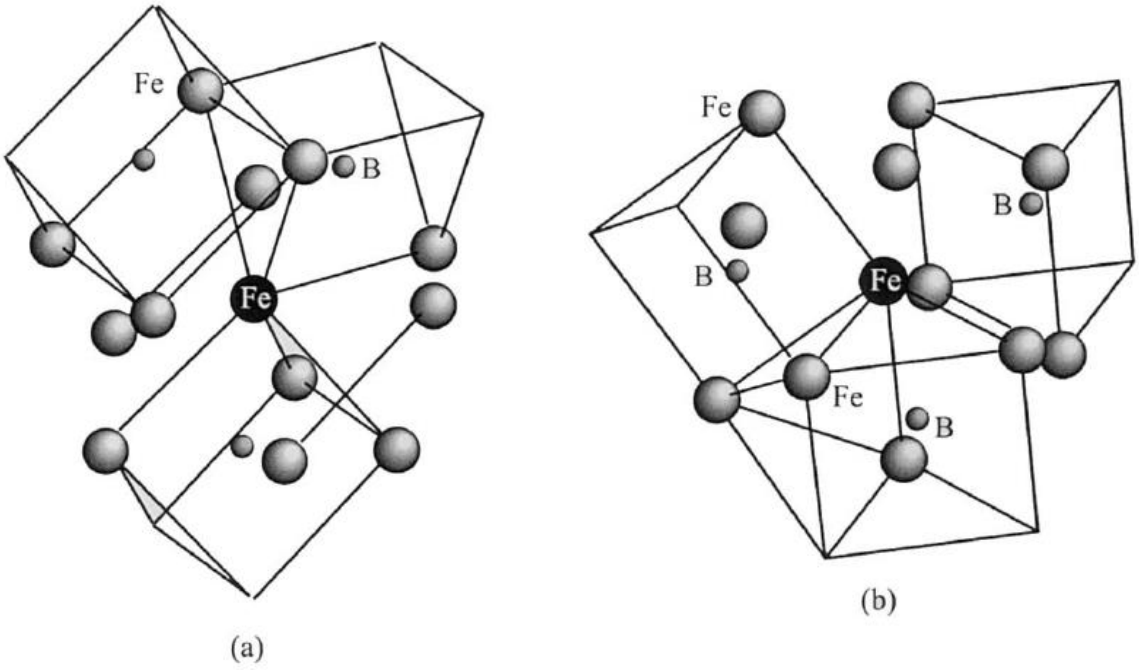

Fig. 2.1 Schematic diagrams of atomic arrangements (a) for the vertex-sharing and (b) edge-sharing triangular prisms in the Fe_3B crystal. Only atoms in the near neighbor region around Fe at the center (solid circle) are drawn (reproduced from [Mat01]).

J. Poon [Poo03] took in account the percentage and the radius of the atoms which are present in the BMG (atom size-composition relationship). The LTM-ETM-Metalloid glasses contains midsize atoms as the majority component (Fe and/or Co, content slightly above 70 at.%), small atoms (the metalloids) as the next-majority component (around 20 at.%), and large-size atoms as the minority component (as for example Nb, content less than 10 at.%), labelled as the “majority atom–small atom–large atom” (MSL) class. In these alloys the heat of mixing is negative. Presumably, the backbone structure can enhance the stability of the undercooled melt, which further suppresses crystallization, in addition to other favorable glass-forming factors that are present in these compositions. However, if the concentration of the L atoms is significantly higher than 10 at.%, there will be an increasing tendency for the L atoms to cluster, which will effectively reduce the interaction between the L atoms and the M and S atoms. Thus, the optimal content of large atoms for forming BMGs of the MSL type appears to be near 10 at.%. The percentage of S atoms is around 20 at.%, while

the L atoms are less than 10 at.%. Thus, the L and S atoms may be seen as forming a strong L–S percolating network or reinforced “backbone” in the amorphous structure, as illustrated in Fig. 2.2.

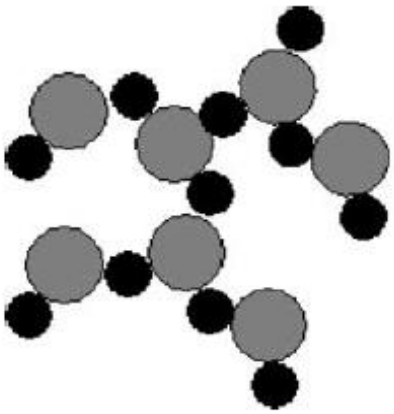

Fig. 2.2 Sketch of atomistic network/ backbone formed by the large atoms and small atoms in the MSL class metallic glasses (reproduced from [Poo03]).

The data published so far prove this theory [Sur11], but the presence of 10 at.% of a large nonmagnetic atoms may deteriorate the ferromagnetic properties. If we consider FeCoBSiNb as a model BMG, our findings, corroborated with other experimental results presented in literature, indicates that a good compromise between GFA and soft magnetic properties is obtained when the Nb content is 4 at.%.

Upon crystallization, such kind of glasses form the metastable $Fe_{23}B_6$ type phase. In this structure, the cubo-octahedra and the cubes formed by metal atoms are connected with metalloid atoms. Thus, the metalloid atoms are surrounded by 8 metal atoms to form an Archimedean square antiprism. These antiprisms ought to be symmetrically arranged in the $Fe_{23}B_6$ structure. In the amorphous Fe-B alloys containing a bit more than 20 at.% B, the local atomic structure is characterized by the non-periodic network of trigonal prisms. The coordination number around the metalloid atoms is expected to be 6 with the first nearest neighbours. Therefore, the change in the chemical short-range order from the trigonal prism to the Archimedean square antiprism as well as simultaneous arrangement of these polyhedra to form $Fe_{23}B_6$ type symmetry should occur for the phase transformation from the amorphous phase to the primary crystalline phase. A drawing of such phase is presented in Fig. 2.3.

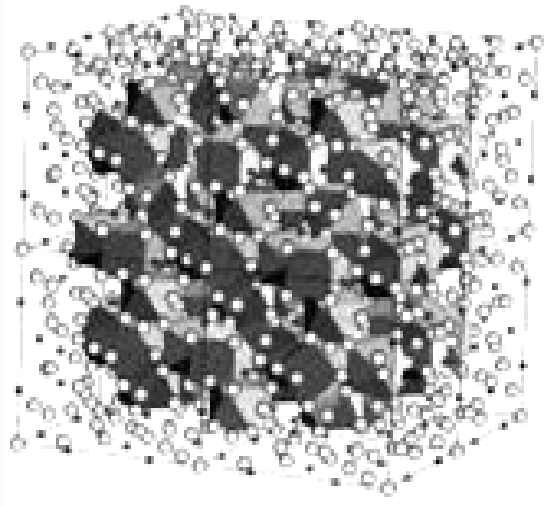

Fig. 2.3 Sketch showing the $Fe_{23}B_6$-type metastable phase (reproduced from [Poo03]).

2.2 Strategy for assessing the glassy nature of the samples

2.2.1 Theoretical aspects

To study the variation of the GFA one has to decide which parameters should be considered. Taking in account the requirements for industrial applications, it is reasonable to consider the **geometry of the samples as a measure of the GFA**. In extenso, if we stick to a specific simple geometry like full cylinders (rods) of a certain length, the maximum achievable diameter for which the products are still amorphous is an indication of the GFA. In other words, the alloy which assures the preparation of a fully amorphous rod in 3 mm diameter (for example) has a better GFA than one which can be amorphised only as rod with 2 mm diameter (assuming that the length is the same). **The amorphous nature of the samples must be investigated by corroborating several measurement techniques**. In the following are briefly described the means used in the present study (the experimental procedures are given *in extenso* in Chapter 3).

X-ray diffraction (XRD). The presence of crystals in the amorphous matrix can be determined by performing X-ray diffraction studies. The well-used Bragg-Brentano configuration may have some limitations: it is difficult to rule-out the presence of a small volume fraction of crystalline inclusions or crystalline nuclei. A better solution is the transmission configuration, but for laboratory devices that use characteristic X-ray tubes there it is a severe restraint regarding the sample thickness (i.e. to approx. 100 μm and below). In this case a better and reliable solution is to use the synchrotron hard X-ray- its brilliance is high enough to pass through a mm-thick sample and its higher energy (i.e. lower wave length) as compared with the X-ray tubes assures a much better resolution when it is about to detect the nano-features embedded in the amorphous matrix. The width and the intensity of the main halo bring as well important details about the amorphicity degree: a more disorganized structure is characterized by a wider diffraction peak with lower intensity.

Differential scanning calorimetry (DSC). The presence of main events that distinguish the glassy structure, as the glass transition and crystallization events, as well as the extension of the SLR, can be easily put in evidence upon DSC measurements. Additionally, the crystallization enthalpy ΔH_x is a good measure of the amorphicity degree (higher the enthalpy, lower the crystalline fraction) and it scales linearly with the crystalline fraction through the following equation:

$$f_X = \frac{\Delta H_{amorph} - \Delta H_{actual}}{\Delta H_{amorph}} \tag{2.1}$$

where f_X is the crystalline fraction, ΔH_{amorph} the crystallization enthalpy of a fully amorphous sample and ΔH_{actual} the crystallization enthalpy of the actual investigated samples.

Time-resolved X-ray diffraction in transmission configuration. This is a very effective method to study the relaxation and crystallization behavior, and therefore to assess the stability of the glassy phase. Such kind of measurements are done in transmission configuration, using the high-energy high intensity monochromatic synchrotron beam.

Magnetic measurements, in particular the coercivity H_c. This method can be successfully applied to magnetic BMGs. Because of the absence of crystalline anisotropy, the ferromagnetic BMGs exhibit good soft magnetic properties, characterized by extremely low coercivity and high permeability. Nevertheless, residual anisotropies may be present, such as shape anisotropy or stress-induced anisotropy, caused by internal mechanical stress induced during the preparation procedure. The unwanted anisotropies can be reduced by annealing the samples at elevated temperatures, but below T_g.

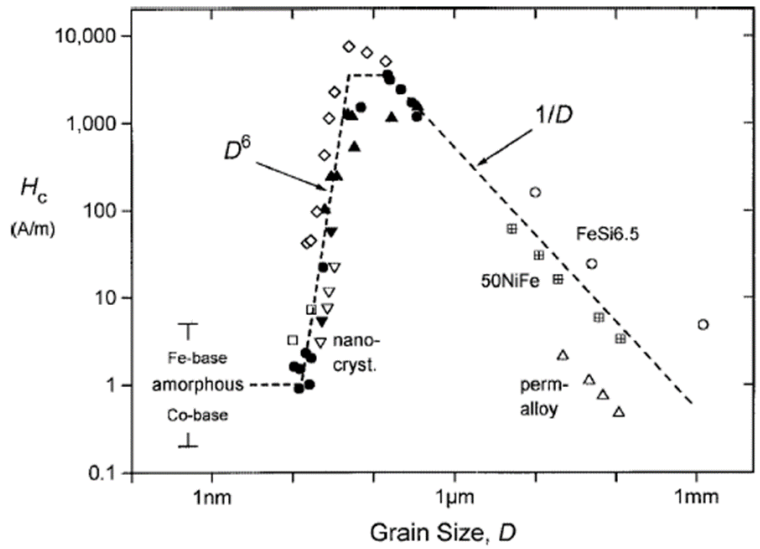

Fig. 2.4 Coercivity H_c vs. grain size D for various soft magnetic metallic alloys: Fe–Nb–Si–B (solid up triangles), Fe–Cu–Nb–Si–B (solid circles), Fe–Cu–V–Si–B (solid and open down triangles), Fe– Zr–B (open squares), Fe–Co–Zr (open diamonds), NiFe alloys (+ center squares and open up triangles) and Fe–6.5Si (open circles) (reproduced from [Her97]).

This method of investigation can prove the presence of some crystals even when they are not detected by the X-ray diffraction studies and therefore can be considered as **the most sensitive one** for our samples. It reliability resides in the fact that for very small crystalline particles, the coercivity scales with the sixth power of their geometrical dimensions. The variation of the coercivity for nanocrystalline magnetic materials was in details summarized by G. Herzer in [Her97], from where Fig. 2.4 is taken. From there it is clear that a fully amorphous sample should have the coercivity below 10 A/m.

Additionally, when there are still doubts regarding the amorphous nature of the samples, **high resolution transmission electron microscopy** (HR-TEM) can be involved. But there are again disadvantages, due to the fact that (a) the probes for TEM are very small and by chance they may not show any crystals if the crystals are not random distributed in the sample, and (b) during the TEM probe preparation process the sample might (nano)crystallize and the TEM image will be affected by artefacts.

2.2.2 Technical aspects

It was mentioned that there does not exist a strict general recipe to find compositions able to form BMGs. Consequently, the minor addition of elements different from the main constituents may affect in a different manner the GFA of different composition, even within the same class of alloys. However, first of all composition with relatively high GFA must be identified. This is why a large amount of work was conducted in this direction and an extensive literature survey was performed.

Generally, **the impurities can be regarded as small addition** even when the concentration is relatively low. As an example, in the case of Finemet® alloy (FeCuNbSiB), there the Cu content is just 1 at.%, but its presence changes completely the behavior of the glass. Now there it is the question if Cu can be regarded anymore as an “impurity” or up to which content one speaks about “impurities”. For example, and as it will be shown later, a similar thing happens with one of our investigated alloys. There the Nb content is maximum 4 at.%, so the presence of other elements even at 1 at.% or less should be treated as an addition. This came because the used raw materials at the laboratory scale usually have a purity superior to 99 %- the BMGs are very sensitive to the cleanliness of the elements. Due to this fact, the first attempts to establish the role of the impurities on the GFA must start directly from the used materials. As will be presented in the next chapters, for each investigated composition

several master alloys were prepared, using only pure elements, using mixture of pure elements and industrial pre-alloys, using only industrial pre-alloys, using pre-alloys made in-house from pure elements etc. The things become more complicated when a new alloy class (or a new composition) is investigated. Usually, there one starts from the premises that the highest GFA is obtained when the purest elements are used. After that, one can substitute some elements partially or totally with “dirty” pre-alloys etc. This gradual way of investigating the alloys has several good parts. All used materials, excepting the pure elements, were chemically analyzed at IFW in order to find-out the actual composition. Studying the changes in the GFA produced by the use of different constituents one can establish the global role of some impurities on the GFA. The other good aspect which results from this method of investigation is the possibility to find which alloy and up to which dimensions can be prepared by using industrial available raw materials.

Other way to investigate the role of the impurities is to take an alloy with known GFA and mix it deliberately with small quantities of different other elements. This is a good method but very laborious, which needs high allocation of man-power and financial resources. A way to simplify the work is to study the crystallization behavior. Once the first crystallized product(s) is/are found, one has to asses which elements may trigger the formation of that specific phase(s). Now, small addition of those elements may be done onto the master alloy. In this way it is possible to find out up to which level several separate additions may affect the GFA.

A third way to investigate the role of the impurities, perfectly suitable for finding especially the effect of Oxygen, is to cast the alloys under controlled atmosphere, at different partial pressure of the air. After, the Oxygen level in each sample should be measured and the results analyzed together with the observed GFA.

2.3 The selection of investigated alloys

The motivation of the entire work stays under the possibility to cast BMGs with soft magnetic properties using industrial raw elements and pre-alloys. Obviously, there are several classes of alloys worth to be investigated. However, in order to study the alloy optimization, focused on finding and understanding the influences of the impurities on the glass forming ability, one should start from a known alloy with **good castability, high GFA and good soft magnetic properties**. We tried to identify some

of such alloys using information available in the scientific literature. What should be mentioned here is that the **achievements mentioned in scientific literature depend on the working environment and technology used**, as well as on the purity or condition of the used raw materials. Also, the available literature data are obtained at a laboratory scale. In many cases, the reproducibility of the results is quite poor and the results presented in a paper do not necessary reflect the behavior of the entire set of samples.

2.3.1 Literature alloy (Fe,Co)-Nb-(B,Si)

Taking in account the available data published so far, the best ferromagnetic alloy system, which is able to retain the amorphous structure when cast as samples with relatively large dimensions, is (Fe,Ni,Co)-Nb-(B,Si). It has the starting point from $Fe_{75}B_{15}Si_{10}$ alloy, which can be cast by melt spinning as ribbons with a maximum achievable thickness of 250 μm [Hag81]. The first attempts to cast a BMG from a similar composition were in 2002 with FeBSiNb [Ino02]. The Nb addition is the reason of a significantly increase of GFA, as it was discussed in the previous paragraph. Due to the fact that Nb content is low and it is present in the master alloy at the expenses of all other elements, in the writing of the compositions the Nb is placed at the end. Table 2.1 show a short summary of these compositions [Ino02]. As it can be seen, the best GFA is attained when Nb content is 4 at.% and the soft magnetic properties, i.e. Curie temperature T_C, magnetic flux density at saturation B_S and coercivity H_c, are very good.

Table 2.1 FeBSiNb compositions investigated by Inoue *et al*. [Ino02].

Alloy	Maximum sample thickness	Thermal stability			Soft magnetic properties		
	t_{max} [mm]	T_g [K]	ΔT_x [K]	T_g / T_l	T_C [K]	B_S [T]	H_c [A/m]
$(Fe_{0.75}B_{0.15}Si_{0.10})_{99}Nb_1$	0.5	815	43	0.56	684	1.50	3.7
$(Fe_{0.75}B_{0.15}Si_{0.10})_{98}Nb_2$	1	812	58	0.57	650	1.49	3.5
$(Fe_{0.75}B_{0.15}Si_{0.10})_{96}Nb_4$	1.5	835	50	0.61	593	1.47	2.9
$(Fe_{0.775}B_{0.125}Si_{0.10})_{98}Nb_2$	0.5	760	N/A	0.54	634	1.51	3.7

Further, the composition was developed and in 2006 was reported first 2 mm diameter rod from $(Fe_{75}B_{20}Si_5)_{96}Nb_4$ [Ino06]. Several investigation conducted over time

and focused on the increase of GFA found out that Fe can be substituted partial or total by Co or Ni (or both of them), but the price was the deterioration of soft magnetic properties, especially decreasing of saturation magnetization. The works concluded that the partial replacement of Fe by Co or Co+Ni causes a significant increase in the glass-forming ability through the decrease in melting and liquidus temperatures, leading to the formation of bulk glassy alloys with diameters up to at least 5 mm for $[(Fe_{0.5}Co_{0.5})_{0.75}B_{0.2}Si_{0.05}]_{96}Nb_4$ [Ino06, She07]. A summary of the thermal stability and, implicitly, the GFA, in the case of Fe-Co-Ni alloys is presented in Table 2.2. The maximum achievable diameter is 5 mm in the case of $[(Fe_{0.5}Co_{0.5})_{0.75}B_{0.2}Si_{0.05}]_{96}Nb_4$.

Table 2.2 Maximum critical diameter, thermal stability and mechanical properties for the Fe-Co-Ni-B-Si-Nb glassy alloys.

Alloy	Maximum sample thickness	Thermal stability		
	t_{max} [mm]	T_g [K]	ΔT_x [K]	T_g / T_l
$[(Fe_{0.9}Co_{0.1})_{0.75}B_{0.2}Si_{0.05}]_{96}Nb_4$	2	832	45	0.570
$[(Fe_{0.8}Co_{0.2})_{0.75}B_{0.2}Si_{0.05}]_{96}Nb_4$	2.5	830	50	0.580
$[(Fe_{0.7}Co_{0.3})_{0.75}B_{0.2}Si_{0.05}]_{96}Nb_4$	3.5	828	50	0.586
$[(Fe_{0.6}Co_{0.4})_{0.75}B_{0.2}Si_{0.05}]_{96}Nb_4$	4	825	50	0.586
$[(Fe_{0.5}Co_{0.5})_{0.75}B_{0.2}Si_{0.05}]_{96}Nb_4$	5	820	50	0.587
$[(Fe_{0.8}Co_{0.1}Ni_{0.1})_{0.75}B_{0.2}Si_{0.05}]_{96}Nb_4$	2.5	818	55	0.606
$[(Fe_{0.6}Co_{0.1}Ni_{0.3})_{0.75}B_{0.2}Si_{0.05}]_{96}Nb_4$	3	792	60	0.608
$[(Fe_{0.6}Co_{0.2}Ni_{0.2})_{0.75}B_{0.2}Si_{0.05}]_{96}Nb_4$	4	800	65	0.611
$[(Fe_{0.6}Co_{0.3}Ni_{0.1})_{0.75}B_{0.2}Si_{0.05}]_{96}Nb_4$	4	813	65	0.613

From the presented data is clear that the best glass former is $[(Fe_{0.5}Co_{0.5})_{0.75}B_{0.2}Si_{0.05}]_{96}Nb_4$. Further, using special techniques including melting together with a fluxing agent (dehydrated B_2O_3 in this case), Inoue's group succeeded to cast this composition up to a diameter of 7.7 mm, concluding that **"*this bulk specimen is the thickest of any soft magnetic glassy alloys formed until now*"** [Bit06]. The used procedure in order to produce this BMG was:

1. Preparation of an eutectic FeNb pre-alloy 75Nb 25Fe (wt.%) by arc melting of pure Nb 99.9% and Fe 99.99%.

2. Arc melting together of Fe 99.9 % and Co 99.9% metals lumps, B 99.5% and Si 99.999% crystals and the Nb–Fe prealloy.

3. The B_2O_3 99.999%, (nominally anhydrous) was preheated at 1273 K (1000 °C) for 130 ks (*sic!*, i.e. ~36 h) sealed in a quartz crucible under vacuum better than 1 Pa (~10^{-2} mbar).

4. Small parts of the previous prepared mast alloy together with the annealed B_2O_3 was sealed in a quartz tube 7.7 mm thick (internal diameter), the volumetric flux-to-alloy ratio being 50-70% vol. The mixture was melted under Ar flow by a torch, held at temperatures well in excess of the liquidus temperature for 100–200 s (~2-3 min), and then cooled to a temperature where B_2O_3 was still molten. This thermal cycle was repeated several times (3-5 times) and at the end the tube was quenched (dropped) in water. The resulted samples are presented in Fig. 2.5 (reproduced from [Bit06]).

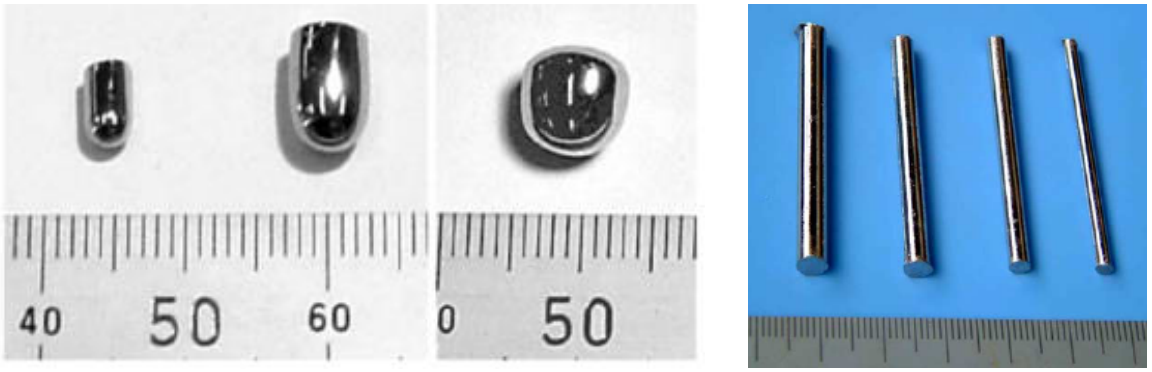

Fig. 2.5 Left: the $[(Fe_{0.5}Co_{0.5})_{0.75}B_{0.2}Si_{0.05}]_{96}Nb_4$ fluxed BMGs. Right: several not-fluxed $[(Fe_{0.5}Co_{0.5})_{0.75}B_{0.2}Si_{0.05}]_{96}Nb_4$ BMGs with diameters up to 5 mm. Pictures reproduced from [Ino06].

In Fig. 2.5 left one can observe that the BMGs have very short lengths, and the geometry of the 7.7 mm diameter rod is close to a sphere, having a length of only 7 mm. However, previous reports coming from the same group have shown BMGs with cylindrical shape having maximum 5 mm diameter and a length of 5 cm (see Fig. 2.5 right).

It must be mentioned here that all results which reports a maximum achievable diameter of 5 mm and a length of 5 cm for $[(Fe_{0.5}Co_{0.5})_{0.75}B_{0.2}Si_{0.05}]_{96}Nb_4$ BMG comes from the same group, i.e. Inoue's group in Sendai, Japan. Other available papers or results presented during some International meetings or Conferences mentioned that for a length of 5 cm only a maximum 2-3 mm diameter can be attained (dimensions for which the samples are still fully amorphous). In our lab the maximum achievable diameter (in the case of this composition, without fluxing the master alloy) is 3 mm for a length of 5 cm. Interesting is that fully amorphous samples with 2 mm diameter and

5 cm in length can be relatively easy to produce, even from master alloys which uses industrial raw elements/pre-alloys. As mentioned earlier, the purity of the starting raw materials, the casting technique used, the casting parameters, as well as the experience of the operator play a very important role in the fabrication of these BMGs. In the current work, the master alloy with the nominal composition $[(Fe_{0.5}Co_{0.5})_{0.75}B_{0.2}Si_{0.05}]_{96}Nb_4$ is the first one chosen for the comprehensive study of what influences its GFA.

2.3.2 Literature alloy Fe-Mo-(P,C,B,Si)

It is known that an industrial pre-alloy or pig iron contains more than only traces of C. This is why, in order to assess the GFA of a BMG made using industrial raw materials, a composition with C is necessary. Combining the achievements presented in literature, together with our own expertise, another possible alloy, also of the type LTM-ETM-Metalloid, was chosen: $Fe_{74}Mo_4P_{10}C_{7.5}B_{2.5}Si_2$. A similar composition was presented by S.J. Pang at the ISMANAM 2007 Conference as being a composition which allows the preparation of BMGs up to 4 mm diameter and a length of 5 cm. We run some preliminary trials on this composition and we found that the GFA is very high, a diameter of 4 mm can be easily reached upon casting, even when dirty raw materials are used. Moreover, a fully amorphous rod with 5 mm diameter and 3 cm length was produced. So, the advantage of such alloy is the good GFA, expected to have a high saturation magnetization due to the high Fe content and also it seems to have rather good mechanical properties (not very brittle, which may enhance the application field). At the first glance, the presence of Mo can be a commercial disadvantage, because of its price, which is twice as high as the Co price, but for example in comparison with the FeCoBSiNb alloy it should be **cheaper**, because the quantity of Mo used is 4 times less than the Co amount. However, if for preparation of $Fe_{74}Mo_4P_{10}C_{7.5}B_{2.5}Si_2$ BMGs only industrial raw materials like FeP, FeB, FeSi, FeMo and graphite might be used (without lowering too much the GFA), it would assure its production at a competitive price.

2.3.3 New alloys and their compositional design strategy

It should be mentioned again that there doesn't exist a **universal recipe** which can be used in order to find new alloys able to retain the amorphous state. However, few things may help to find- or at least to tailor- the composition. For example, one can

suppose that the addition of a big element which can act as “glue” atom (like Nb or Mo) in the complex $Fe_{23}B_6$-type network may be helpful. Also, the addition of Y, for example, may help the glass formation by acting as an oxygen scavenger. Further are summarized the other compositions tried in this work, together with the respective reasons for which the respective compositions were developed, as well as a brief description of the main results, the details being presented later.

- Y-added alloys. It is shown in literature [Lu03b, Pon04] that Y may enhance the GFA by acting- eventually- as an oxygen scavenger, therefore acting toward the intrinsic cleaning the melt and removing the heteronucleants. We added Y to the $[(Fe_{0.5}Co_{0.5})_{0.75}B_{0.2}Si_{0.05}]_{96}Nb_4$ master alloy but the new obtained compositions did not show better GFA. These aspects are presented in subchapter 4.4.

- Following the route used to design the FeCoBSiNb BMGs, we tried to take other known composition which allows fabrication of thick amorphous ribbons and contains C (the reasons of introducing C is already mentioned). This is the $Fe_{77.5}P_{12.5}C_{10}$ alloy, which was reported to be amorphous up to a thickness of 360 µm [Ino82]. The target compositions were $[(Fe_{0.5}Co_{0.5})_{77.5}P_{12.5}C_{10}]_{96}Nb_4$. The high content of P and C makes impossible the simultaneously use of pre-alloys FeC, FeP and FeNb. However, from the homogeneity reasons, at least FeP and FeNb pre-alloys must be used. Preliminary trials with $(Fe_{77.5}P_{12.5}C_{10})_{96}Nb_4$ and $[(Fe_{0.9}Co_{0.1})_{77.5}P_{12.5}C_{10}]_{96}Nb_4$ compositions show relatively good and reproducible results. The advantage of $[(Fe_{0.5}Co_{0.5})_{77.5}P_{12.5}C_{10}]_{96}Nb_4$ composition would be **a new class of magnetic BMGs** (due to the difficulties in preparation, this composition is not mentioned in literature up to now), with **higher saturation magnetization** and **higher permeability**.

Chapter 3
Experimental details and particularities

3.1 Master alloy preparation

In order to prepare the high number of different master alloys used in present study, three different casting techniques and devices were used. Namely, they are induction melting, arc melting and levitation melting (or cold crucible).

3.1.1 Induction melting

The melting in induction was performed using a Balzers induction melting oven. Schematically it is presented in Fig. 3.1. The working crucible is manually sintered around the induction coils and it is made using alumina powders. There are several crucible available, with different dimensions. In such device one can melt from 200 grams to 7 kilograms of Fe-based alloys. The melting chamber can be evacuated down to 10^{-2} mbar and filled with inert gas (i.e. Ar, purity 99.998 %). After melting, the alloy can be left to solidify in the crucible or cast in a mold. The maximum achievable temperature during melting is around 1600 °C and it is carefully monitored from outside with a two-color pyrometer through a glass windows.

Fig. 3.1 Induction melting furnace used in the current work. Left: general view. Right: details where the coil, the melting crucible and the mold can be seen.

3.1.2 Arc melting

In order to melt together alloys which may contain elements with high melting points, or elements with big differences between meting temperatures, one uses the arc-melting technique. The arc-melting device used in the current work is presented in Fig. 3.2. As the induction melting furnace, it is a commercial device. The bottom plate, in which the melting crucibles are formed, is a water-cooled copper hearth and acts as the cathode of the arc-melting furnace. The anode or the melting electrode is a rod manufactured from Thorium-alloyed Tungsten and can withstand temperatures as high as 3000 °C. The furnace can be evacuate down to 10^{-5} mbar and then filled with inert gas.

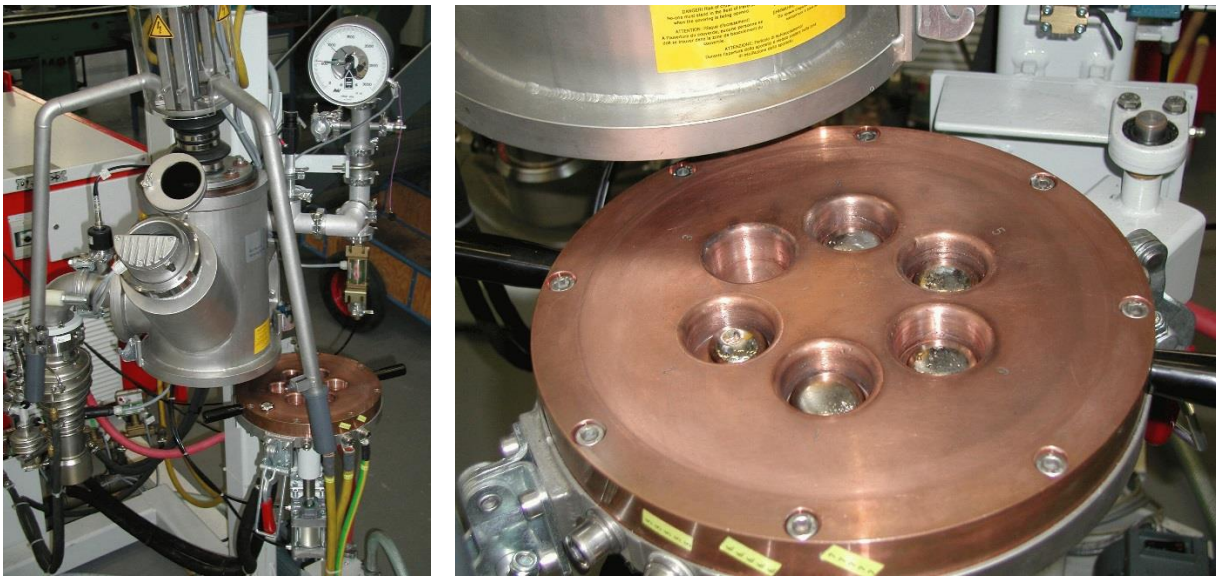

Fig. 3.2 Arc melting furnace used in the current work. Left: general view. Right: details where the bottom plate with some master alloys can be seen.

3.1.3 Levitation melting (cold crucible)

The levitation melting apparatus is an in-house designed device. The principle of levitation melting is schematically illustrated in Fig. 3.3 left side. The cold crucible facility is used in order to produce high purity master alloys. Raw materials and pre-alloys are inductively melted under argon atmosphere on a water cooled copper crucible (cold crucible). Adjusting the coil geometry according to the shape of the copper crucible, charges of about 15 to 25 g can be melted and overheated up to 2000 °C. In order to avoid the eddy currents in the massive crucible wall, it is vertically slit, so that only within the individual segments local eddy currents occur. The melting crucible can be placed in a closed quartz tube (as figured in Fig. 3.3 left) and evacuated to high vacuum and then refilled with inert gas, or the entire system is placed in a

vacuum-tight chamber, as is the actual case presented in Fig. 3.3 right side, which shows the used cold crucible facility. Depending on the cold crucible geometry the molten sample is slightly levitated about 100 μm from the crucible wall. Avoiding any crucible contact, alloys can be produced without contamination. Moreover, at a certain temperature in the overheated state, the molten sample can be sucked into a water cooled copper mold through an orifice at the bottom of the copper crucible. The cylinder-like shaped mold with a diameter of 6 mm and 55 to 100 mm length provides relatively high and uniform cooling rates along the cast rod.

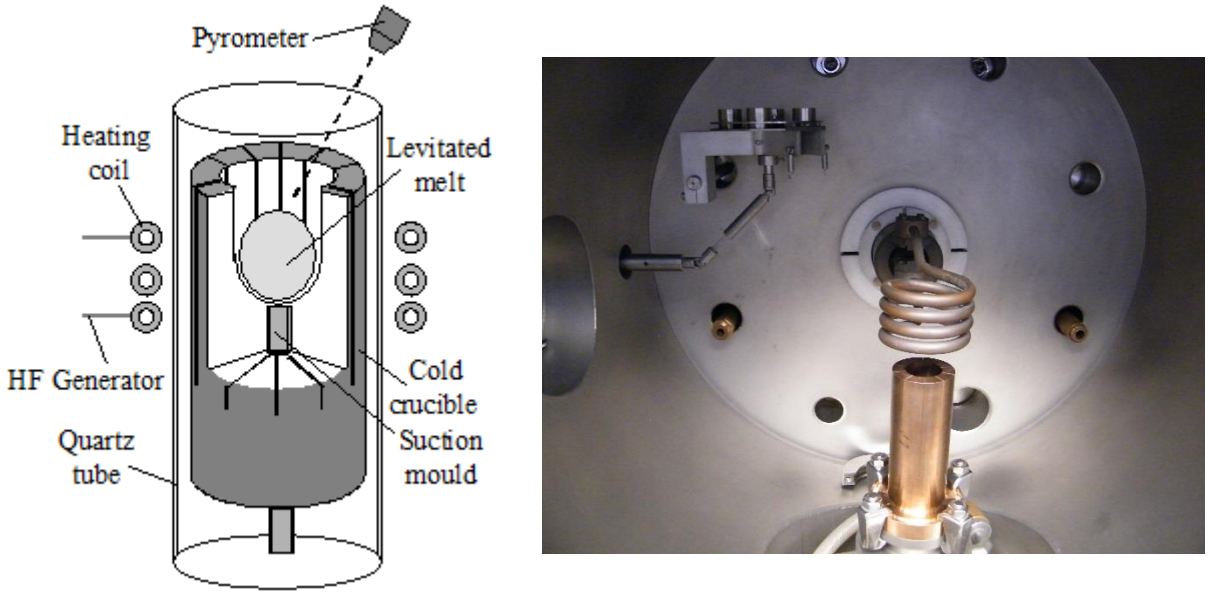

Fig. 3.3 Levitation melting facility Left: working principle schematically explained. Right: details where the coil and the melting crucible can be seen, here in the lower position. During the melting the segmented crucible is pushed up into the induction coil.

3.2 Casting techniques

In order to perform the activities described in this work, a large number of bulk samples with different dimensions and different geometries (i.e. rods and closed rings) were cast. The bulk samples were cast using the method generic-named “copper mold casting”. There two types of copper mold casting devices were used: injection casting and centrifugal casting. The main difference resides in the driving force under which the molten alloy is inserted into the mold: in the first case one speaks about ejection with the help of an inert gas under pressure, while the second technique employs the use of centrifugal force. In the following all these preparation routes are described in details.

3.2.1 Injection casting

The experimental set-up (see Figs. 3.4 (a) and (b)) consists of a closed chamber, which can be evacuated up to 8 x 10^{-5} mbar and filled with inert gas(es). In actual experiments Ar with a purity of 99.998 % was used. There a Cu-mold is placed and above it is a fused silica crucible which contains the working alloy. The melting was done by induction, using a high-frequency generator with a maximum power of 35 kW at a nominal frequency of 60 kHz, and the temperature was monitored from outside by a two-color pyrometer. The crucible can be put in contact via an electromagnetic valve with a tank which contains as well pure Ar (99.998 %) at a pressure superior to that in the working chamber. The pyrometer, crucible, nozzle and the opening of the Cu-mold are very careful aligned. There the molten alloy is ejected with the help of Ar gas over-pressure. The cooling rate attainable during quenching can reach few hundreds of K/s. This results in the formation of a sample, which can be detached easily from the mold due to thermal contraction difference. The round nozzle dimension of the used silica crucible was 0.9 mm. The temperature at which the melt is ejected is usually 150-200 K above the melting point.

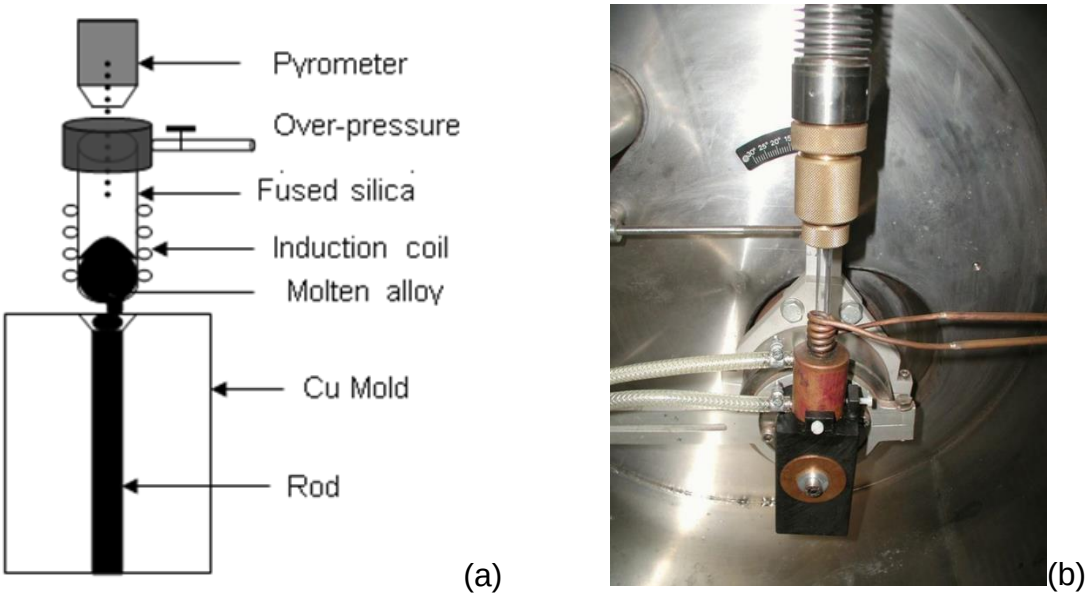

Fig. 3.4 (a) A sketch of the used injection copper mold casting apparatus and (b) the picture of the actual device used at IFW Dresden.

3.2.2 Centrifugal casting

The centrifugal casting method has the advantage of a higher driving force for casting. In this way, alloys with higher viscosities can be cast relatively easy. The device uses the induction melting of the alloy and the mold is placed horizontally (see fig. 3.5). The chamber can be evacuated up to 10^{-4} mbar and filled with pure Ar. The

temperature is monitored from outside by a two-color pyrometer. The ejection is usually performed when the alloy has a temperature of 150-200 K above its melting point. The system can reach 500 RPM in 1 s, assuring an acceleration of at least 13 m/s. The achievable cooling rates are of the order of hundreds K/s. It should be noted that this device was specially used in order to produce the newly ring-shaped BMG.

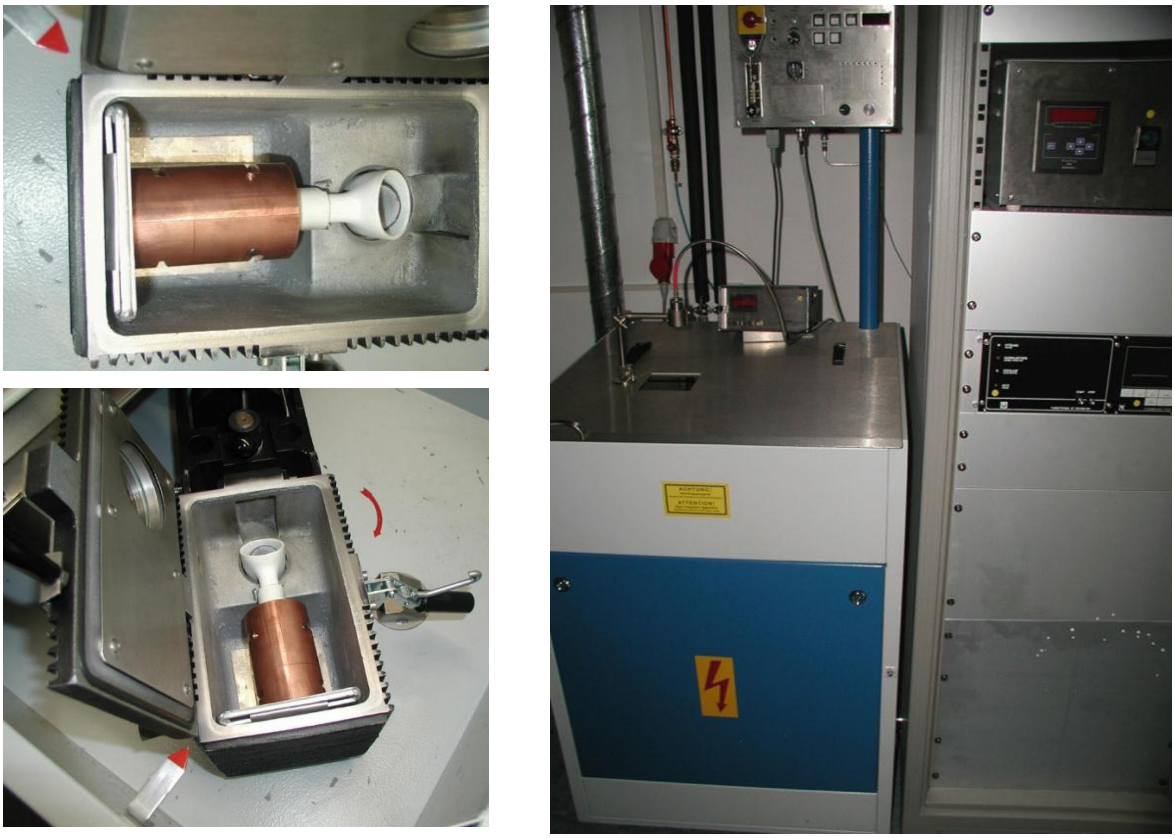

Fig. 3.5 The centrifugal casting device. Here one can remark the melting crucible (transparent quartz, inserted in a white alumina crucible) and the copper mold. The alumina crucible extends below the chamber, through a glass cup, into the induction coil. The coil retracts automatically in the spinning moment.

3.3 Analysis techniques

3.3.1 Chemical analysis

Oxygen, Nitrogen and Sulfur contamination, as well as composition deviations due to the evaporation of some elements during the melting processes were carefully checked in the Chemical Analysis Group of the IFW Dresden.

The oxygen analysis was performed by the carrier gas-hot extraction method, using a LECO USA TC-436 DR analyzer. Samples with a mass of ~50 mg were cut and carefully etched for 5 min in a solution of absolute ethanol with 10 vol.% of

concentrated HNO_3 to remove the oxygen surface contamination, which naturally occurs during cutting. The method consists of melting and heating the samples to temperatures of about 2500 ^oC in a resistively heated furnace using graphite crucibles. At this state, the Oxygen contained in the molten sample is reduced in the neighborhood of the crucible wall by reaction with the Carbon atoms, which diffuse from the graphite crucible into the sample. In this way, CO forms, which is then extracted and carried away from the reaction area by a continuous helium gas flow. The gas mixture is analyzed by infrared radiation absorption to detect and quantify the CO. The absolute error of this method is about ± 0.01 at.%. The Oxygen content was checked for the pre-alloys, as well as for the final master alloys and the cast amorphous samples. In a similar way, Nitrogen and Sulfur contaminations were checked.

The Carbon content of the FeC prealloy (as well as the content in some master alloys or cast samples) was measured by a combustion method using a LECO USA CS 244 analyzer. Two different measurements were used in order to distinguish between the mean Carbon concentration and the amount of unalloyed graphite. The first method consists of melting and heating the alloy to a high temperature (700 to 2700 ^oC) in a continuous flux of oxygen. The Carbon contained in the molten sample is oxidized and CO_2 is formed in the strongly oxidizing atmosphere. The released CO_2 is transported by the Oxygen gas flow to be analyzed and quantified by infrared absorption.

To determine the amount of possibly unalloyed graphite, the samples were subjected to a selective chemical dissolution in an acid mixture of concentrated HNO_3 and HF. The unreacted rests, which are supposed to consist of graphite, were filtered and analyzed by the combustion method described above.

The elemental composition was evaluated in order to find the actual composition of the several pre-alloys and master alloys. The analysis was performed using the spectrophotometry (ICP-OES), with the help of a CARL ZEISS Specord M 500 Spectrophotometer. In this case, small pieces of the alloy samples were dissolved in acid and the solution was mixed with an excess of reagent, which forms a colored reaction product with the initial solution. The light absorption of the colored solution is measured in a cuvette using ultraviolet or visible radiation of a defined wavelength. The absorption is proportional to the concentration of the dissolved element. The detection limits depend on the element, element concentration and used standards. In

our lab these limits usually are 0.01 wt.%, excepting C, O, N and S where the limits can go as low as 1 wt. ppm.

3.3.2 Thermal analysis- heat flux DSC

A computer-controlled differential scanning calorimeter (NETZSCH DSC 404) was used in order to determine glass transition, crystallization and melting points of the investigated alloys. The device measures temperatures and heat flows associated with thermal transitions in a material. The DSC 404, sketched in Fig. 3.6, is a heat flux DSC (in fact it is a DTA- differential thermal analyzer, but the software permits to see directly the heat flow as a function of temperature) and the instrument signal is derived from the temperature difference between sample and reference at the same heat input. The device contains two small crucibles (pans), which sit on a small slab of material with a known (calibrated) heat resistance *K*. The temperature of the calorimeter is raised linearly with time (scanned), i.e. the heating rate $dT/dt = \phi$ is kept constant.

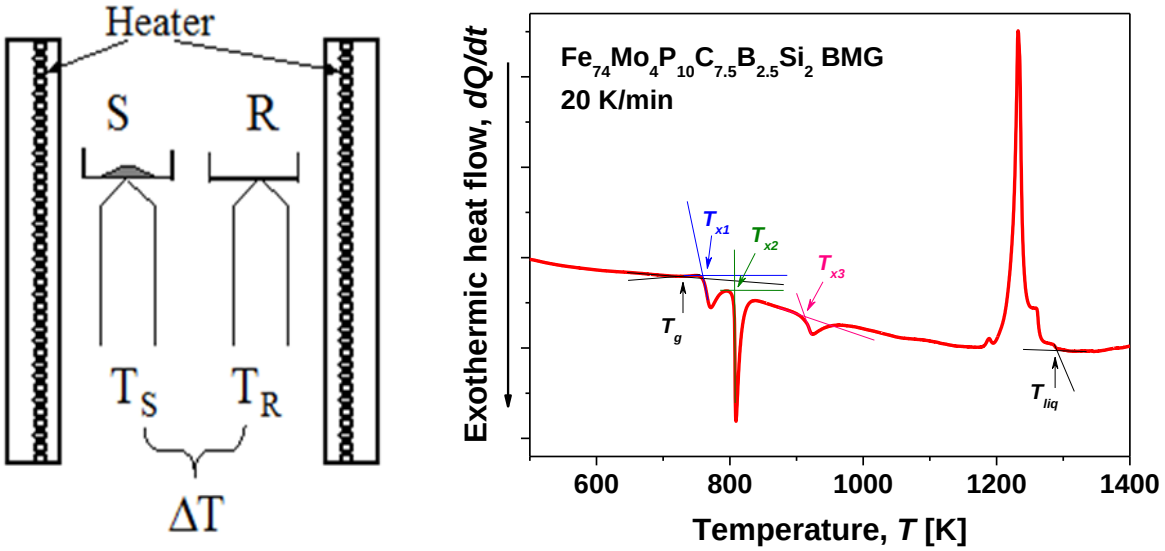

Fig. 3.6 Left side: principle of heat flow DSC: S- sample crucible, R- reference crucible, T_S, T_R- thermocouples. Right side: a typical isochronal DSC plot, measured at 20 K/min for an $Fe_{74}Mo_4P_{10}C_{7.5}B_{2.5}Si_2$ BMG sample. The two-tangent measurement method and the main temperatures are figured as well.

The heat flows into the two pans by conduction. The flow of heat into the sample is larger because of its heat capacity C_p. The difference in flow *dQ/dt* between sample and reference induces a small temperature difference ΔT across the slab. This temperature difference is measured using thermocouples (see Fig. 3.6). The heat capacity can in principle be determined from this signal:

$$\Delta T = K\frac{dQ}{dt} = KC_P\phi \quad , \quad \text{and thus} \quad C_P = \frac{\Delta T}{K\phi}. \tag{3.1}$$

When a sudden change in the heat capacity occurs (e.g. when the sample melts), the signal exhibits a peak. From the integration of this peak the enthalpy of melting can be determined, and from its onset the melting temperature. Samples of about 20 mg mass were investigated up to 1300 °C using heating rates of 40, 20 or 10 K/min. DSC measurements were carried out in 100 ml/min flow of 99.998% pure Ar. The glass transition temperature T_g, the crystallization temperature T_x and the liquidus temperature T_{liq} were determined as the onsets of the respective events, using the two tangents method, as figured in Fig. 3.6. More details can be found, for example, in [Spe94].

3.3.3 Thermal analysis- power compensated DSC

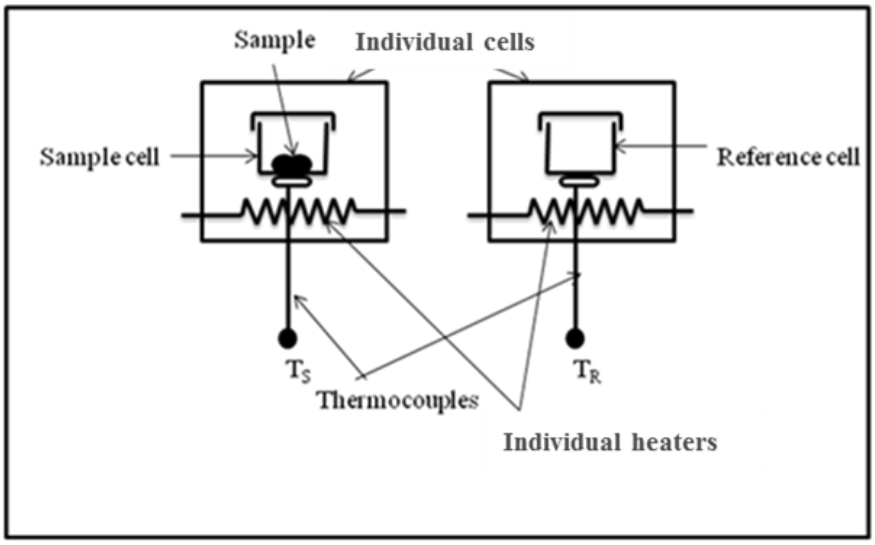

Fig. 3.7 The working principle of power-compensated DSC. S- sample, R- reference, T_S, T_R- thermocouples.

The PERKIN ELMER DSC 7 works in a power compensated mode. The working principle is sketched in Fig. 3.7. There each cell has not only its own thermocouple, but also its own heater. Due to this construction the temperature of each cell (i.e. sample and reference cells) can be *independently* controlled and kept constant, The instrumental signal in this mode is derived from the power supplied to the sample or to the reference material in order to keep the temperature difference between the sample

and the reference (ΔT) equal to zero by the help of a bridge circuit. The power required to keep the bridge circuit in balance is proportional to the change in heat capacity or enthalpy (ΔH) change i. e. $dQ / dt \sim \Delta H$. This DSC was used in order to study the isothermal crystallization. For that, the sample was heated up to a certain temperature above T_g (i.e. in the supercooled liquid region) and maintained there until the complete crystallization. The accuracy of all thermal experiments lies within ± 2.5 K.

3.3.4 X-ray diffraction

The X-ray diffraction (XRD) patterns of the cast samples were recorded in order to identify the phases formed upon fast cooling or during heating to elevated temperatures (recording *in situ*). For these investigations, two methods were used: Bragg-Brentano (i.e. reflection) using characteristic radiation produced by commercially available X-ray tubes, and transmission configuration using high intensity high-energy monochromatic synchrotron beam (i.e. bremsstrahlung).

A PHILIPS PW 3020 Bragg-Brentano diffractometer using $CoK_{\alpha 1}$ (λ = 1.78897 Å) radiation was used in the first case. The diffractometer operated at a voltage of 40 kV and a current of 40 mA. It was equipped with a secondary graphite monochromator and a sample spinner. The samples were prepared by crushing the glassy alloys into small pieces and bonded into amorphous resin in order to have a good resolution. The intensities were measured at 2θ values from 20° to 90° with a step size of $\Delta(2\theta)$ = 0.025° and 2 s measuring time per step.

The X-ray diffraction in transmission configuration, using a high intensity high-energy monochromatic synchrotron beam was carried out at the ID11 beamline of the European Synchrotron Radiation Facilities (ESRF) in Grenoble, France. Electrons emitted by an electron gun are first accelerated in a linear accelerator (LINAC) and then transmitted to a circular accelerator (booster synchrotron) where they are accelerated to reach an energy level of $6 \cdot 10^9$ electron-volts (6 GeV). These high-energy electrons are then injected into a large storage ring (844 meters in circumference) where they circulate in an ultra-high vacuum environment (10^{-10} mbar) at a constant energy for many hours. A sketch showing the synchrotron facilities is presented in Fig. 3.8.

The storage ring includes both straight and curved sections. As they travel around the ring, the electrons pass through different types of magnets: bending magnets, undulators and focusing magnets. When the electrons pass through the

bending magnets, they are deflected from their straight path by several degrees. This change in direction causes them to emit photons, the synchrotron radiation. The undulators are magnetic structures, made up of a complex array of small magnets, forcing the electrons to follow an undulating, or wavy, trajectory in the vertical plane. The beams of radiation emitted from the different bends overlap and interfere with each other to generate a much more intense beam of radiation than that generated by the bending magnets. The focusing magnets, placed in the straight sections of the storage ring, are used to focus the electron beam to keep its diameter small and well-defined. The small and well-defined electron beam produces the very bright X-ray beam needed for the experiments. A picture showing a part of the storage ring is presented in Fig. 3.9. More details can be found in [ESRF].

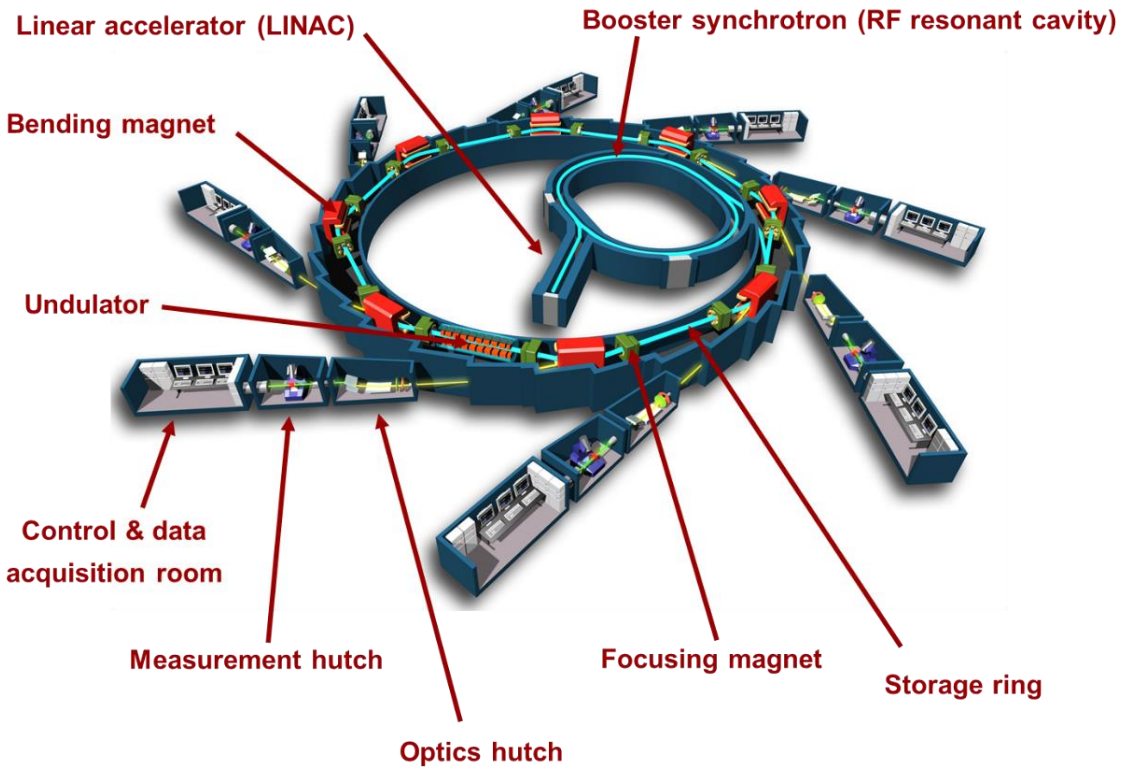

Fig. 3.8 X-ray generation using a synchrotron (picture source: Internet).

This high intensity beam allows the investigation of samples in transmission and *in-situ* at room temperature, as well as during heating and/or cooling. For these experiments, capillary tubes with 1.5 mm external diameter were filled up to a length of 10 mm with small fragments obtained by crushing the as-cast BMG samples or with several ribbon flakes. The tubes were placed in a computer-controlled Linkam hot stage (see Fig. 3.10) and heated or cyclically heated/cooled with 10, 20 or 40 K/min in

the beam. The diffraction images were recorded with a 2D detector, FReLoN 14 bit dynamic CCD camera (**F**ast **Re**sponse **Lo**w-**N**oise **C**harge **C**oupled **D**evice) developed at ESRF [ESRF], and further integrated with respect to radial and azimuthal coordinates on 2D detector using the FIT2D software [Ham96] in order to obtain the diffraction patterns. During the integration the patterns were carefully corrected for the dark current and background. The sample-to-detector distance was calibrated using LaB_6 and CeO_2 NIST standard powders. The Linkam heating device was carefully calibrated using pure (purity at least 99.9%) Sn, Zn, Al and Ge elements. The typical set-up for the synchrotron experiments is sketched in Fig. 3.11.

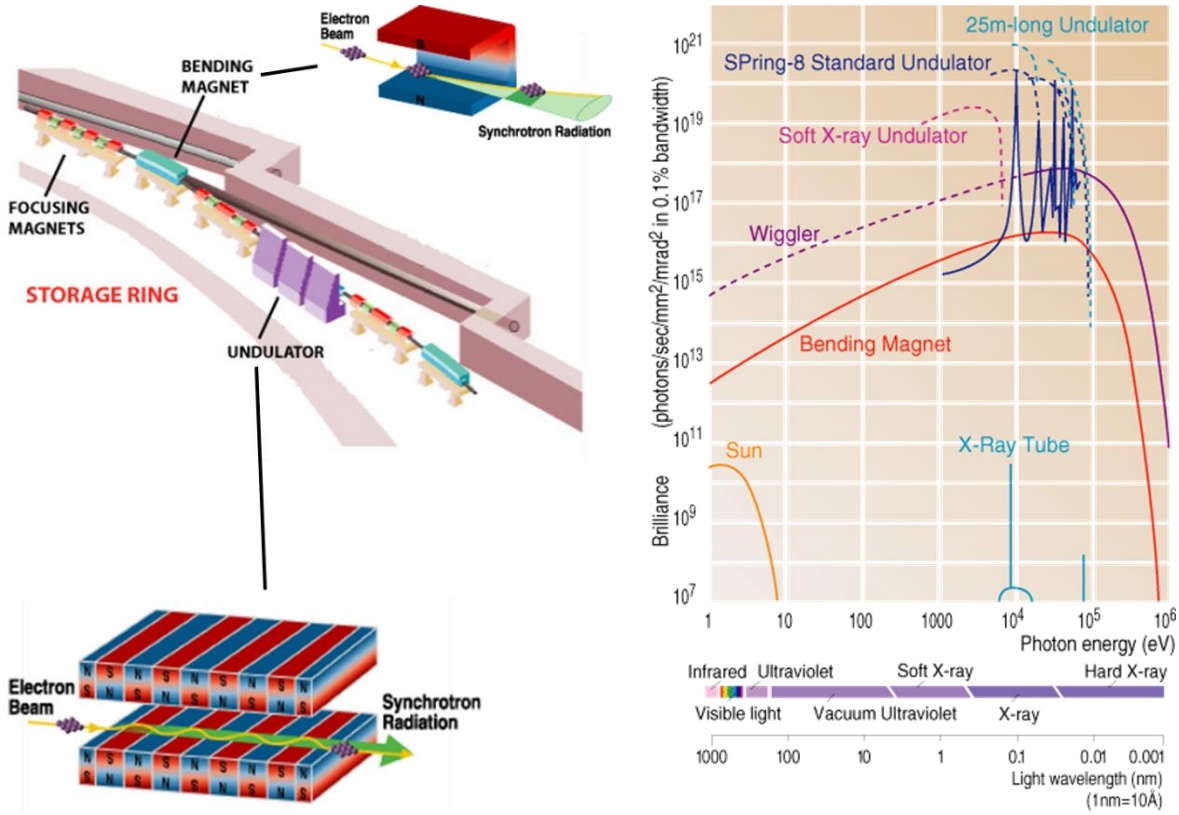

Fig. 3.9 (pictures source: Internet) Left: inside the storage ring. Right: the brilliance of the synchrotron X-ray function of the energy. It is interesting to remark that compared with the commercial X-ray tubes or even with the Sun, the synchrotron radiation has a brilliance up to 10^{10} times higher!

It should be mentioned here that in the actual work the XRD in reflection configuration did not bring the desired details and accuracy. The method limits the investigations to small sample's volume, while with the help of synchrotron radiation every cylindrical sample was continuously scanned along its axis, given very accurate

structural details. This is why further on this actual work the XRD in Brag-Brentano is not presented in details.

(a)

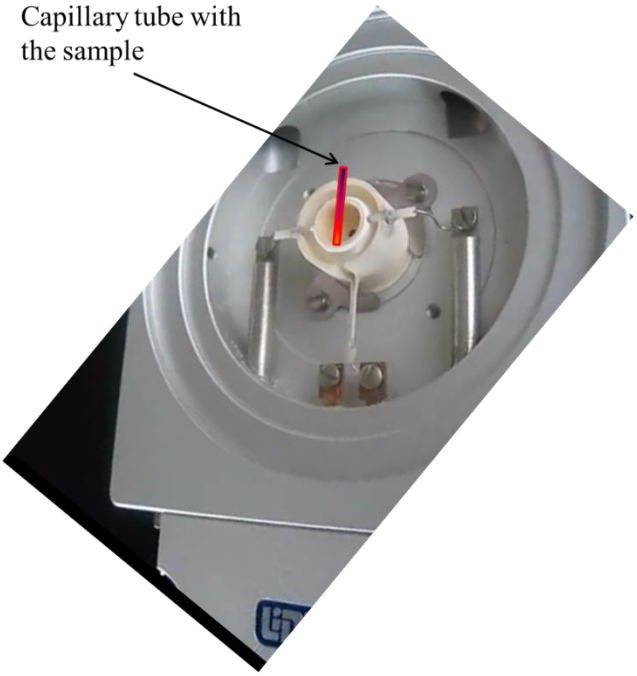

(b)

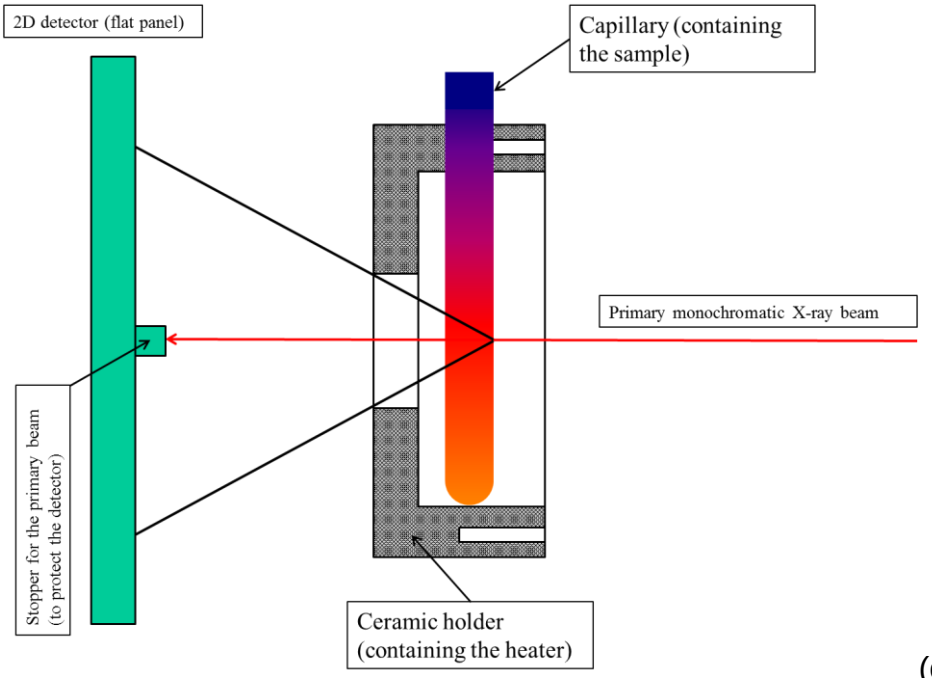

(c)

Fig. 3.10 The Linkam hot-stage device: (a) picture showing the constructive elements (taken from the manufacturer internet site). One can remark there the ceramic heater where the capillary tube containing the sample is placed. The actual position is sketched in (b) and the real working set-up in (c).

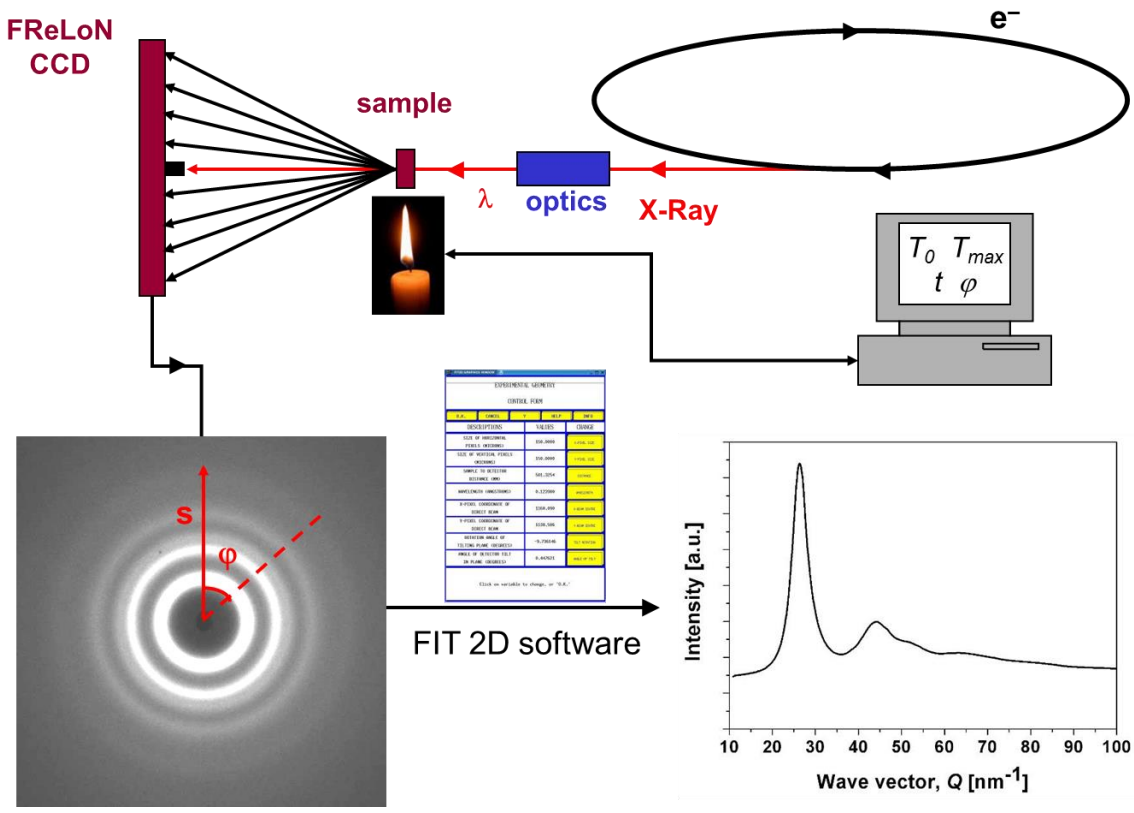

(a)

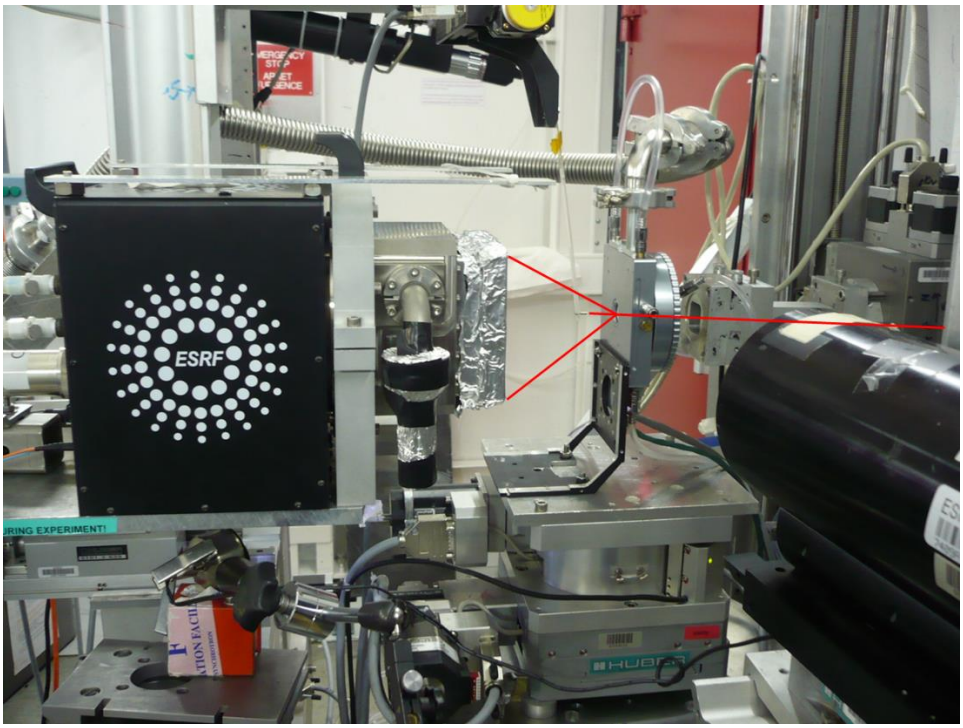

(b)

Fig. 3.11 (a) The typical set-up used for XRD experiments implying the use of synchrotron radiation. (b) Picture showing the actual set-up at ID11@ESRF. With red is drawn the path of the primary (which goes through the sample and it is stopped by the beam-stop) and diffracted X-ray beam.

In order to facilitate the comparison and for better physical understanding, the diffracted intensity *I* in the case of synchrotron XRD is plotted as a function of the wave vector $Q = (4 \cdot \pi \cdot \sin\theta) / \lambda$, where θ is half of the scattering angle. The maximum value for the wave vector *Q* was set to 100 nm^{-1}. Accordingly, an accidental shift of the sample position with 0.1 mm along to the beam direction would result in a shift by 0.006 nm^{-1} for the maxima centered around 31 nm^{-1} and 0.01 nm^{-1} for the maxima centered around 52 nm^{-1}.

3.3.5 Electron microscopy

The microstructure of selected samples was additionally investigated by electron microscopy, using the scanning electron microscope (SEM) and the transmission electron microscope (TEM). The appearance of the as-broken surface of some samples and master alloys was analyzed by means of a Hitachi TM 1000 tabletop SEM, equipped with a four-quadrant semiconductor detector (i.e. back scattered electron detector) and with a BRUKER energy dispersive X-ray (EDX) detector. The sample were simply washed in an ultrasound bath using acetone as cleaning agent prior SEM investigations.

The TEM investigations were performed using a TECNAI G2 F20 microscope. The thickness of the samples was reduced to around 100 μm by manual grinding and then a spherical cavity with a thickness at the center smaller than 5 μm was made in the samples by grinding and polishing using a dimple grinder Gatan 656. The samples were then made electron-transparent at the center of the cavity region by ion milling using a Gatan 691 Precision Ion Polishing System (PIPS) at room temeprature. The voltage of the ion beam was 2.7 KV, the angle was 5 – 6 ° and the ion milling time duration was around 70 hours.

3.4 Magnetic measurements

3.4.1 Measurement of coercivity

For measuring the coercivity of the very soft magnetic alloys a DC Förster Coercimat was used. Its principle of operation is briefly sketched in Fig. 3.12. The magnetizing field was set to 200 kA/m for a magnetizing time of 10 seconds. When the sample is magnetized and the main field attains again zero, the sample will have a residual magnetization, which causes a stray field proportional to the magnetization.

This field can be reduced to zero by applying a magnetic field in the opposite direction compared to the magnetizing field. If the magnetizing field is in the positive sense, the field used to reduce the remanence to zero gives $-H_c$. The device can change the sense of the magnetizing field. This allows to measure the $+H_c$ also. The absolute value of the coercivity is the average of these two values: $H_c = (H_c^+ - H_c^-)/2$. The accuracy of the experimental data lies within ± 0.1 A/m.

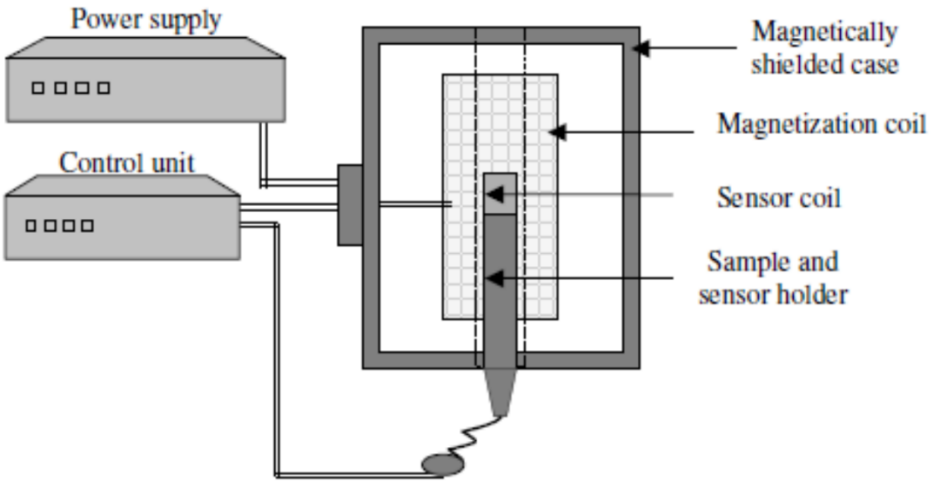

Fig. 3.12 The principle of the coercimat.

3.4.2 Vibrating sample magnetometer

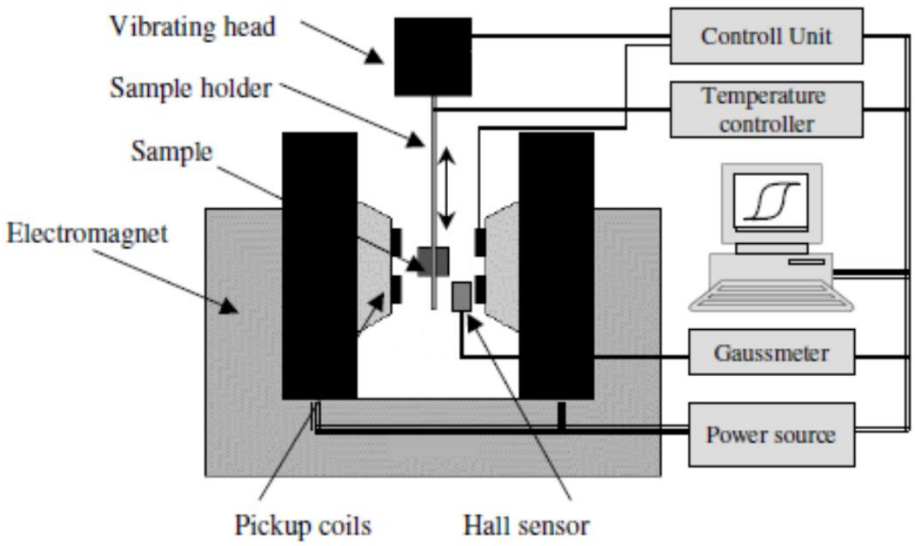

Fig. 3.13 The vibrating sample magnetometer.

The Vibrating Sample Magnetometer (VSM) is an instrument designed to continuously measure the magnetic properties of materials as a function of temperature and field. In this type of magnetometer, the sample is vibrated up and down in a region surrounded by several pickup coils (see Fig. 3.13). The magnetic sample is thus acting as a time-changing magnetic flux, varying inside a particular region of fixed area. From Maxwell's law it is known that a time-varying magnetic flux is accompanied by an electrical field [Kne62] and the field induces a voltage in the pickup coils. This alternating voltage signal is processed by a lock-in amplifier, in order to increase the signal to noise ratio. The result is a measure of the magnetization of the sample.

Magnetic DC fields up to 20 kOe ($\mu_0 H$ = 2 T) can be applied to the sample with a large electromagnet. The field produced by the electromagnet is measured by a Hall probe. A cryostat can be inserted to vary the temperature from 77 to 300 K and a resistive furnace is available, which allows to heat the sample to 1250 K. The used VSM was provided by LakeShore and it is computer-controlled via a 735-type VSM Controller, a 340-type temperature controller and a 450-type gaussmeter. The accuracy of the experimental data lies within ± 80 A/m (i.e. ~ 1 Oe).

3.4.3 Faraday magnetometer

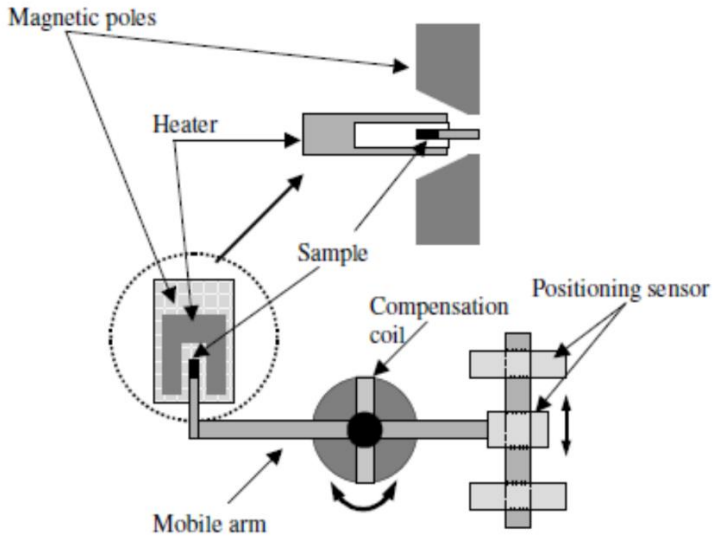

Fig. 3.14 The Faraday magnetometer.

In order to determine the Curie temperature T_C, a computer-controlled Faraday magnetometer was used (Fig. 3.14). The device consists of a mobile lever, which can

rotate without friction in an air bearing. One end of the arm contains the sample and it is placed between two poles of a permanent magnet which produces a DC magnetic field of about 0.55 T, i.e. a field high enough to saturate the samples. The poles of the magnet are non-symmetrical in order to generate a field gradient. In this way, the sample is forced to move in that region where the field is higher. The tip with the sample is inserted into a small resistive heater, which can assure heating and cooling at constant rates, from room temperature to 1000 K. The temperature is measured by a thermocouple, which is in contact with the sample. Changes in the sample temperature will modify the value of its magnetization, i.e. will modify the force on the sample in the magnetic field gradient, which causes a rotation of the mobile arm.

At the end of the mobile arm, a pair of small coils, which act as positioning sensors, is placed. The arm is rigidly mechanically coupled with a coil, which can rotate around a permanent magnet and which can be passed by a DC current. This coil is named compensation coil, because the rotation of the mobile arm produced by interaction between sample and the magnetic field gradient (as was described above) can be counterbalanced by adjusting the current which passes through the coil. Thus, the variation of the current is proportional to the variation of the magnetization and the computer can automatically register the magnetization as a function of temperature. Before the measurements, the magnetometer was calibrated by Ni-samples.

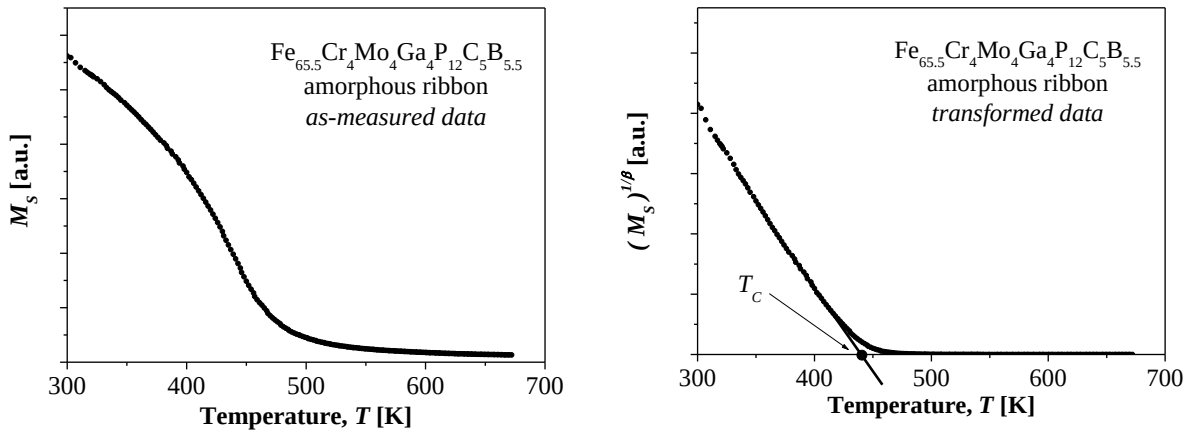

Fig. 3.15 Experimental raw data (a) and transformed data (b) used to determine the Curie temperature. The data from this example were measured for $Fe_{65.5}Cr_4Mo_4Ga_4P_{12}C_5B_{5.5}$ amorphous ribbon.

For temperatures close to T_C, the saturation magnetization can be described by [Her89]:

$$M_S(T) = M(0) \cdot \left(1 - \frac{T}{T_C}\right)^{\beta} \tag{3.2}$$

with the exponent β = 0.36. In order to minimize the errors, the experimental results (Fig. 3.15 (a)) were plotted as $(M_S)^{1/\beta}$ versus T (Fig. 3.15 (b)). The Curie temperature was considered the temperature were the $(M_S)^{1/\beta}$ deviated from linearity (see the black spot from Fig. 3.15 (b)). The accuracy of the experimental data for thermomagnetic curves lies within ± 2.5 K.

Chapter 4
Glass-forming ability of $[(Fe_{0.5}Co_{0.5})_{0.75}B_{0.2}Si_{0.05}]_{96}Nb_4$ alloy

4.1 The master alloys

Several master alloys were prepared using different ingredients, methods and at different laboratories. The details are given in the following. The coding takes in account the name of the labs (i.e. IFW or OCAS), as well as their places (Dresden, Germany and Zwijnaarde, Belgium, respectively) and the used pre-alloys or pure elements. Additionally, if there several master alloys were prepared using the same procedure, the name can bear as suffix a numeral (as for example ZW-Bin2).

DD-FeB: master alloy made in Dresden, using pure elements from IFW plus a laboratory designed FeB pre-alloy available at IFW. Melting procedure: arc melting.
ZW-Bin: master alloy made in Zwijnaarde, using ingredients and pre-alloys from OCAS (FeB, FeSi, FeNb, final composition adjusted with pure Fe and pure Co). Melting procedure: cold crucible.
DD-Bin: master alloy made in Dresden, using OCAS binary FeB, FeSi and FeNb, plus pure IFW Fe and Co. Melting procedure: induction.
DD-Pure: master alloy made in Dresden, using pure elements from IFW. Very clean and laborious procedure, consisting of:

- separate remelting of pure Fe, Co and Nb lumps for cleaning, each 2 times in arc-melter, Ti-gettered Ar atmosphere
- obtaining of the eutectic 75Nb25Fe (wt.%): melting together the cleaned Fe and Nb, 2 times in arc-melter, Ti-gettered Ar atmosphere
- the remelted Fe and Co, plus FeNb, plus B and Si crystals melted together in induction.

DD-Bin-corr: master alloy with a corrected composition, which was made by adding the missing quantities to **DD-Bin** (upon chemical analysis we observed a small compositional deviation from the nominal composition). This observed deviation was not more than 1-2 wt.%, which is normally accepted by large scale processes but important when speaking about laboratory scale.

The purity of the used elements where:

Fe: 99.99 % (lumps, electrolytic)

Co: 99.9 % (lumps, electrolytic)

Nb: 99.9 % (lumps, electrolytic)

B: 99 % (crystalline)

Si: 99.9999 % (single crystal)

The IFW FeB pre-alloy was analyzed only for the main constituents, due to the fact that it was obtained by alloying pure Fe with amorphous B powder. The composition is at the eutectic point (17 at.% B).

The composition and purity of OCAS binary pre-alloys is presented in Table 4.1. The data were taken by the bulletin submitted with the materials (the certificate from the vendor) and are given in wt.%.

Table 4.1 The composition of the used pre-alloys from OCAS, in wt.% (vendor certificate). The empty cells indicate that the content of the searched elements were under the (industrial) detection limit. The Fe content was not directly analyzed, it is obtained by balancing to 100.

	B	**C**	**Al**	**Si**	**P**	**S**	**Cr**	**Mn**	**Nb**	**Fe**
FeB	19.9	0.8	0.5	0.5						78.3
FeSi			1.24	75	0.02	0.06				23.68
FeNb			0.4	1.7					66.7	31.2

As a first important observation here should be mentioned that FeSi has a high concentration of Al and FeNb a high content of Si. Also, upon visual inspection, the FeNb industrial pre-alloy seemed to be inhomogeneous. Most probably this would not affect an industrial process where large quantities are made at once, but at laboratory scale it may shift the final chemical composition of the master alloy. This fact was taken in consideration when the necessary amount for each composition was calculated. Furthermore, the industrial pre-alloys were analyzed also at IFW. Surprisingly, upon chemical analysis conducted at IFW, the Al content in FeSi was found to be **one order of magnitude smaller**. This fact contributed also to the final compositional deviation of the master alloy **DD-Bin**.

As already mentioned, the compositional variation plays a very important role in understanding the GFA. This is why it was necessary for every binary pre-alloy- and

for the master alloys as well- to find out the real composition. The very laborious chemical analysis was carefully conducted in IFW and the results are summarized in Tables 4.2 and 4.3. **Every value is an average of at least 4 experimental measurements** (if the differences are within the measurement errors). Table 4.2 shows the values obtained for the pre-alloys while table 4.3 summarizes those find out for the master alloys, including the composition of two **remelted** master alloys. It is worth to mention that sometimes the remelting of the master alloy increases the GFA. The mechanism responsible for that is related to a). the possibility to dissolve the oxides and b). a better homogeneity of the alloy may be obtained.

Table 4.2 The analyzed composition of the OCAS binary pre-alloys (in wt%). The empty cells indicate that the content of the searched elements were under the detection limit. As can be observed, the FeSi and FeNb pre-alloys were not homogeneous.

	Fe	B	Si	Nb	Al	P	Mn	Ni	Cu	Cr	Ti	Pb	Sn	Co
FeB	79.69	17.32	1.22		0.07	0.01	0.49	0.13	0.12	0.23				
FeSi	25.00 28.55 27.53 26.91		74.62 71.22 72.48 72.94		0.06		0.14		0.02	0.03	0.18			
FeNb	27.09 27.18 25.94 26.88		2.17 2.13 2.09 2.08	68.73 68.87 70.13 68.87	0.07	0.08	0.04		0.01	0.01	0.09	0.07	0.02	0.01

	C	S	O
FeB	0.196	0.0009	0.0218
FeSi	0.008	0.0003	0.0287
FeNb	0.165	0.0420	0.0743

The master alloys **DD-pure** and **DD-Bin-corr** alloys were not analyzed, because their composition have the lowest deviation from the aimed composition. Additionally, other 2 alloys were made, namely **BB-Bin2** and **ZW-Bin2**, at IFW and at OCAS, respectively, using binary pre-alloys. However, they were not used further for casting experiments, due to a relative high difference between the actual and target composition. Their compositions are listed in Table 4.3 as well. The nominal

composition is given as $[(Fe_{0.5}Co_{0.5})_{0.75}B_{0.2}Si_{0.05}]_{96}Nb_4$ in at.%, which means $Fe_{36}Co_{36}B_{19.2}Si_{4.8}Nb_4$ at.% or, after transformation in wt.%,

41.49 Fe 43.78 Co 4.28 B 2.78 Si 7.67 Nb.

As already anticipated, there are significant differences between the chemical composition as-received from the supplier (Table 4.1) and as-analyzed at IFW (Table 4.2). Moreover, the FeSi and FeNb are indeed inhomogeneous. Certainly, the chemical analysis performed at IFW is the most accurate one, due by the standards and calibration samples used here and by the good laboratory conditions.

Table 4.3 The analyzed compositions of selected master alloys (wt.%).

	Fe	Co	B	Si	Nb	C	S	O
DD-FeB	40.86	43.76	4.34	3.21	7.38	0.0200	0.0009	0.0023
DD-Bin	41.03	43.78	3.79	2.83	7.78	0.0420	0.0014	0.0067
DD-Bin-rem	41.03	43.59	3.78	2.73	7.83	0.0425	0.0010	0.0120
ZW-Bin	40.10	43.78	4.29	2.94	7.22	0.0800	0.0102	0.0038
ZW-Bin-rem	39.53	43.48	4.19	2.85	8.44	0.0759	0.0083	0.0040
DD-Bin2	41.63	43.40	3.73	2.83	7.54	0.0570	0.0133	0.0043
ZW-Bin2	37.26	43.97	6.26	3.16	8.30	0.1350	0.0015	0.0031

	Al	P	Mn	Ni	Cu	Cr	total
DD-FeB	0.03	0.01	0.12	0.05	0.04	0.04	**99.86**
DD-Bin	0.02	0.03	0.15	0.06	0.03	0.13	**99.68**
DD-Bin-rem			0.15				**99.57**
ZW-Bin	0.07	0.02	0.16	0.08	0.07	0.17	**98.99**
ZW-Bin-rem			0.12				**98.70**
DD-Bin2	0.12	0.03	0.16	0.11	0.02	0.08	**99.70**
ZW-Bin2	0.14	0.05	0.21	0.10	0.05	0.09	**99.68**

The first observation is that the analyzed compositions of **all master alloys are relatively close to the desired overall composition**. Exception is the alloy **ZW-Bin2**,

which has less Fe and near double amount of B, as well as increased amount of Nb. This can be due by the inhomogeneity of the used pre-alloys, or the inhomogeneity of the master alloy itself. Interesting is also the result obtained by analyzing the remelted alloys. This method of remelting is usually performed with the purpose of increasing the homogeneity of the master alloy. Also, the oxides can be more easily dissolved upon several meltings. Surprisingly, the **DD-Bin-rem** has a larger value of the Oxygen content than the starting master alloy. This indicates that in the original master alloy the oxides were not uniformly distributed. The measurement method cannot make difference between the Oxygen coming from the oxides and the atomic Oxygen which is dissolved in the melt. Interesting is that the in the case of dissolved Oxygen, the GFA may increase because in small quantities the O atoms may behave as the other metalloid atoms.

As a general remark, the alloys made using OCAS FeNb and FeB pre-alloys show a very high content of Carbon. For example, **DD-FeB** has 200 ppm, **DD-Bin** 420 ppm and **ZW-Bin** 800 ppm, content which become even worse in **DD-Bin2** (570 ppm) and **ZW-Bin2** (1350 ppm). Judging from the compositions of the used pre-alloys, the Carbon may come from FeB and/or FeNb. It is not clear in which form the Carbon is present in these pre-alloys (unreacted or as carbonates), but upon remelting- see the case of **ZW-Bin-rem**- the Carbon content slightly decrease (from 800 to 759 ppm). Other aspect worth mentioning is the presence of Sulfur in alloys involving the use of FeNb pre-alloy from OCAS. An abnormal exception is the alloy **DD-Bin** and **ZW-Bin2**, where the Sulfur content is one order of magnitude lower than compared with similar alloys. However, the data are not questionable because, for example, **DD-Bin-rem** has a lower content of Sulfur and upon remelting indeed the Sulfur content seems to decrease- see also the case of **ZW-Bin** and **ZW-Bin-rem**.

4.2 Casting trials: selected results

It was mentioned in Chapter 2 that the Japanese research group of Prof. Inoue has cast $[(Fe_{0.5}Co_{0.5})_{0.75}B_{0.2}Si_{0.05}]_{96}Nb_4$ BMG rods with diameters up to 5 mm and lengths of 5 cm, and if the master alloy is cleaned by fluxing with B_2O_3 prior casting, even 7.7 mm diameter could be obtained. This might be due to the use of very high purity elements, assuring with strictness the predicted/desired chemical composition, and very clean working conditions. For our investigations we tried copper molds, inside

cylindrically-shaped with 2, 3 and 3.3 mm diameter and a length of 5 cm. In most of the cases, i.e. regardless the type of the master alloy used, glassy rods with a full length of 5 cm and 2 mm diameter can be easy obtained. For 3 or 3.3 mm diameter there special efforts should be made. Rods with diameters 4 mm and larger were almost impossible to get (only in some special conditions and not in a reproducible way). Surely, this is primary related to the homogeneity and cleanness of the master alloy. Nevertheless, the casting technique and the operator play also a crucial role, but, as it will be shown in Chapter 5 in the case of Fe-Mo-(P,C,B,Si) alloy, at IFW Dresden **better results as those presented in literature can be anyway obtained**.

Table 4.4 presents selected BMGs prepared using different master alloys. The color code indicates the appearance of the rods, as it was considered at the first glance (i.e. optical aspect of the as-cast surface and as-broken cross-section). However, further structural investigations fully proved these first observations.

Table 4.4 Selected BMGs, together with their amorphicity status.

	DD-FeB	ZW-Bin	DD-Bin	DD-Bin rem	DD-FeB rem	ZW-Bin rem	DD-pure	DD-Bin corr.
2 mm	BUH2122	BUH2121	BUH2120	BUH2124			BUH2160 BUH2161 BUH2162	BUH2163 BUH2164 BUH2165
3.0 mm							BUH2168	BUH2167
3.3 mm	BUH2127	BUH2134 BUH2135	BUH2138 BUH2139	BUH2125 BUH2126 BUH2140 BUH2141	BUH2130 BUH2131 BUH2132 BUH2133	BUH2136 BUH2137	BUH2154 BUH2155 BUH2156 BUH2157 BUH2158 BUH2159	BUH2166

	amorphous
	partially amorphous
	crystalline

Table 4.4 gives a global impression of the GFA. The master alloys **DD-FeB** and **ZW-Bin** showed from the beginning a quite good GFA. **DD-Bin** increased its GFA upon remelting. **DD-pure** and **DD-Bin-corr** show even better GFA. From **DD-FeB-rem** even a 3.3 mm diameter BMG was possible to cast, but this is just one samples from several crystalline others. Therefore this is a particular result and not a repeatable one.

Master alloys **DD-FeB**, **DD-Bin, ZW-Bin**

DD-Bin is the "worst" one. Only partial amorphous rods, even with only 2 mm diameter, were cast. It has the highest O content among the 3 mentioned master alloys. C and S seems to play no role here, as well as the other metal impurities. But the master alloy is depleted in B (3.79 instead of nominal 4.28 %) and taking in account that these are wt.%, the transformation in at.% shows a significant difference. Interesting is that from the 3 mentioned alloys, **DD-Bin** is the only one with Fe content close to the nominal content, but the GFA seems to be more sensitive to the metalloid content. This could be understood if one looks at the role of the metalloids in the amorphous structure. If we assume that the random arrangement of the atoms follows the Matsubara/Poon models [Mat01, Poo03], the small atoms are more important than the medium or large atoms. Further studies on crystallization behavior bring more light on this matter (by detecting the primary crystallization products).

Master alloy **DD-Bin-rem**

Upon remelting, the **DD-Bin** seems to increase its GFA up to an acceptable level. The level of other elements as Cu, Ni and Cr diminishes (i.e. under detection limit), but the enhanced GFA does not come from there- the content are anyway very small. Looking at the main elements, one may notice that the overall composition doesn't change much, the B content remains almost the same (i.e. half percent lower than the nominal), but the O content almost doubled. This is a very important finding. If it is supposed (as discussed previously) that the bad GFA of **DD-Bin** is generated by the depletion in B, the only conclusion is that further the O plays the role of a metalloid in the entire frame. This scenario is feasible if the O, which probably was initially bonded there in oxide(s), is dissolved after remelting. In other words, up to a certain level, **the O has a benefit on GFA**. How much this level is, one cannot know exactly- but it can be somehow predicted. The O radius is smaller than B radius, and it may

play the role of the small atom around Fe or Co atoms in the Poon model of the reinforced backbone [Poo03].

Master alloys **DD-pure, DD-Bin-corr**

These alloys have the best GFA. This is very understandable- and expected- because they are the cleanest and have the designed composition. This proves once again that the **purity of the used elements** plays a critical role. However, the performances announced by the Japanese group (i.e. 5 mm diameter) were not achieved.

Master alloys **DD-FeB-rem, ZW-Bin-rem**

These master alloys, upon remelting, increase their GFA, but not significant. The actual composition of the **DD-FeB-rem** was not checked, but it is supposed that it eventually change within the measurement errors, because for its manufacturing only pure elements were used (the FeB pre-alloy ways made at IFW, i.e. under laboratory conditions). The **ZW-Bin-rem** also does not change the real composition, and, as a consequence, the GFA remains the same.

As an additional detail, the melting (and ejection) temperature is also an indication of the compositional variation. For example, the BMGs made using **DD-pure** and **DD-Bin-corr** were ejected at the same temperature of 1250°C. **DD-FeB** and **ZW-Bin** required a higher temperature (1275 °C), **DD-Bin** even higher (1300 °C), and **DD-Bin-rem** can be again ejected at a temperature toward 1250°C. Moreover, the experimentally observed melting behavior of this alloy composition (regardless the used ingredients) shows that the composition is **not** an **eutectic** one. This means that the alloy should be ejected at a temperature above the liquidus. In the same time, if the casting temperature is too high, is not possible to achieve the proper cooling rate for amorphisation. In order to understand all these aspects, and because one single investigation method does not provide enough details regarding the real nature of the structure, few samples were studied exhaustively and the results are presented in the following.

4.3 GFA as determined from several investigation methods

The amorphicity of the samples was determined by several kinds of measurements. The most sensitive one is the coercivity measurement. If there are no crystals, the coercivity is less than 10 A/m. A small volume fraction of crystalline inclusions, which normally cannot be detected with the regular in-reflection X-ray diffraction studies, may be responsible for an increasing of the coercivity up to 15-20 A/m. This is valid only when one compares samples with the same geometry, in fact with the same length. Due to technical reasons (the gauge coils of the device itself), for coercivity measurements we selected always rods with a length of 20 mm. In this way we are in approximation of an infinite cylinder, which approximates the ideal shape of a revolution ellipsoid. The device used for DC coercivity measurements is a commercial one, provided by Dr. Förster Institute (Germany) and which was in-detail described in the subchapter 3.4.1.

As mentioned in the subchapter 2.2.1, the crystallization enthalpy may be used as well as a measure of the amorphicity degree (higher the enthalpy, more amorphous is the sample). But this is 100% true only if one compares samples cast from *the same* master alloy. Different master alloys, with variations of the actual composition, may give fully amorphous samples but with a slightly changed topological short-range order and this can influence the crystallization behavior.

The density modification can, at least theoretically, give an idea about the amorphicity as well. The alloy in the glassy state should have a density lower than in the crystalline state. However, even the density values are true, their interpretation can mislead. This is because all glasses have in their structure such named “free volume” which affects the density. This free volume appears as a consequence of the rapid quenching from the melt (kinetic freezing of the liquid state) and it can be completely released by annealing. Moreover, by releasing the free volume the glass tends to achieve the density characteristic for a dense packed structure, i.e. for its crystalline state. The density was checked only for few samples, the experimental difficulty (i.e. device constructed to use the Arhimede’s law and very small sample prone to huge errors in measuring the actual volume) being another factor which may give false information.

Table 4.5 summarizes measured data for some of the samples chosen for detailed investigation. If one consider the coercivity measurements as a pertinent

gauge, the fully amorphous samples should be BUH2122 (**DD-FeB**), BUH2160 (**DD-Pure**), BUH2121 (**ZW-Bin**), followed by mixt glassy samples BUH2124 (**DD-Bin-rem**), BUH2161 (**DD-Pure**), BUH2164 (**DD-Bin corr**), BUH2163 (**DD-Bin corr**) and the last BUH2120 (**DD-Bin**), about which no doubt that it contains a quite high amount of crystals. There are samples even of the same composition, but with different structures.

Table 4.5 Measured data for selected samples of different master alloys: coercivity H_c, density ρ, crystallization enthalpy (endothermic) ΔH, saturation magnetization M_s, saturation polarization J_s (calculated as $\mu_0 \rho M_s$), glass transition temperature T_g, crystallization temperature T_x, extension of the supercooled liquid region (SLR) $\Delta T_x = T_x - T_g$, liquidus temperature T_{liq}, reduced glass-transition temperature T_{rg} and parameter $\gamma = T_x / (T_g + T_{liq})$. The DSC data were measured upon isochronal heating with 20K/min heating rate.

Sample name	**BUH 2122**	**BUH 2160**	**BUH 2161**	**BUH 2121**	**BUH 2120**	**BUH 2124**	**BUH 2163**	**BUH 2164**
Master alloy	**DD-FeB**	**DD-pure**	**DD-pure**	**ZW-Bin**	**DD-Bin**	**DD-Bin rem**	**DD-Bin corr**	**DD-Bin corr**
Hc [A/m]	4.5	2.7	25.3	2.7	234	15.5	57	47.7
ρ [g/cm^3]			7.6896	7.6343		7.6854		
$-\Delta H$ [J/g]	42.14	38.5	37.5	43.84	32.2	37.16	44.28	40.87
M_s [Am^2/kg]	105	110	109	104	111	110	106	105
J_s [T]	1.01	1.06	1.05	1.00	1.06	1.06	1.02	1.01
T_g [K]	833	824	821	830	813	811	825	823
T_x [K]	872	857	854	864	847	844	861	860
ΔT_x [K]	39	33	33	34	34	33	36	37
T_{liq} [K]	1495	1473	1474	1496	1468	1500	1489	1487
T_{rg}	0.55	0.56	0.56	0.55	0.55	0.54	0.55	0.55
γ parameter	0.375	0.373	0.372	0.371	0.371	0.365	0.372	0.372

Excepting the sample BUH 2120, all other seemed to be amorphous as it is marked also in Table 4.4. The **X-ray diffraction studies in Bragg-Brentano**

configuration showed only minor differences, within the detection limit, therefore they are not shown here. In turn, as it will be presented later, transmission XRD and TEM were performed in order to find-out the real structure. Besides no appreciable differences in the XRD patterns, from Table 4.5 one can observes that **the reduced glass-transition temperature T_{rg} and the γ parameter do not show any noticeable difference.** Hence, the thermodynamic parameters that should give the best information about the GFA **predict an identical GFA** for all exemplified master alloys- which is not the case as already seen upon casting.

The DC saturation magnetization M_s (and the saturation polarization J_s (calculated as $\mu_0 \rho M_s$) as well) takes almost the same value for all investigated samples. The saturation magnetization does not strictly depend on the amorphicity degree. Surely, it is higher for samples which already developed some crystalline inclusions (if they are magnetic, like α-Fe, Fe_2B or Fe_3B) or smaller if the crystalline products are not magnetic, but the most important is the shape of the hysteresis loop. For a fully (and relaxed) amorphous sample, it tends to be perfectly rectangular, showing a very small magnetic energy (i.e. the area included by the hysteresis is small). More accurate would be magnetic measurements in AC fields, but there is a technical problem: in order to minimize the errors, a closed magnetic circuit is required, i.e. the samples must be under ring shape. Due to their intrinsic brittleness, it is almost impossible to cast a geometrically perfect, fully amorphous ring. Therefore, the data are limited to the DC hysteresis- and they are presented in details in the following.

4.3.1 Same master alloy, samples with different degree of amorphicity

Let's consider samples BUH2160 and BUH2161. For simplicity, their detailed results are summarized in Table 4.6. Both samples are made using **DD-Pure**, but BUH2160 seems to be "more amorphous" than BUH2161 (2.7 A/m versus 25.3 A/m). Figure 4.1 shows the DSC traces of these samples. The BUH2160 sample has a bit higher T_g and a higher T_x, but ΔT_x is the same. Also, the crystallization enthalpy is just slightly higher for fully amorphous sample (see Table 4.6), the melting is almost at the same temperature and the reduced glass transition temperature takes the same value. Also, the general behavior is the same for both samples.

Table 4.6 Extras from Table 4.5, details for BUH2160 and BUH2161. The notations and the measurement units are as usual (and described previously).

		H_c	$-\Delta H$	M_s	J_s	T_g	T_x	ΔT_x	T_{liq}	T_{rg}	γ
BUH 2160	**DD-pure**	2.7	38.5	110	1.06	824	857	33	1473	0.56	0.373
BUH 2161	**DD-pure**	25.3	37.5	109	1.05	821	854	33	1474	0.56	0.372

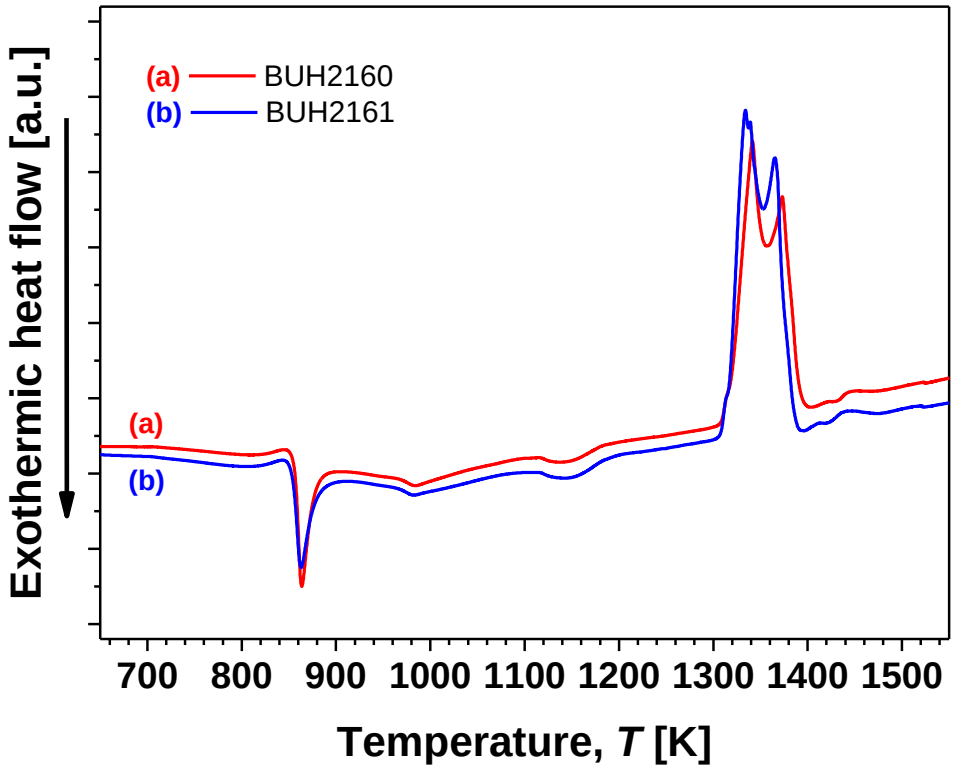

Fig. 4.1 Two samples made from **DD-Pure** master alloy. The sample BUH2160 (curve a) is "more amorphous" than BUH2161 (curve b).

Fig. 4.2 shows the corresponding DC hysteresis loops measured for samples BUH2160 and BUH2161. The first sample (curve a, in red) is "more amorphous" than the second one (curve b, in blue). As it was mentioned previously, the saturation magnetization takes almost the same values, but the tendency is to become more rectangular. No real difference between the magnetic energies (area included by the loop). However, the detection limit of 1 Oe (= 79.9 A/m) makes the VSM useless for accurate measurements of coercivity (therefore it was measured with the coercimat). However, both samples show almost no magnetic remanence, which is a clear advantage in applications which require very soft magnetic materials.

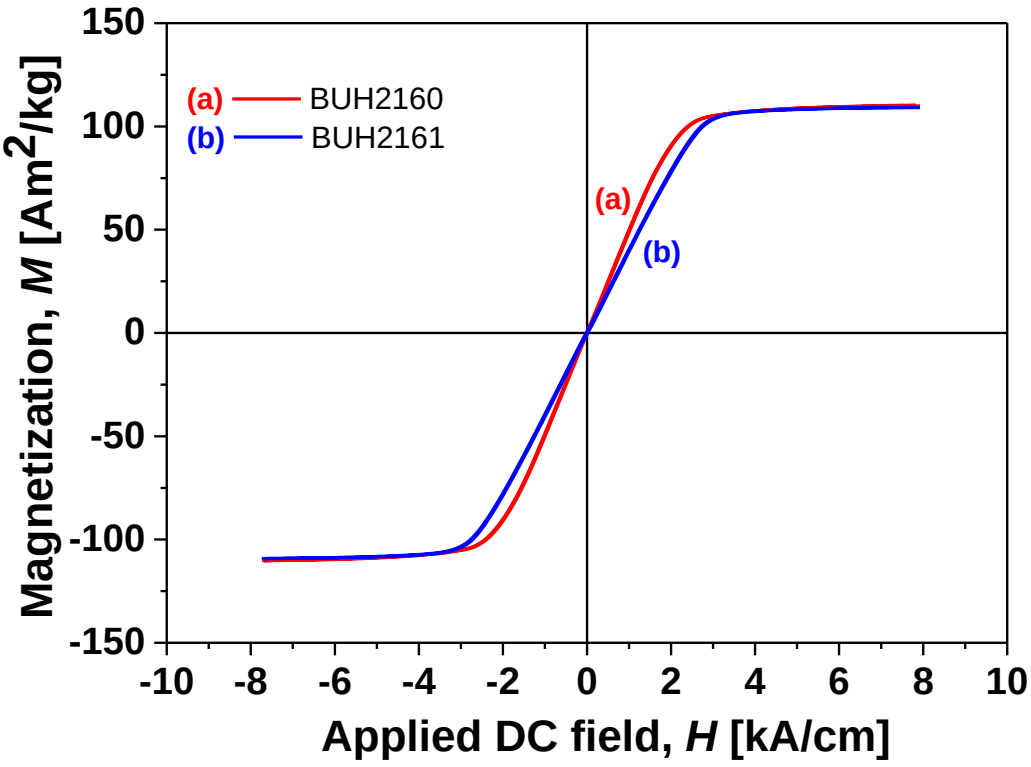

Fig. 4.2 Hysteresis loops for samples made from the same master alloy but with different degree of amorphicity.

4.3.2 Different master alloy, different degree of amorphicity

This is the case of the samples BUH2121 and BUH2120, i.e. fully amorphous and composite. The measurement details are summarized in Table 4.7 and the corresponding DSC traces are shown in Fig. 4.3, while in Fig. 4.4 are given the hysteresis curves.

Table 4.7 Extras from Table 4.5, details for BUH2121 and BUH2120. The notations and the measurement units are as usual (and described previously).

		H_c	$-\Delta H$	M_s	J_s	T_g	T_x	ΔT_x	T_{liq}	T_{rg}	γ
BUH 2121	**ZW-bin**	2.7	43.84	104	1	830	864	34	1496	0.55	0.371
BUH 2120	**DD-bin**	234	32.2	111	1.06	813	847	34	1468	0.55	0.371

Here it is clear that the crystalline sample displays a crystallization enthalpy smaller than the one measured for fully amorphous sample. Also, the glass transition and crystallization take place earlier, the melting as well, but, surprisingly, not only the

T_{rg} and γ parameter are the same but also the extension of the SLR takes the same values for both alloys- so theoretical it indicates the same GFA. This might be understand and explained in the following way. The BUH2120 sample consists of crystals embedded in an amorphous matrix. The overall compositions of both samples are (almost) identical, but the amorphous matrix in BUH2120 has different composition as BUH2121 sample. Therefore, the thermal stability data come from a different amorphous alloy- and so the main parameters may take similar values.

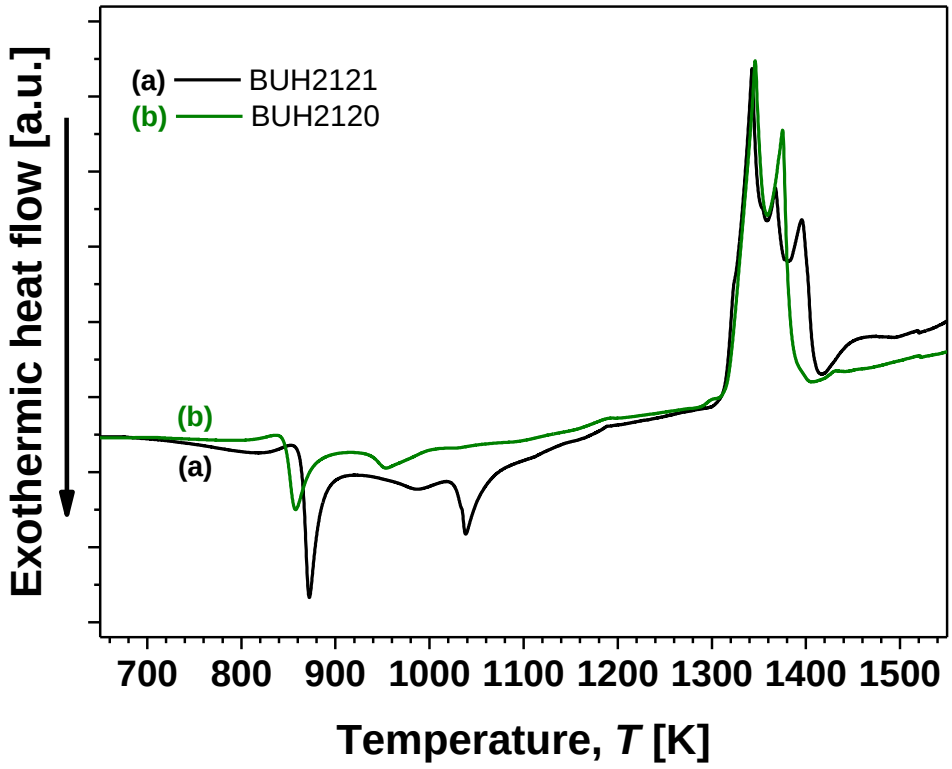

Fig. 4.3 Comparison between BUH2121 (**ZW-Bin**, fully amorphous, curve a) and BUH2120 (**DD-Bin**, mixture amorphous/crystalline, curve b).

The sample which is fully amorphous (BUH2121, curve a in Fig. 4.4) shows here a reduced saturation magnetization. This can be explained by the fact that the crystals which are formed in BUH2120, the sample with crystalline inclusions, are soft ferromagnetic. We suppose that there a solid solution of the type α-(Fe,Co) was formed. It is known that the saturation magnetization of such products may reach even more than 2.2 T (over 200 Am^2/kg) [Her97]. Such structures will be detailed later, showing the X-ray studies.

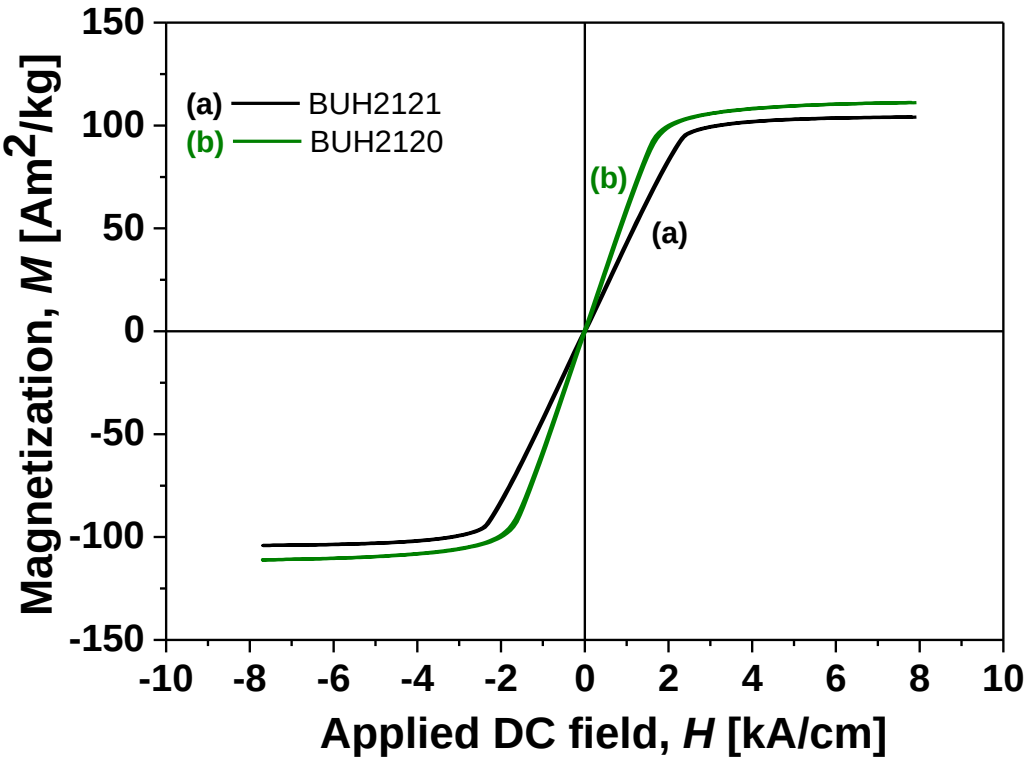

Fig. 4.4 Hysteresis curves for different samples, different master alloy: BUH2121 (**ZW-Bin**, fully amorphous, curve a) and BUH2120 (**DD-Bin**, mixture amorphous/crystalline, curve b).

4.3.3 Related master alloys, different degree of amorphicity

Table 4.8 Extras from Table 4.5, details for BUH2120, BUH2124 and BUH2164. The notations and the measurement units are as usual (and described previously).

		H_c	$-\Delta H$	M_s	J_s	T_g	T_x	ΔT_x	T_{liq}	T_{rg}	γ
BUH 2120	**DD-bin**	234	32.2	111	1.06	813	847	34	1468	0.55	0.371
BUH 2124	**DD-bin-rem**	15.5	37.16	110	1.06	811	844	33	1500	0.54	0.365
BUH 2164	**DD-bin-corr**	47.7	40.87	105	1.01	823	860	37	1487	0.55	0.372

Figure 4.5 shows the DSC behavior of BUH2120 (**DD-Bin**), BUH2124 (**DD-Bin-rem**) and BUH2164 (**DD-Bin-corr**). Here different measurements give divergent data. According to the coercivity measurements, the order should be BUH2120, BUH2164, BUH2124. The enthalpy would indicate BUH2120, BUH2124, BUH2164, while the extension of the SLR and γ parameter indicate BUH2124, BUH2120, BUH2164 (all these data are detailed in Table 4.8). This is a typical example of composite samples,

where the amorphous matrices may have slightly different composition, therefore the direct comparison is misleading and should be made with carefulness.

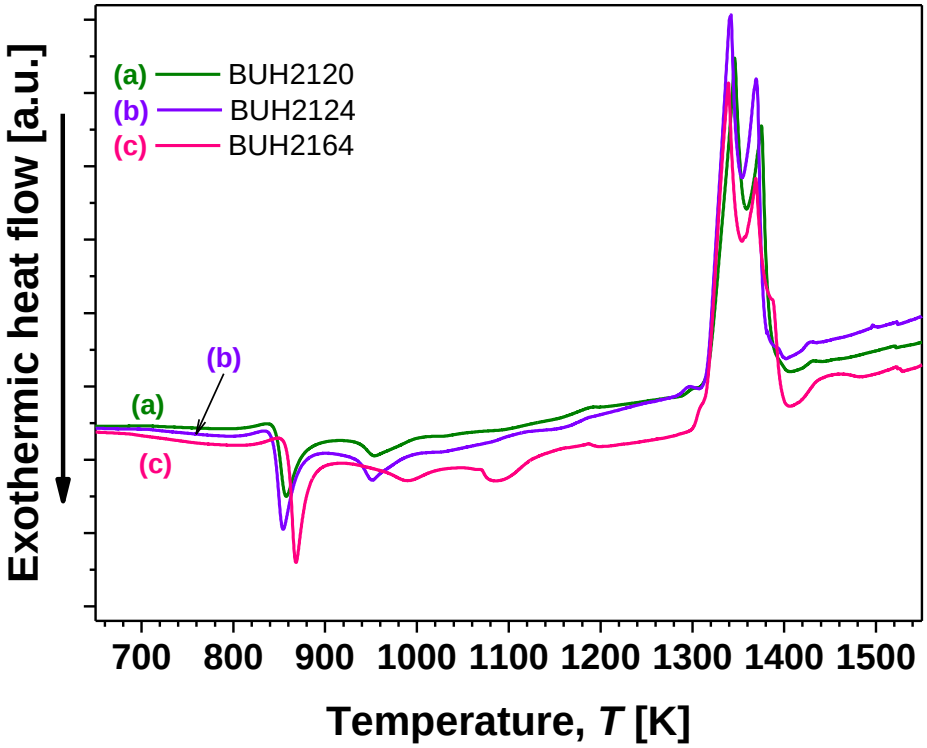

Fig. 4.5 Comparison between BUH2120, BUH2124 and BUH2164.

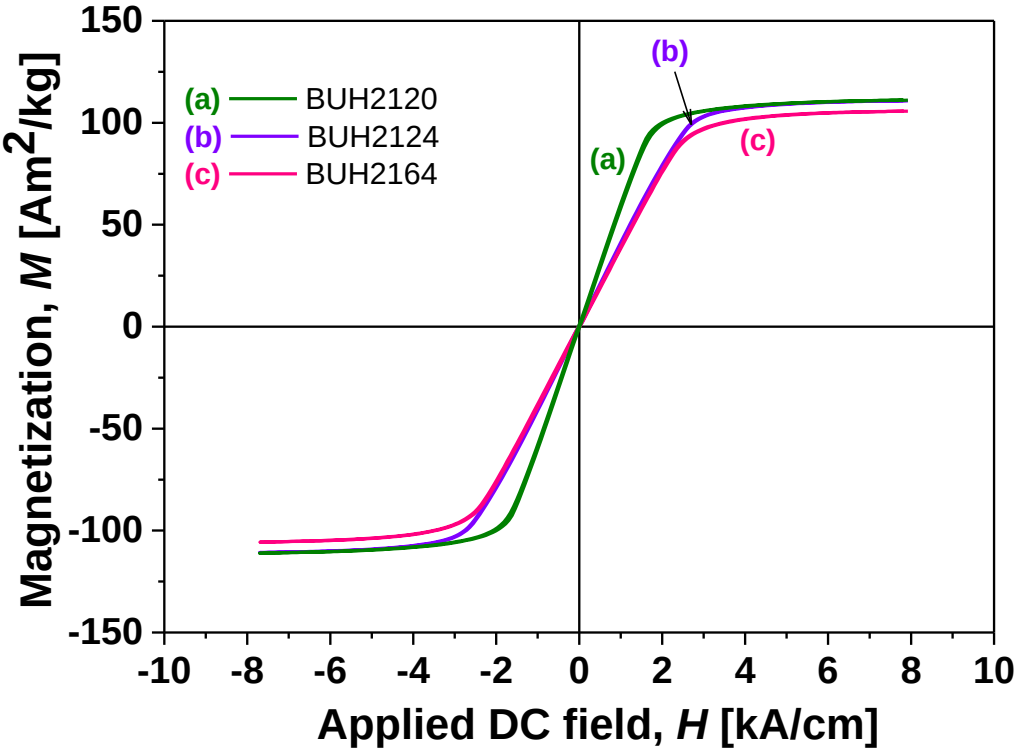

Fig. 4.6 BUH2120 (**DD-Bin**), BUH2124 (**DD-Bin-rem**), BUH2164 (**DD-Bin-corr**), magnetization loops.

Fig. 4.6 shows the VSM loops of BUH2120 (**DD-Bin**), BUH2124 (**DD-Bin-rem**) and BUH2164 (**DD-Bin-corr**). The other measurements have shown already that is not very clear how the GFA increases (or varies). As for the other samples, the "more" amorphous the sample, the lower the saturation. However, all features are so close, that the small differences can even be considered to be within the measurements errors, i.e. artefacts coming from the VSM itself, a misalignment of the sample in the easy magnetization axis etc.

4.3.4 Different master alloys, fully amorphous samples

This is by far the most interesting case, where one should see exactly the differences brought by the different ingredients. For simplicity, Table 4.9 shows the details only for these samples: BUH2122 (**DD-FeB**), BUH2160 (**DD-Pure**) and BUH2121 (**ZW-Bin**). If the extension of the SLR of BUH2160 and BUH2121 is almost the same (i.e. 33 K and 34 K, respectively), and comparable with every other sample, the first one made from **DD-FeB** shows the widest SLR from all: 39 K. It does not show the highest reduced glass transition temperature, but, however, all investigated samples seem to have almost the same T_{rg}. The crystallization enthalpy is also not the highest one (see Table 4.9 or Table 4.5 with all samples), but it is the one with the most interesting crystallization behavior- it shows a second crystallization plus transformation at the highest temperature from all samples (see Fig. 4.7)- which in fact indicates the best thermal stability. For clarity, the thermograms are limited to lower temperatures and no melting is shown. This is an interesting finding. Certainly, in order to find out the influence of the impurities or minor additions on the GFA, one has to study in more details the crystallization behavior of different samples with made from different master alloys. These data will be presented in Chapter 5.

Table 4.9 Extras from Table 4.5, details for BUH2122 (**DD-FeB**), BUH2160 (**DD-Pure**) and BUH2121 (**ZW-Bin**). The notations and the measurement units are as usual (and described previously).

		H_c	$-\Delta H$	M_s	J_s	T_g	T_x	ΔT_x	T_{liq}	T_{rg}	γ
BUH 2122	**DD-FeB**	4.5	42.14	105	1.01	833	872	39	1495	0.55	0.375
BUH 2160	**DD-pure**	2.7	38.5	110	1.06	824	857	33	1473	0.56	0.373
BUH 2121	**ZW-bin**	2.7	43.84	104	1	830	864	34	1496	0.55	0.371

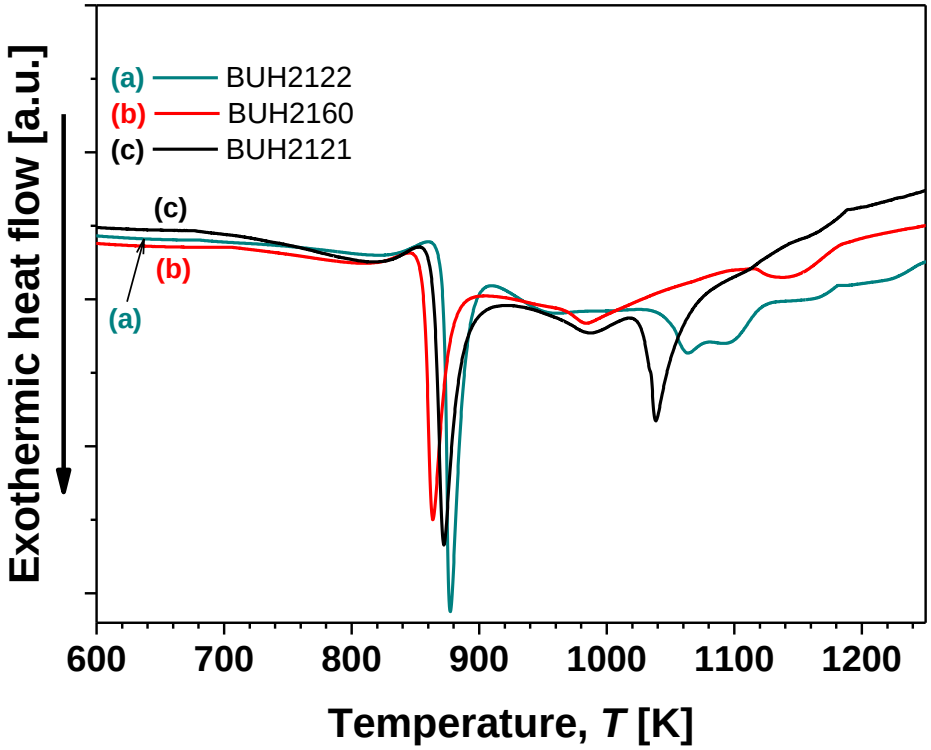

Fig. 4.7 DSC traces for 3 fully amorphous samples (different master alloys). Here only the crystallization events are presented.

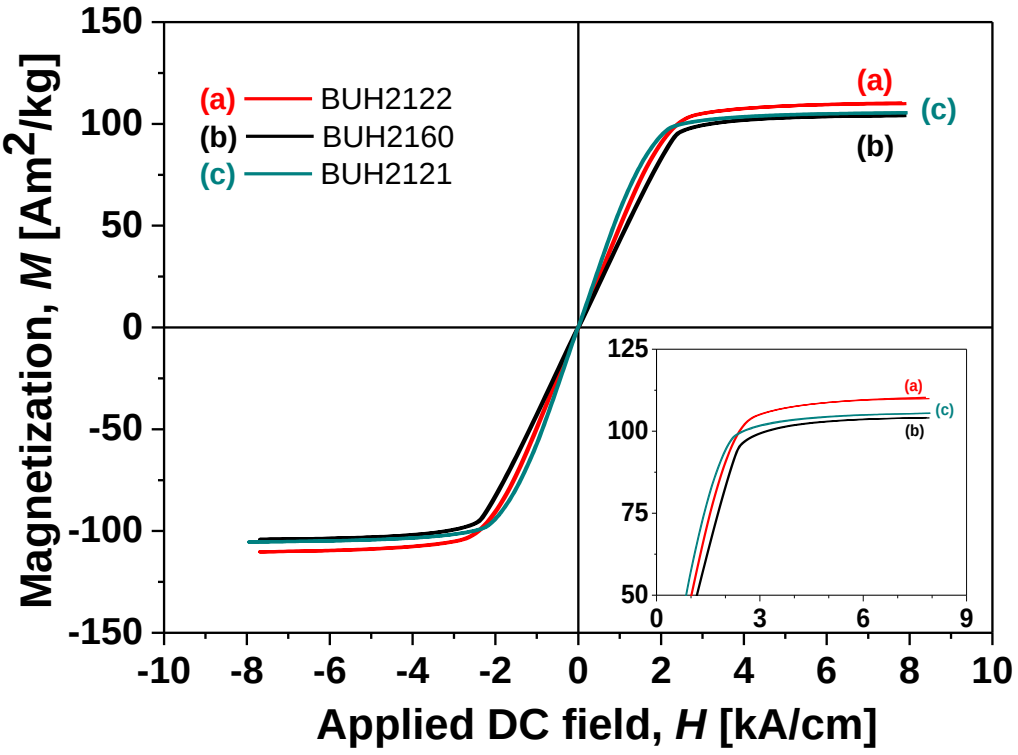

Fig. 4.8 Fully amorphous samples made from different master alloys. The inset shows the behavior by approaching the saturation.

The magnetization behavior for identical samples (see Fig. 4.8) is expected to be identical. At a first glance it is so, but if one looks in details there are small differences, which are visible there when the samples approach the magnetic saturation (the inset in Fig. 4.8). All three samples are amorphous, showing almost the same value of the coercivity and of the parameters which characterize the GFA. However, as can be seen from the inset in Fig. 4.8 and from the Table 4.9, the samples BUH2160 (**DD-Pure**) shows the highest saturation value (110 Am^2/kg), followed by BUH2122 (**DD-FeB**) with 105 Am^2/kg and BUH2121 (**ZW-Bin**) with 104 Am^2/kg. When the samples are fully amorphous, one can apply the Heisenberg theory of the ferromagnetism [Hei28]. In 1928 Heisenberg described the quantum mechanical origin of ferromagnetism, by considering the interaction between electronic spins. The spins of the neighboring electrons are coupled and in this way all the spins are oriented in the same direction. This parallel alignment of the spins gives rise to a macroscopic magnetic moment. Important now is to understand that the saturation magnetization depends on the exchange interaction between spins. At a first glance, it means that the **magnetization** depends on the number of the spins, i.e. the **number of the magnetic atoms** in the analyzed sample, and on the **distance** between them. In our case, the metalloids and other non-magnetic atoms increase the distance between ferromagnetic atoms (Fe and Co) and this is traduced in a lower saturation magnetization that in the case of pure Fe or Co. The things are in reality not as simple as presented here, but roughly we can consider this “model”. Now it is interesting to go back to the composition table (i.e. Table 4.3), from which, for simplicity, some rows are copied and grouped under Table 4.10.

Table 4.10 The real composition of **DD-FeB** (so the sample BUH2122) and **ZW-Bin** (sample BUH2121) master alloys. The composition is given in wt.%, excepting C, S and O for which the number represents wt ppm.

	Fe	**Co**	**B**	**Si**	**Nb**	**C**	**S**	**O**	**Al**	**P**	**Mn**	**Ni**	**Cu**	**Cr**
DD-FeB	40.86	43.76	4.34	3.21	7.38	200	9	23	0.03	0.01	0.12	0.05	0.04	0.04
ZW-Bin	40.10	43.78	4.29	2.94	7.22	800	102	38	0.07	0.02	0.16	0.08	0.07	0.17

The master alloy made using pure elements (**DD-Pure**, not presented here) is the one with the lowest impurities level. This is why the sample BUH2160 shows the highest level of the saturation magnetization. The **DD-FeB** master alloy contains some

non-magnetic impurities (basically C), which lower the saturation of the sample BUH2122. The level of the impurities is even higher in **ZW-Bin** and as a consequence the saturation magnetization of BUH2121 is smaller than those measured for other samples. To other extent, the **DD-FeB** has a bit more Fe than **ZW-Bin**, which also may contribute to the increase of saturation. However, the target is 41.49 wt.% Fe, requirement most probably fulfilled only by **DD-Pure** alloy, which shows the highest saturation magnetization.

4.4 Yttrium additions and its influence on GFA

It is known from literature [Lu03b] that Y may have a positive role in enhancing the GFA. The mechanism contains two aspects. First, as pointed out by Inoue [Ino00], atomic size difference and heat of mixing play important roles in bulk glass formation. Yttrium has the largest atomic radius of 1.80 Å among all constituent elements [ASM92] and a large negative heat of mixing with B (-35 KJ/mol) [Tak05] Therefore, the addition of Y causes the more sequential change in the atomic sizes, as well as the generation of new atomic pairs with large negative heat of mixing. Consequently, the topological and chemical short-range orderings are increased with adequate amount of Y addition, thus increasing the packing density of the undercooled liquid with low atomic diffusivity. This can be revealed by the enhanced stability of the liquid phase; that is, the suppression of the melting due to the primary phases and the decrease in the liquidus temperature. On the other hand, as shown by Z.P. Lu et al. in [Lu03b], too much Y would lead to the precipitation of the $Fe_{17}Y_2$ phase and would deteriorate the GFA.

A second aspect is related to impurities, especially oxides. For example, such impurities may have an adverse effect on glass formation in Zr-based bulk metallic alloys [Sur11]. It is speculated that the GFA of Fe-based BMGs is also sensitive to the Oxygen impurity. However, in the present case, we already shown that some Oxygen dissolved in the master alloy may improve the GFA. Indeed, **dissolved** but **not bonded** there **in an oxide**. The Oxygen impurity can be minimized by neutralizing it through alloying, for example with Y, which is a reactive element.

An additional speculation is related to the fact that Y additions may increase the viscosity of the melt, slowing down the diffusion. All these are theoretical aspects, proved only in some particular cases. We tried to add Y and the results did not become better. The additions were with 0.5, 1, 1.5 and 2 at.% Y, respectively. For that, a master

alloy with moderate GFA were chosen- the **DD-Bin** alloy. Controlled quantities of this alloy were arc melted together with the respective quantities of Y in order to reach the desired composition. The new alloys were relative dirty and oxidized, having **a much higher melting point** that the starting mother alloy and reacted with the quartz crucible used for casting. As a result, **no amorphous rods** were possible to cast, even in 2 or 1 mm diameter.

In order to rule-out the possible influence of the preparation routes, a second set of experiments were done, this time in several steps and **starting from pure elements**. First, a binary eutectic pre-alloy Fe-75Y (wt.%) was made. The second step was to melt in induction the rest of the elements, up to the nominal composition minus the respective quantities of FeY. The third and the last step were to melt together using the cold crucible method (i.e. containerless levitation melting, no contamination with the crucible material) the alloys without Y together with the desired quantities of FeY. From each alloy with Y some rods were cast, but the results were negative. The cast rods were not completely amorphous, only a small volume fraction of amorphous matrix could have been spotted. In conclusion, the **Y addition does not enhance the GFA in the case of $[(Fe_{0.5}Co_{0.5})_{0.75}B_{0.2}Si_{0.05}]_{96}Nb_4$ alloy**.

4.5 The influence of casting atmosphere on GFA

In order to study the influence of the casting atmosphere- and so the Oxygen effect- on the GFA, several rods were cast in atmospheres with different partial Oxygen pressure. This was done by playing with the vacuum level in the casting device. The experimental results are listed in Table 4.11 and the figures which follow show the statistics and the conclusions. All castings were performed using the same **master alloy**, which consisted only of **pure elements**. In order to keep the results reproducible, the castings were limited to 2 mm diameter rod samples with a length of 5 cm.

In details, the working chamber was evacuated prior casting to different pressures and then filled up to a certain pressure with Ar. The second column of Table 4.11 shows that in clear: p_i is the initial pressure down to which the chamber was evacuated and then Δp is the ejection overpressure, which is measured as the difference between the pressure of the chamber after filling with Ar and pressure of the gas in the ejection reservoir (both values are given in the second column in parenthesis). The ejection was performed always with the help of an inert gas (i.e. Ar)

in order to prevent a premature oxidation and to keep the castability. Also, the castings were performed under the same pressure difference of 300 mbar. All samples were characterized visually by direct observation and upon coercivity measurements. For selected rod samples, the Oxygen and Nitrogen contents were measured.

Table 4.11 Samples cast in different Ar or air atmosphere. The oxygen and nitrogen content are given in wt. ppm. The cells marked with green show the best samples. The sample names are made using the letters P (from German word "Probe" = sample) and V (from German word "Versuch" = attempt).

Atm.	Casting details	Sample name	Characteristics	H_c [A/m]	[O]	[N]
Argon	$p_i = 10^{-2}$ mbar Δp = 300 mbar (300/600 mbar)	P1.1_V1	42mm, uniform, some crystals on the surface	44.5		79
		P1.1_V2	30mm, external uniform, structural inhomogeneous	57		
		P1.1_V3	35mm, good looking rod, some crystals at bottom	26	40	36
Argon	$p_i = 10^{-1}$ mbar Δp = 300 mbar (300/600 mbar)	P1.2_V1	31mm, good looking rod, some crystalline islands on the surface	77		
		P1.2_V2	40mm, uniform, small imperfections in the upper part	21	0.01	32
		P1.2_V3	40mm, crystalline	2000		
Argon	p_i = 1 mbar Δp = 300 mbar (300/600 mbar)	P1.3_V1	46mm, mold full, uniform, crystalline islands on the surface	54	0.01	51
		P1.3_V2	45mm, mold full, some crystals on the surface	7.4		39
		P1.3_V3	35mm, crystalline	500		
partially Argon	p_i = 50 mbar Δp = 300 mbar (300/600 mbar)	P1.4_V1	40mm, mold full, good surface, uniform	25.4	8	49
		P1.4_V2	40 mm, mold full, good surface, uniform	6.3		
		P1.4_V3	36mm, crystalline	1300		
Vacuum	$p_i = 10^{-3}$ mbar Δp = 300 mbar (0/300 mbar)	P2.1_V1	35mm, surface imperfections	42		
		P2.1_V2	35mm, bad contact alloy/mold (gases!)	16	9	40
		P2.1_V3	35mm, bad contact alloy/mold, crystalline	5000		

Atm.	Casting details	Sample name	Characteristics	H_c [A/m]	[O]	[N]
Vacuum	$p_i = 10^{-2}$ mbar Δp = 300 mbar (0/300 mbar)	P2.2_V1	Several pieces, crystalline			
		P2.2_V2	31mm, crystalline, bad contact alloy/mold	2750		
		P2.2_V3	30mm, crystalline, bad contact alloy/mold	2500	40	66
Vacuum	$p_i = 10^{-1}$ mbar Δp = 300 mbar (0/300 mbar)	P2.3_V1	33mm, bad surface, crystalline	3000	20	67
		P2.3_V2	30mm, crystalline, bad surface	3500		
		P2.3_V3	40mm, crystalline, bad surface	7000		
Vacuum	p_i = 1 mbar Δp = 300 mbar (0/300 mbar)	P2.4_V1	36mm, bad surface, but looks good in cross-section	144	40	28
		P2.4_V2	33mm, bad surface, interesting cross section	2000		
		P2.4_V3	Small fragments; crystalline			
(partially) air	p_i = 100 mbar Δp = 300 mbar (100/400 mbar)	P2.5_V1	40 mm, mold full, uniform, small regions with bad contact	6		
		P2.5_V2	35mm, surface quite bad, bottom crystalline	60	30	51
		P2.5_V3	42mm, surface bad, crystalline	475		
air	p_i = 1000 mbar Δp = 300 mbar (1000/1300 mbar)	P2.6_V1	43mm, mold full, good surface, only few small bad islands, uniform	1.9	8	3
		P2.6_V2	42mm, mold full, uniform, the upper 2 cm bad surface	7.9		
		P2.6_V3	41mm, mold full, uniform, just few imperfections	2		34

It is interesting to observe that by far the casting experiments upon which the best results were obtained took place when the casting atmosphere was not very “clean”. Other fact, when the samples were not amorphous, one could observe on their surface some voids, as some crystals were embedded in the amorphous matrix. For selected samples Oxygen and Nitrogen (i.e. the air main constituents) content were analyzed, because these are susceptible to dissolve in the final product.

In the following are shown the variation of the amorphicity function of different casting atmosphere and Oxygen/Nitrogen level in the sample. Due to the reasons discussed previously, the coercivity was used as an amorphicity gauge. The level up to which the samples can be considered still glassy was set to 10 A/m.

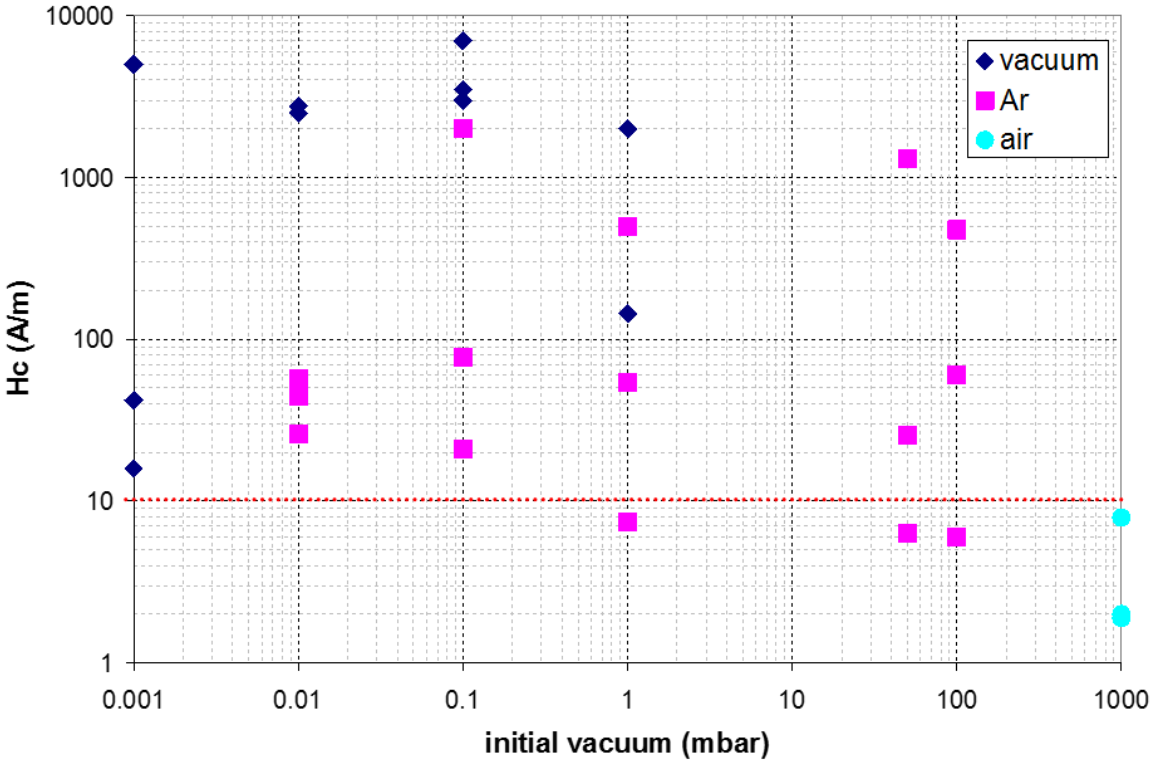

Fig. 4.9 Coercivity as a function of the atmosphere cleanliness (i.e. the initial pressure in the casting chamber).

Fig. 4.9 shows the coercivity as a function of the casting atmosphere purity (i.e. the initial pressure in the casting chamber). As already anticipated, **the best results were obtained upon casting in air**. Interestingly, the worst results were recorded upon vacuum casting. The castings in Ar show a large scatter; however, the best results in this category took place also when the chamber was not evacuated down to a high-vacuum level.

Fig. 4.10 presents in details for the selected samples the Oxygen (blue rhombs) and Nitrogen (magenta squares) levels as a function of the atmosphere cleanliness (i.e. the initial pressure in the casting chamber). It is interesting to remark that the initial vacuum prior filling with Ar has significant influence on Oxygen content. Moreover, the lowest values of the Nitrogen content was found for samples cast in air. And, both Oxygen and Nitrogen content have a descendent trend as the partial air pressure increases.

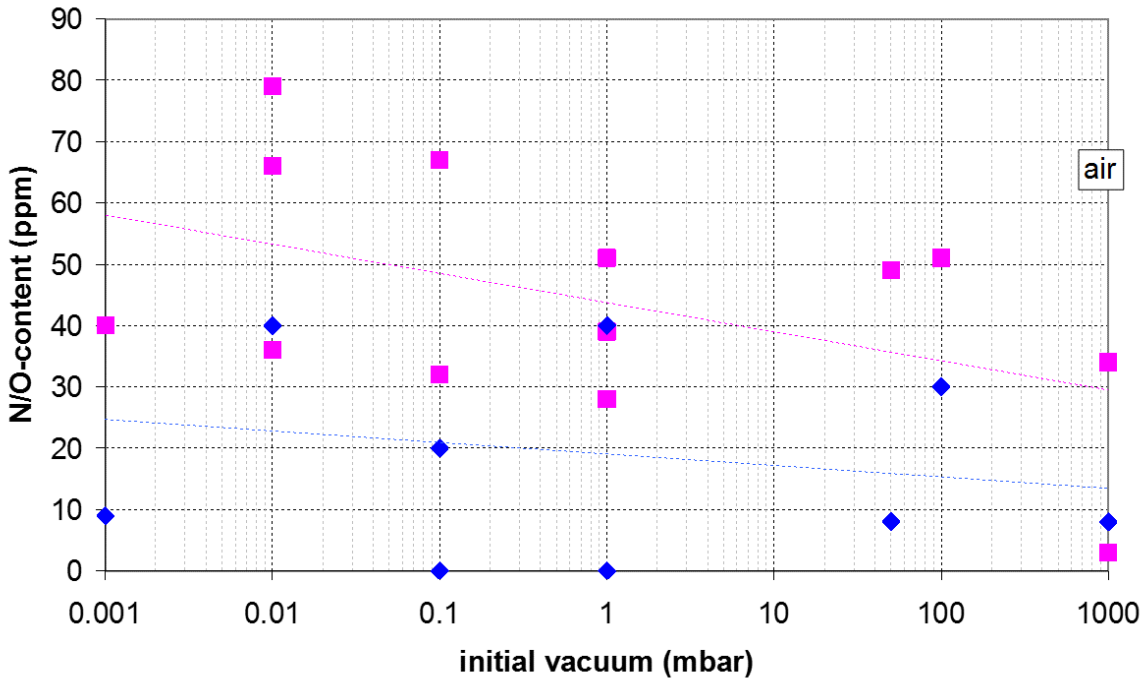

Fig. 4.10 Oxygen (blue rhombs) and Nitrogen (magenta squares) levels as a function of the atmosphere cleanliness (i.e. the initial pressure in the casting chamber).

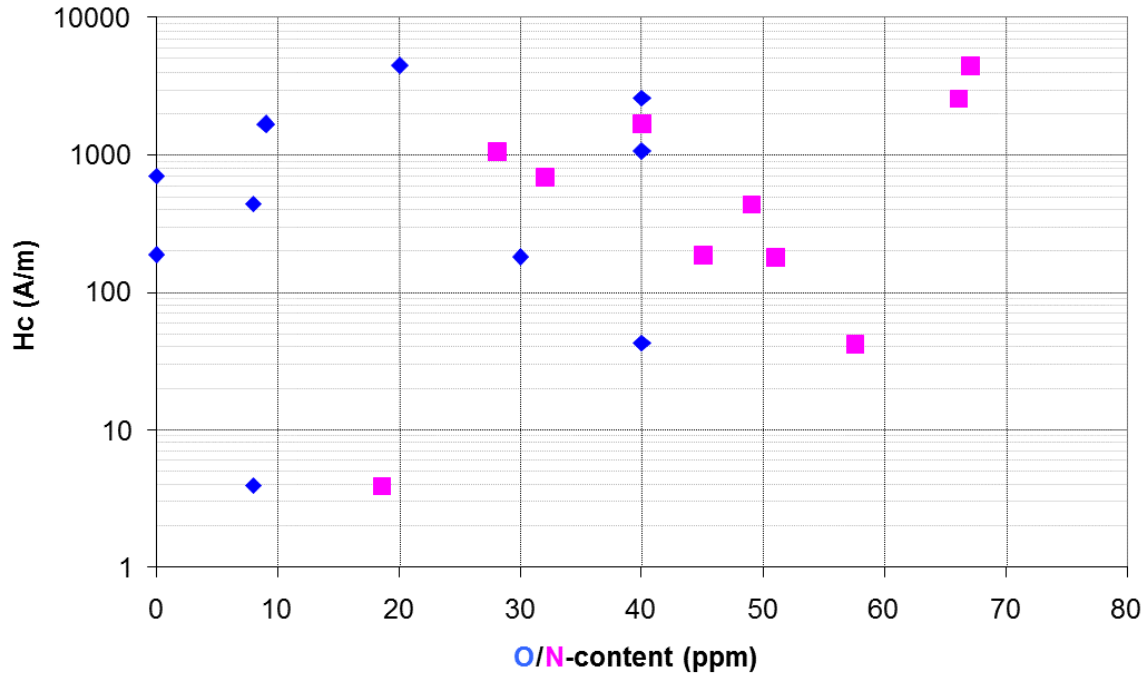

Fig. 4.11 The coercivity (and therefore the amorphicity) as a function of Oxygen (blue rhombs) and Nitrogen (magenta squares) content.

The next legitimate question is if there it is a traceable trend regarding the amorphicity and the Oxygen or Nitrogen content. The answer is shown in Fig. 4.11,

where the coercivity as a function of these two elements is illustrated. Surprisingly, there is **no evident trend**, so no clear conclusion can be drawn. However, one should recalls that here it is about the Oxygen and Nitrogen content in the cast sample and not in the master alloys used for casting. This is why, in order to restrict the factors which may affect the GFA, the master alloy chosen for these trials were produce starting from the pure elements.

Chapter 5
Crystallization behavior of $[(Fe_{0.5}Co_{0.5})_{0.75}B_{0.2}Si_{0.05}]_{96}Nb_4$ BMGs

The glassy state is retained at room temperature if the nucleation and growth is avoided. In simple words this requirement is traduced in the necessity to cool the melt as fast as possible. In the real life the maximum achievable cooling rates are limited. As a consequence, in order to obtain amorphous structure at experimentally accessible cooling rates, the crystalline network must be frustrated. Consequently the most successful compositions should be those with polymorphous crystallization of several different crystalline phases. Also, a good candidate may be an alloy which forms upon primary crystallization a complicated structure, which require diffusion over long distances. In both cases, the atoms present in the molten alloy would need a long time for rearrangements at the long range scale. When in the alloy **atoms that stabilize the crystalline equilibrium phases** are present, the time necessary for rearrangements is substantially shortened and, as consequence, **the crystals will form much earlier** that the kinetic freezing of the entire melt. Once the proper nuclei formed, they can further (i) grow in dimensions and numbers or (ii) be centers for further heterogeneous nucleation. Both cases are detrimental for the glass formation and such situation must be avoided.

In order to study the crystallization behavior, one needs to combine data obtained from different means. In the present case the change of the amorphous structure is analyzed from thermodynamic and structural point of view. Therefore, data collected upon DSC measurements, in isochronal and isothermal mode, as well as time-resolved X-ray diffraction using the synchrotron radiation, were critically assessed. In both cases several samples made from different master alloys were used. The experimental behavior is finally modelled, and in this way a complete image of what could take place was created.

5.1 Crystallization behavior, thermal studies

Upon thermal measurements, the characteristic temperatures which basically defines the glass forming ability (glass transition temperature T_g, crystallization

temperature T_x, melting (liquidus) temperature T_{liq}, extension of the supercooled liquid region ΔT_x, reduced glass transition temperature $T_{rg} = T_g / T_{liq}$ and gamma parameter $\gamma = T_x / (T_g+T_{liq})$) can be analyzed. Also, several other parameters can be measured and calculated as well:

- the crystallization enthalpy ΔH (directly related to the amount of crystallized amorphous matrix);
- activation energy for crystallization E_c (related to the stability of the amorphous structure against crystallization);
- incubation time τ (the time after which the crystallization starts when the amorphous sample is kept at a constant temperature in the supercooled liquid region);
- Avrami exponent n (characteristic for the crystallization type- indicates the nature of transformation);
- reaction constant k (dependent on the crystallization type and activation energy).

The techniques used in order to establish the above mentioned parameters are based on Kissinger approach or on the Johnson-Mehl-Avrami (JMA) plots. For Kissinger approach the high-temperature NETZSCH DSC 404 (heat flux mode DSC) was employed. There, the amorphous samples were heated from room temperature up to above complete crystallization, using different constant heating rates (i.e. isochronal mode). If one considers T the absolute temperature, R the gas constant and ϕ the heating rate, the Kissinger equation can be written as [Kis57]:

$$\ln\frac{\phi}{T^2} = -\frac{E}{RT} + const. \qquad (5.1)$$

By plotting the $-ln(\phi/T^2_P)$ as a function of $1000/T_P$, where T_P is the temperature of the exothermic event which indicates the crystallization (peak temperature), the activation crystallization energy E_c will be proportional with the slope of the curve. The errors are smaller when the curve contains more points, i.e. several isochronal experiments at different heating rates have to be performed. Table 5.1 summarizes the data measured for new glassy samples produced by using the master alloy **DD-pure**. The new samples show identical behavior. However, in order to distinguish between several

samples, in the following only the data measured for the sample BUH2240 are presented. Here should be mentioned that for this kind of experiment only **DD-pure** alloy was used, because the previous experience have shown that this alloy is the one which has the nominal composition closest to the designed one. Compared with the previous cast samples (see Table 4.5), the new samples show a ~ 12% larger SLR (i.e. with 4 K), resulting in a better thermal stability and therefore improved GFA.

Table 5.1 The main temperatures measured in the high-temperature DSC upon various constant heating rates. The peak temperatures and the heating rates were further used to calculate the activation energy for crystallization.

ϕ [K/min]	T_g [K]	T_x [K]	ΔT_x [K]	T_P [K]
5	805	837	32	848
10	812	844	32	855
15	820	853	33	859
20	827	860	33	861
30	829	865	36	866
40	832	869	37	872

Fig. 5.1 shows the Kissinger plot, calculated with the data presented in Table 5.1. As it is observed, a relatively good linear dependence of the measured data was obtained, indicating a good reproducibility. The activation energy of 536 kJ/mol is quite high, for example much higher than the characteristic values for Zr-based glasses (~ 250/300 kJ/mol [Sur11]). High values of activation energy for crystallization usually are characteristic to amorphous systems with a very high stability against crystallization. Literally it represents the necessary energy for one mole of the amorphous alloy to crystallize.

Further, for the Johnson-Mehl-Avrami approach, the PERKIN ELMER DSC 7 (power compensation DSC) was used. Here the samples were heated with the same constant heating rate (i.e. 20 K/min) up to a temperature above T_g, but still in the SLR, and hold there for a given time. After a while, the crystallization took place and several data could have been measured and calculated. The isotherms are presented in Fig. 5.2, for each curve the plateau temperature being mentioned.

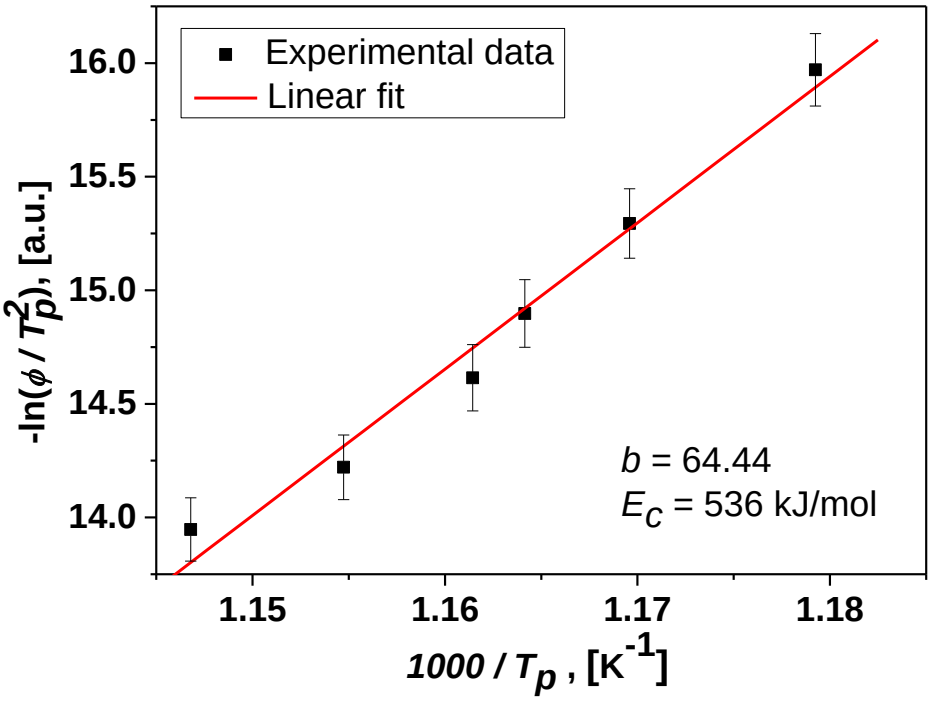

Fig. 5.1 Kissinger plot, from which the E_c was calculated. According to the formalism, $E_c = R \cdot b$ = 536 kJ/mol, where b is the slope of the curve, calculated by fitting the experimental data.

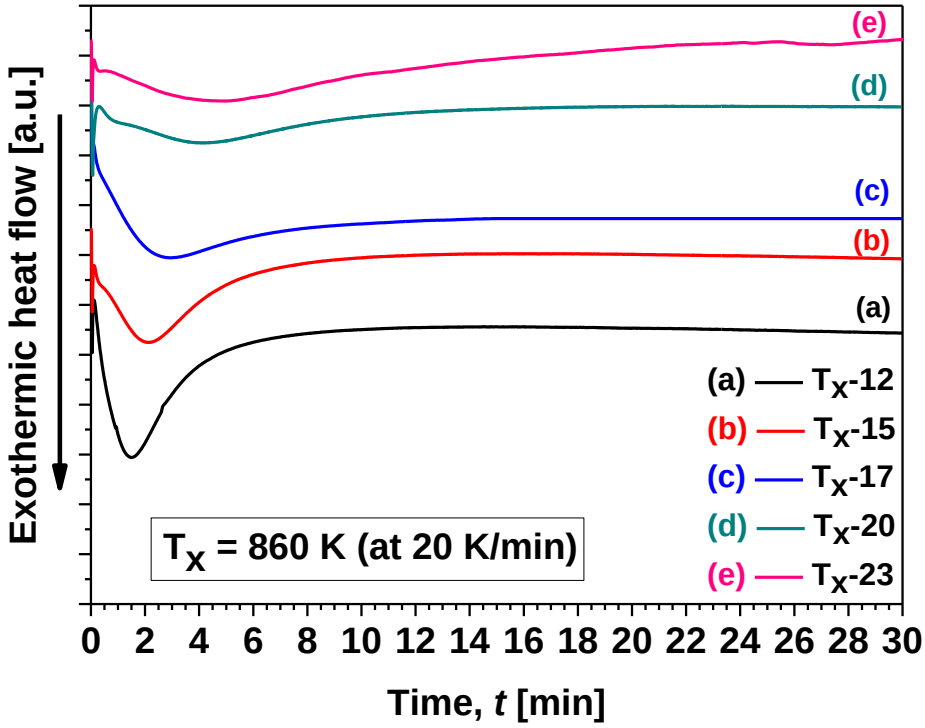

Fig. 5.2 The isothermal DSC curves. The heating up to the plateau temperatures was done at 20 K/min.

It is interesting to observe that basically the crystallization starts after a very short time, but until the final stage, i.e. fully crystallization, is necessary a relatively long time. As the plateau temperatures approach the crystallization temperature, the crystallization is faster and takes shorter time. According to the JMA equation [Avr39],

$$x = 1 - \exp\left\{-[k(t-\tau)]^n\right\} \tag{5.2}$$

in which x represents the crystallized fraction (time dependent), k is the reaction constant, n the Avrami exponent and τ the incubation time. The reaction constant is also temperature and activation energy dependent and is assumed to be described by Arrhenius equation:

$$k = k_0 \exp\left(-\frac{E_c}{RT}\right) \tag{5.3}$$

By plotting the crystallized fraction as a function of time (x is proportional with the area closed by the crystallization peak), we obtain typical sigmoidal curves (the temporal evolution of the crystallization), as shown in Fig. 5.3.

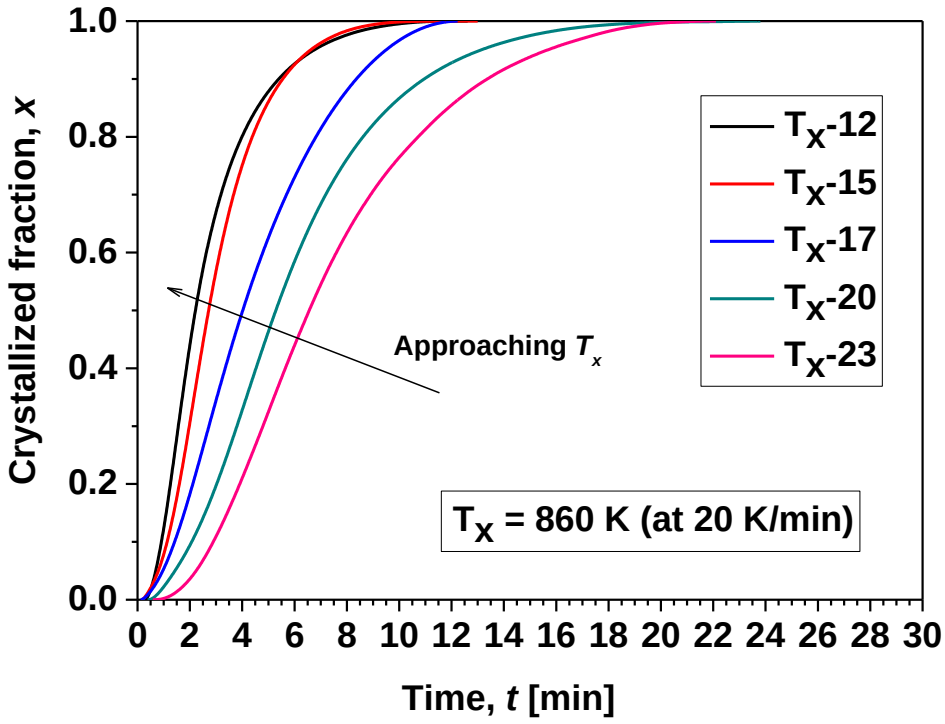

Fig. 5.3 Temporal evolution of the crystallized fraction. The isothermal temperatures and the corresponding curves are indicated. At higher temperatures the crystalline fraction increases faster.

The sigmoidal-type curve means that the crystalline volume fraction evolution with time at the initial crystallization stage is slow, then increases rapidly and finally slow down again or reaches saturation. During the initial part of the transformation, the nuclei are formed at different incubation times and this process continues with evolution of time depending on the nucleation rate during the overall transformation process. The saturation could be understood in terms of site saturation i.e. no sites are available for further nucleation. This is because the matrix continuously changes its composition too as the crystalline precipitates are formed. The shape of the sigmoidal curve at different temperatures is also different. The curve for the temperature near to glass transition temperature shows a relatively slower rate of nucleation and growth than the curve for the temperature closer to crystallization temperature. This is only due to the higher viscosity at lower temperature which leads to a slower diffusion of atoms.

In Fig. 5.3 one can see clearer that the crystallization starts immediately when the temperature rises above glass transition, but the complete transformation of the amorphous matrix requires a relatively long time. These curves are used in order to determine the incubation time τ, defined as the time interval between the sample reaching the isothermal temperature and the initiation of the transformation. Experimentally, τ is considered the moment when the crystallization fraction starts to increase linearly in time, i.e. when the *x* vs. τ curves become linear. In our case, this moment was considered when the crystallized volume fraction reached 10%. After applying the logarithm to eq. (5.2), one can obtain:

$$\ln\left(\ln\frac{1}{1-x}\right) = n\ln k + n\ln(t-\tau) \tag{5.4}$$

The plots described by the eq. (5.4) are named JMA plots and from here the *n* and *k* constants can be evaluated. Fig. 5.4 shows the plots, while the data are summarized in Table 5.2. The JMA plots are quite linear and almost parallel, in good agreement with nucleation theory. The present studied glassy samples are very resistant against crystallization. They need high temperature and high energy to crystallize, but once the critical level attained, the crystallization proceeds immediately. This explains the high value of activation energy as well as the very small values found for incubation time (see Table 5.2).

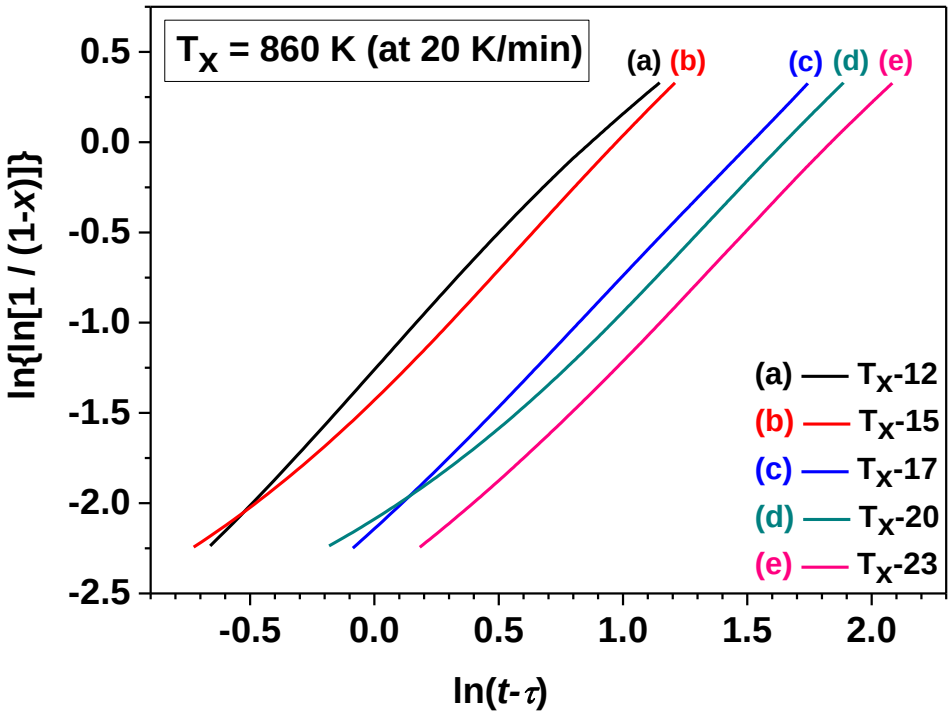

Fig. 5.4 The Johnson-Mehl-Avrami plots for different annealing temperatures. The plots were calculated for $0.10 < x < 0.75$.

Table 5.2 Incubation time τ, Avrami exponent n and reaction constant k as a function of annealing temperature.

Kinetic parameters	Plateau temperature [K]				
	T_x - 12 = 848	T_x - 15 = 845	T_x - 17 = 843	T_x – 20 = 840	T_x – 23 = 837
τ (min)	0.4	0.65	0.5	1.25	1.7
n	1.37	1.48	1.44	1.44	1.43
k	2.41	2.64	4.54	5.18	6.33

The Avrami exponent, which on average takes the value of 1.43, could indicate some **pre-existing nuclei**. In literature it is considered that an Avrami exponent of 1.5 = 3/2 is a particular case and it is characteristic for a 3D growth of spherical crystallites, athermal and diffusion controlled (athermal = crystals starts to grow at the same time = crystals of equal size). This is characteristic for **primary crystallization** way of transformation, in perfectly agreement with our experimental data. The experimental measured values 1.43 of the Avrami exponent, i.e. a bit lower than the particular case of 3/2, may be due by the fact that the pre-existing nuclei are still very small or even not clearly formed. However, it clearly indicates that in this kind of bulk glasses a short range order (SRO) which influences the further crystallization may exists. Most

probably, as suggested earlier, the atoms are pre-arranged in trigonal prisms, which further will develop in the complex fcc $Fe_{23}B_6$-type structure. However, a strictly physical interpretation of the Avrami constants, *k* and *n*, is difficult and prone to misjudgment. Originally, *n* was held to have an integer value between 1 and 4, which reflected the nature of the transformation in question. For example, the value of $n = 4$ can be said to have contributions from three dimensions of growth and $n = 1$ representing a constant nucleation rate. Alternative derivations exist where *n* has a different value. An interesting situation occurs when nucleation happens on specific sites (such as grain boundaries or impurities) which rapidly saturate soon after the transformation begins. Initially, nucleation may be random and growth unhindered leading to high values for *n* (3 or 4). Once the nucleation sites are consumed the formation of new particles will cease. Furthermore, if the distribution of nucleation sites is non-random then the growth may be restricted to 1 or 2-dimensions. Site saturation may lead to *n* values of 1, 2 or 3 for surface, edge and point sites, respectively.

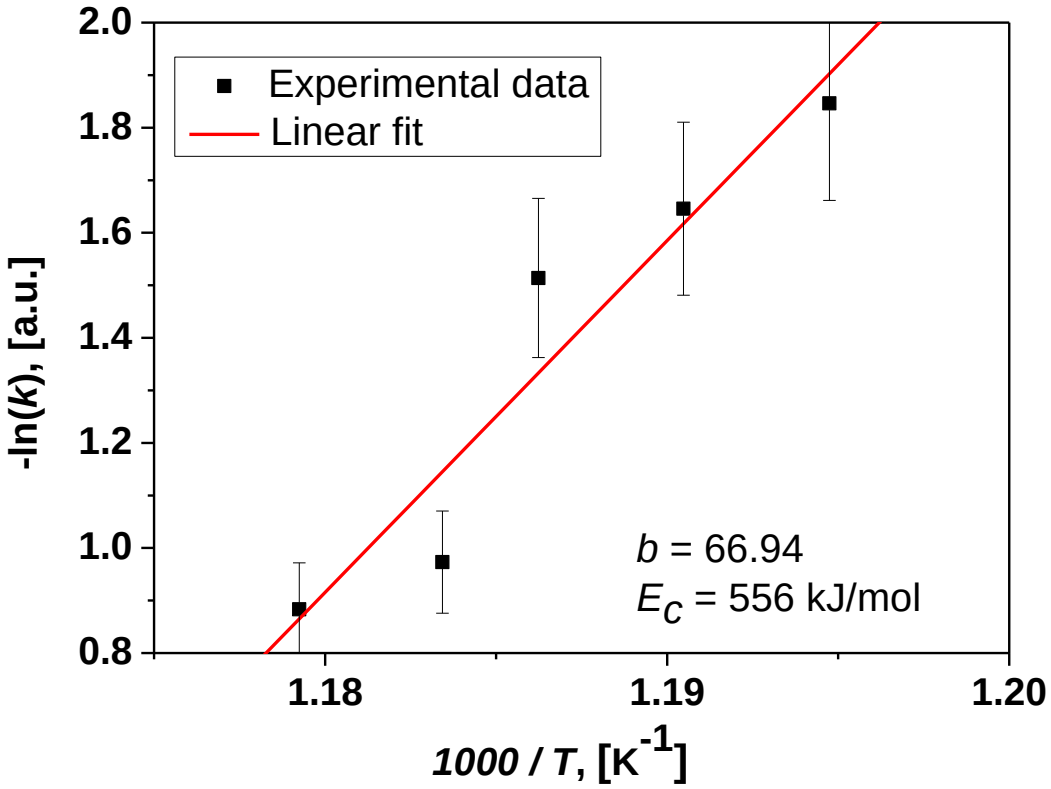

Fig. 5.5 Plot *–ln(k)* as a function of *1000/T*, from which the activation energy was calculated.

Coming back to the equation (5.3) and by applying the logarithm, one obtains:

$$\ln k = \ln k_0 - \frac{E_c}{RT} \tag{5.5}$$

therefore by plotting the *–ln(k)* as a function of *1000/T*, where *T* is considered to be the corresponding plateau temperature, a new almost linear dependence with the slope proportional with the activation energy for crystallization is obtained (Fig. 5.5). Using this method, the activation energy for crystallization was calculated to be 556 kJ/mol, in good agreement with the value found by Kissinger approach (536 kJ/mol). The bigger scatter of the data points is due in principal by the uncertainty in measurement of the short incubation times. However, a deviation of ± 20 kJ/mol is within the measurements errors.

5.2 Crystallization behavior, time-resolved XRD studies

Several amorphous samples were investigated by XRD using high intensity high-energy monochromatic synchrotron radiation. For the structural evolution is important to study samples made from various master alloys because they may behave different as the compositions are slightly different. In the following, the data characteristic for 3 different amorphous samples will be discussed in very last detail. The mentioned samples are BUH2240, cast using the master alloy **DD-pure**, BUH2177, cast using the master alloy **DD-bin2** and BUH2121, cast using the master alloy **ZW-bin**. In this way, the most important master alloys are covered.

Fig. 5.6 shows for comparison the DSC traces measured at 20 K/min for all three mentioned samples. This picture recalls the behavior of each glassy sample and gives the overall temperatures where the main events take place. Therefore, it will be used as a starting point for further detailed analyses. As it can be seen, all three samples crystallize relatively similar. However, the DSC thermograms show some differences in the main temperatures, as well as in the crystallization path. For example, the **DD-pure** sample (BUH2240, curve (a) in Fig. 5.6) shows only one single crystallization event, followed at a large distance by other small exothermic events. The second exothermic event is more pronounced and takes place at a lower temperature in the case of **DD-bin2** sample (BUH2177 or curve (b)), while for **ZW-bin** (BUH2121, curve

(c)) it is shifted toward higher temperatures, it is very weak and followed by a much sharper exothermic event.

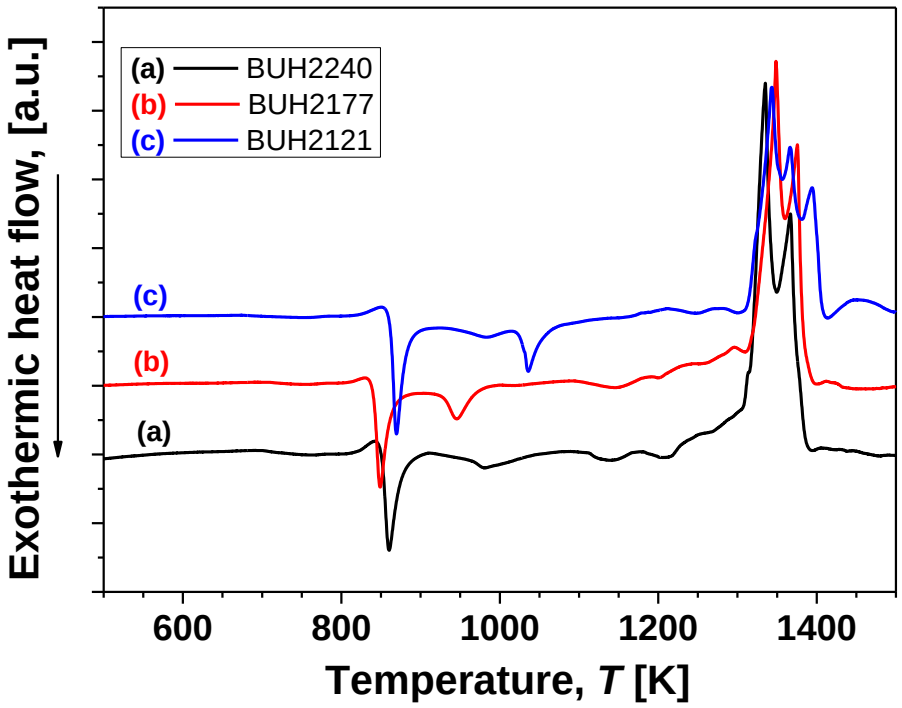

Fig. 5.6 DSC traces of the three investigated BMGs. The heating was performed with a constant heating rate of 20 K/min.

Figs. 5.7, 5.8 and 5.9 show the general evolution in time as the temperature increases of the amorphous structure for all three samples (BUH2240 **DD-pure**, BUH2177 **DD-bin2** and BUH2121 **ZW-bin**, respectively). The XRD in transmission configuration clearly proves the amorphous nature of all samples- only broad maxima are visible in the patterns (at room temperature) and no sharp Bragg peaks. The first and second broad maxima are in detail presented in the inset. The wave vector scale is unreadable (due by the used software to plot all curves together), but there the emphasis is on the way of crystallization (i.e. qualitatively). Later on detailed singular patterns will be presented. From the start of the crystallization moment up to the maximum reached temperature only one kind of crystalline phase formed. The DSC traces (in detail presented in Fig. 5.6) have shown that there is basically only one main crystallization peak, which is followed at a certain temperature by other exothermic transformation(s), which can be attributed to the crystallization of the rests of the amorphous matrix (very possible when the first crystallization is of the type primary crystallization). Judging now from the diffracted patterns, the phase(s) which appear upon first crystallization event do not modify their structure- one can see that the

crystalline peaks do not transform in others, just increase in intensity (= presence of an increased volume fraction). This already points toward the possibility to have a primary crystallization of a metastable phase with big unit cell.

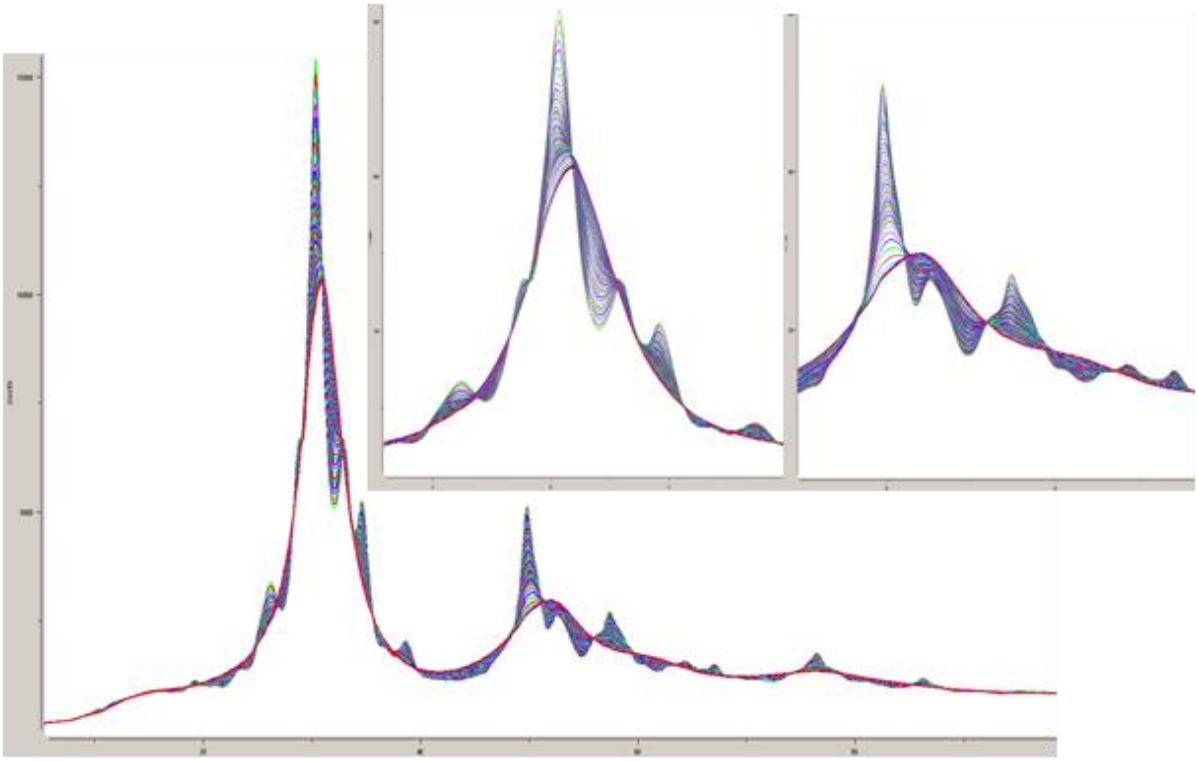

Fig. 5.7 The structural evolution of BUH2240 BMG sample (alloy **DD-pure**).

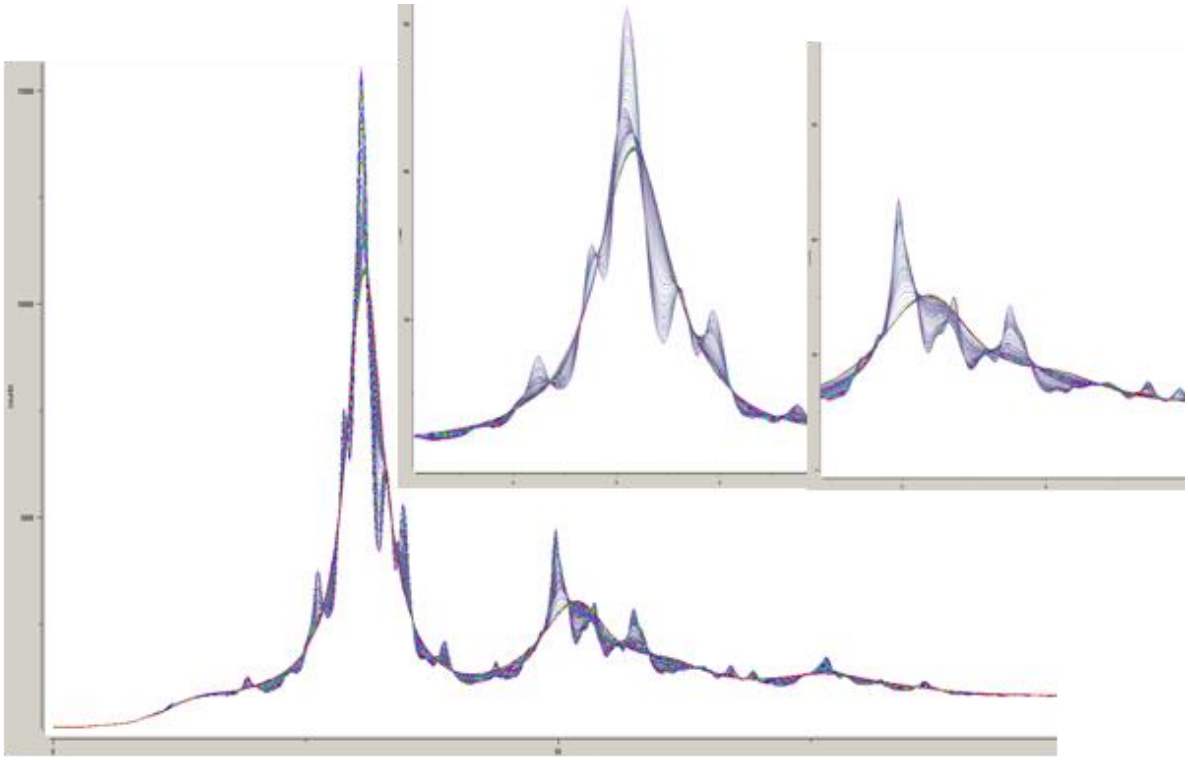

Fig. 5.8 The structural evolution of BUH2177 BMG sample (alloy **DD-bin2**).

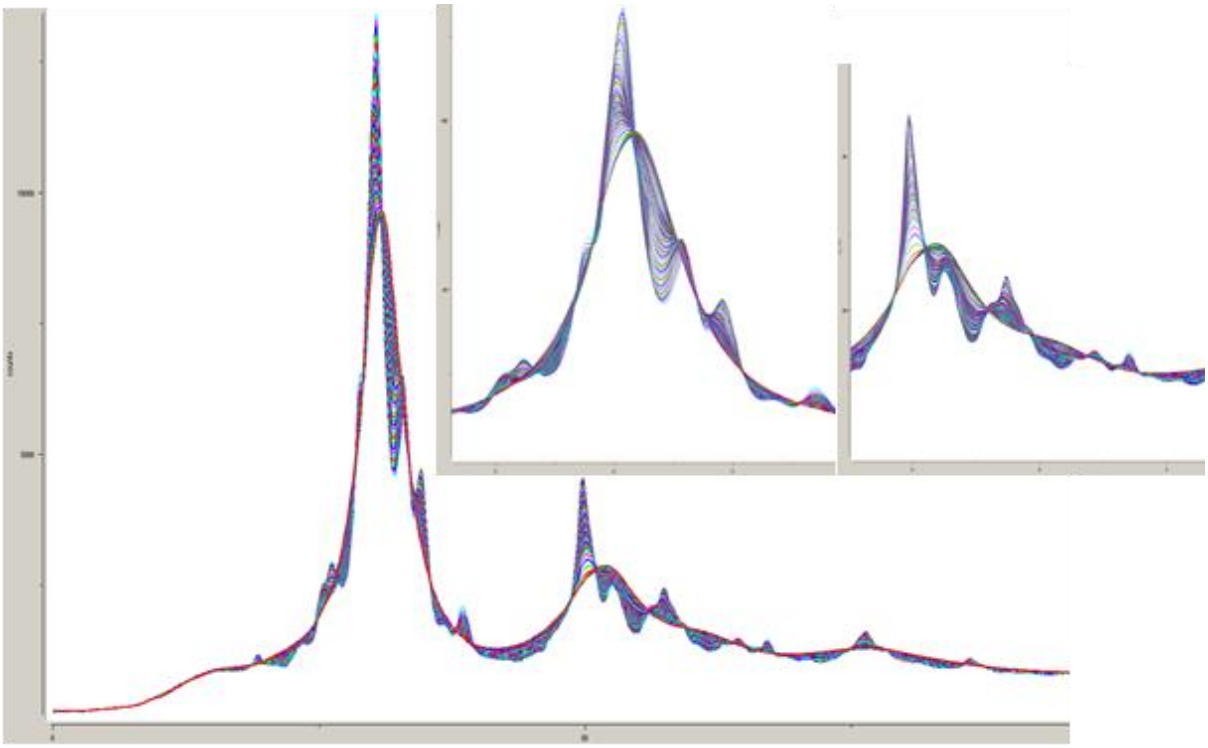

Fig. 5.9 The structural evolution of BUH2121 BMG sample (alloy **ZW-bin**).

The detailed XRD patterns recorded for various temperatures are presented in Figs. 5.10, 5.11 and 5.12. The patterns are extracted from those presented in Figs. 5.7, 5.8 and 5.9, respectively, shifted with the same amount on the y scale (which is the diffracted intensity scale) and the respective temperatures are marked in clear. The maximum achieved temperature for time-resolved XRD, i.e. 1050 K, covers all main changes observed in Fig. 5.6. The crystalline phases are marked in the figures with vertical arrows.

There one can clearly see that the only crystalline phase which can be surely identified is the “big cube” fcc $Fe_{23}B_6$-type phase. The presence of small volume fraction of other crystals cannot be surely ruled-out, but eventually their quantity is small and therefore the corresponding Bragg peaks are weak. However, the exothermic events observed in the DSC, above the main crystallization peak, are mostly due by the transformation of the residual amorphous matrix into $Fe_{23}B_6$. The transformation of other formed crystals (for example Fe_2B) in $Fe_{23}B_6$ is less probable, because (i) $Fe_{23}B_6$ is a metastable phase and Fe_2B is the equilibrium one and (ii) an allotropic transformation of this kind should provoke an endothermic event and not an exothermic one. Further, in order to analyze if samples made from different master alloys behave different, there are plotted together diffraction patters stemming from all three samples at selected temperatures (Figs. 5.13, 5.14 and 5.15).

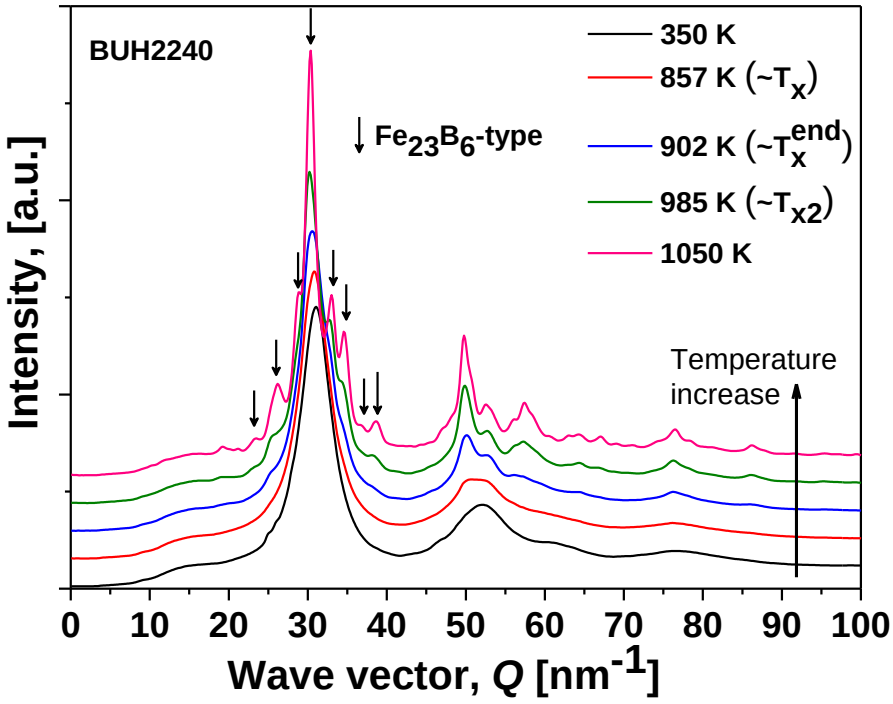

Fig. 5.10 BUH2240 DD-pure glassy sample: diffraction patterns recorded at several different temperatures. The temperatures are immediately above the exothermic events put in evidence by the DSC experiments (Fig. 5.6).

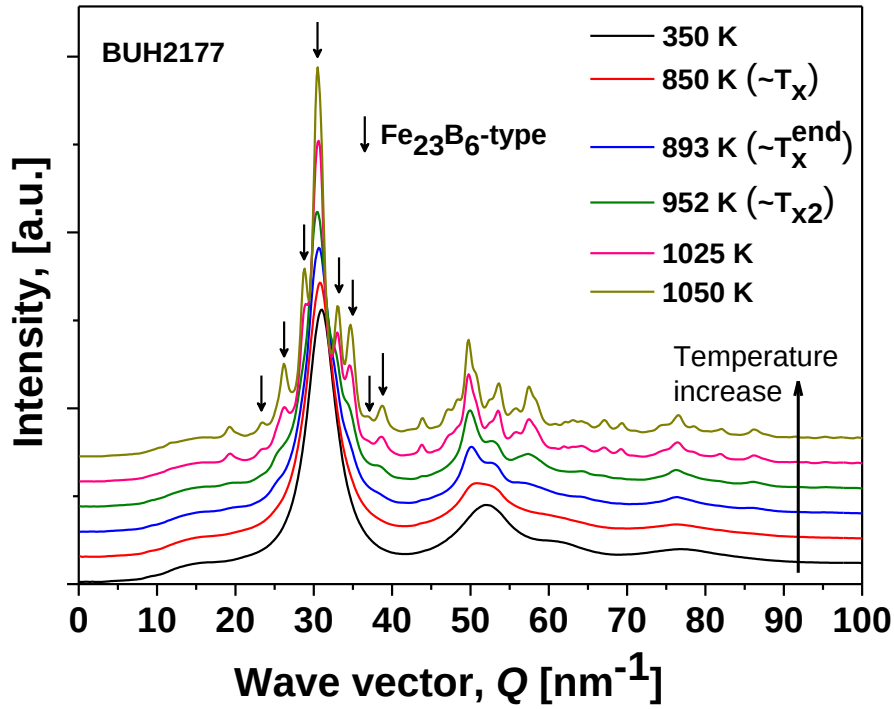

Fig. 5.11 BUH2177 DD-bin2 glassy sample: diffraction patterns recorded at several different temperatures. The temperatures are immediately above the exothermic events put in evidence by the DSC experiments (Fig. 5.6).

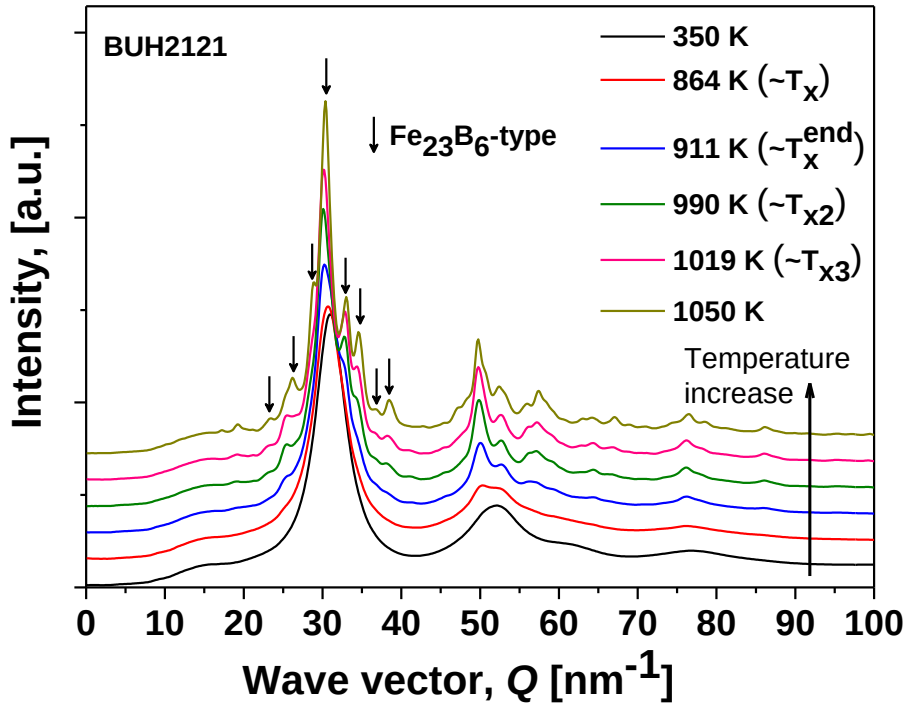

Fig. 5.12 BUH2121 ZW-bin glassy sample: diffraction patterns recorded at several different temperatures. The temperatures are immediately above the exothermic events put in evidence by the DSC experiments (Fig. 5.6).

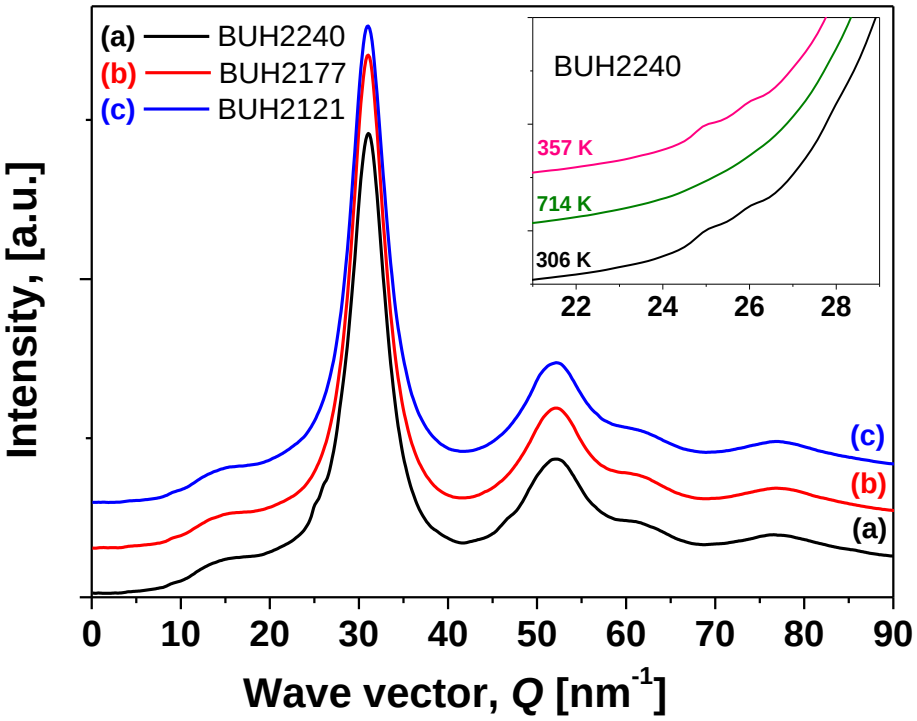

Fig. 5.13 Diffraction patterns at room temperature. The inset shows in detail the evolution of the "humps" when the sample is subjected to a thermal cycle room temperature-high temperature-room temperature, with the highest attained temperature lower than the glass transition (i.e. T_{ann} = 714 K), but close to it (i.e.T_g = 827 K).

Fig. 5.13 presents for comparison the diffraction patterns of all three samples at room temperature (i.e. around 300 K). The samples are glassy but their short-range order might be different. In detail, one can see that the sample BUH2240 made from DD-pure master alloy (and only this sample) shows some “humps” before and after the main halo. Such kinds of things are really difficult to be put in evidence and easily can be mistaken with measurement artifacts. In the actual case a very careful analysis of the XRD data was made, so they are real and due to the position in the reciprocal space one can suppose that there a kind of ordering may be present- or even nuclei. This would not be a surprise and somehow could be common also for other kind of Fe-based BMGs [Sto09, Sto10b]. Interesting is that by annealing these entities disappear, but they form again when the sample is cooled down. The temperature at which they disappeared was 714 K, which, for this sample, is exactly at the beginning of the relaxation interval prior glass transition (see Fig. 5.6). More, analyzing in detail Fig. 5.13, we can see that only this sample shows such clear relaxation interval. The explanation for this behavior is the following, supposing that there a kind of nanocrystalls or nuclei are present. Once the temperature increases the interatomic distances start to increase. There it is a moment when the thermal agitation becomes high enough and the ordering is destroyed. As a consequence, the “humps” disappear. If the sample is cooled down, the ordering appears again. If the annealing temperature is high enough, close to T_g (at the end of relaxation), or if the annealing time is long enough, this order may be completely destroyed and by cooling it will not form anymore. The mechanism through which such transformations could happen is eventually the annihilation of the free volume. In any case, if the free volume is released, a small shift of the main halo should be observed when the samples is cooled down to room temperature [Yav05]. This is given by the fact that by releasing the free volume, the interatomic distances become smaller, so the main halo shifts toward higher Q values.

Fig. 5.14 shows the XRD patterns, for all three samples, recorded at 714 K, a temperature below the glass transition but very close to. In fact, by analyzing the thermograms presented in Fig. 5.6 one can remark that at ~ 700 K the relaxation starts (i.e. the thermograms show a slight exothermic behavior prior glass transition). Therefore, if the samples are essentially different, at 714 K their XRD pattern should be different as well, which, as seen in Fig. 5.14, is not the case.

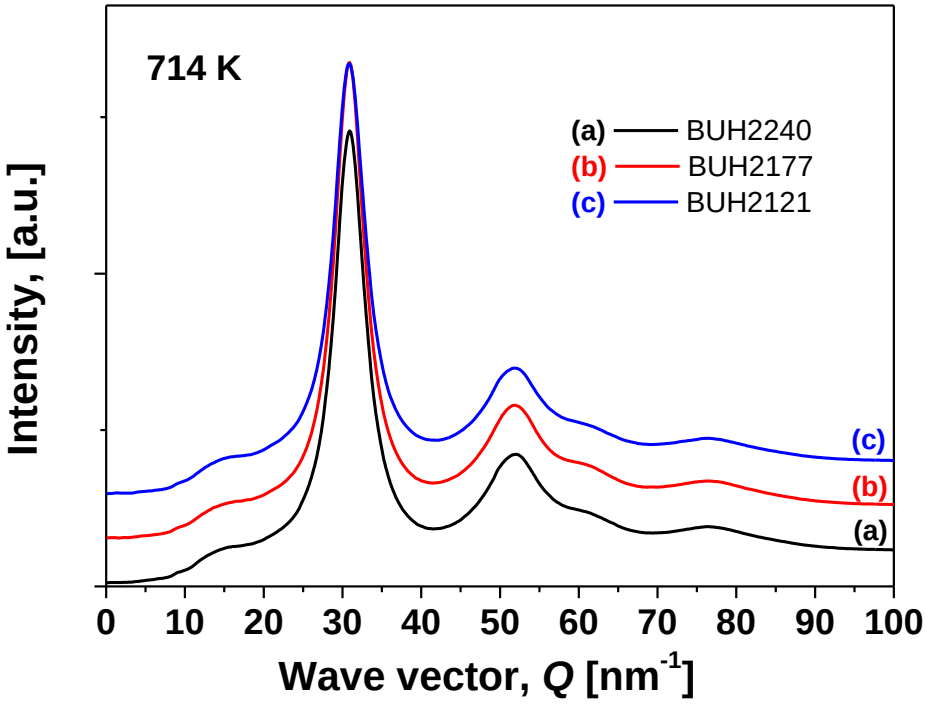

Fig. 5.14 Diffraction patterns for the three samples at 714 K (during relaxation prior glass transition). One can see that they are still fully amorphous.

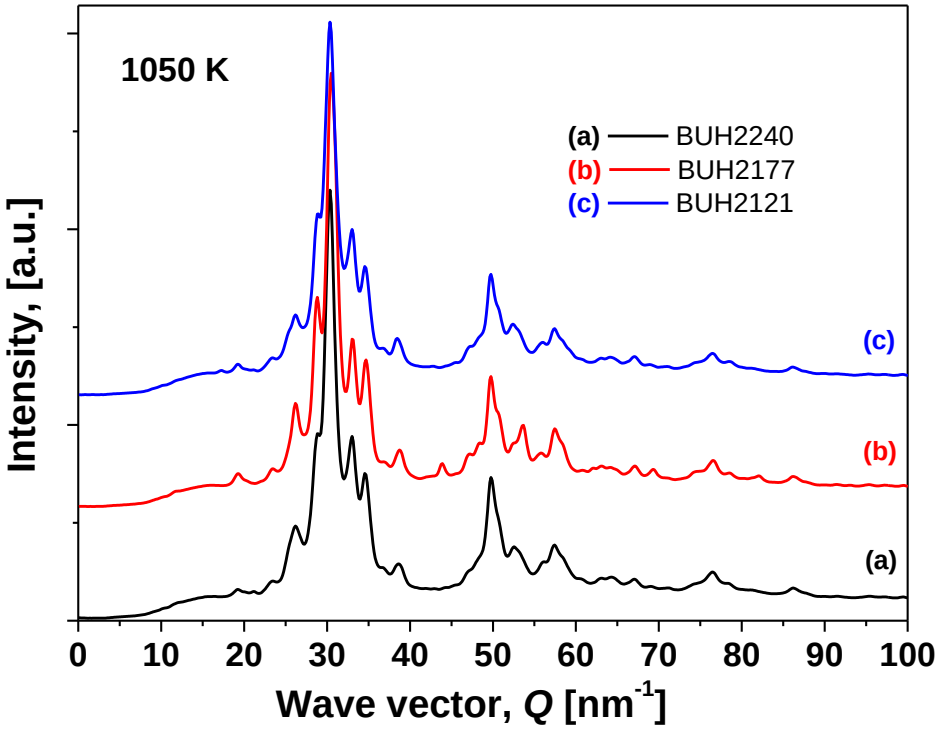

Fig. 5.15 Diffraction patterns for all three samples at 1050 K. They are fully crystallized and almost similar. The main crystallized phase which is present is of the $Fe_{23}B_6$-type.

Fig. 5.15 presents the XRD patterns recorded at 1050 K, the maximum temperature achieved during in-situ heating. From there one can understand that when fully crystallized, all three samples are similar. However, there small differences may be observed. For example the sample BUH2177 (DD-bin2 master alloy) might display some “extra features” when compared with the other two samples. The new extra peaks are anyway too small (both qualitatively and qualitatively) in order to precisely identify the additional crystalline phases. The eventual possibilities basically restrain to t-Fe_2B, t-Fe_3B, α-Fe and/or γ-Fe. They may form by crystallization of small volume fractions of the amorphous matrix after the $Fe_{23}B_6$ is formed. The composition of the alloy does not correspond to the stoichiometry of the $Fe_{23}B_6$ phase, therefore what is left should crystallize in the equilibrium phases.

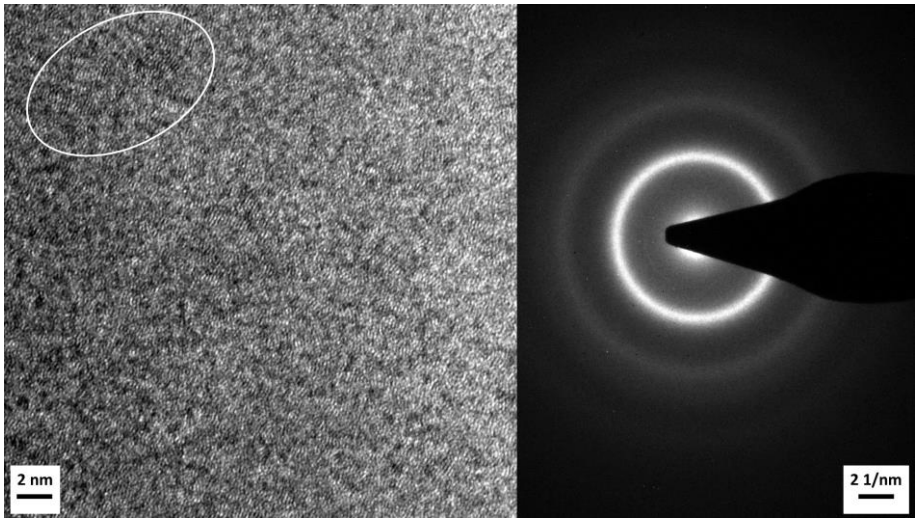

Fig. 5.16 HR-TEM picture and the corresponding SAED patterns taken from the sample BUH2121. Short-range ordering might be present, as such in the area marked with the white ellipse.

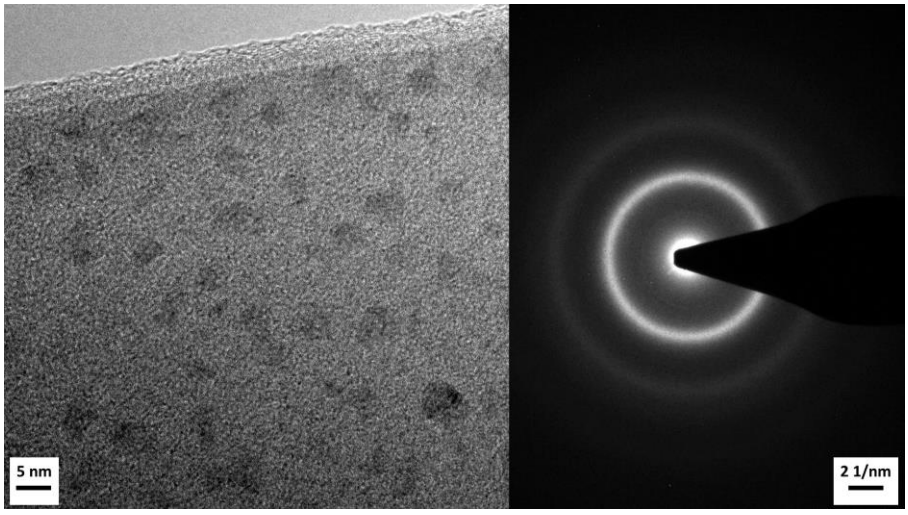

Fig. 5.17 HR-TEM picture and the corresponding SAED patterns taken from the sample BUH2240 (margin of the TEM sample). Here the nanocrystalls are more visible. However, the SAED patters does not evidence them.

The coercitivities of the as-cast BMGs were: BUH2240 = 6 A/m, BUH2177 = 8.5 A/m and BUH2121 = 2.7 A/m. It is interesting that the BUH2240 sample, which shows those nuclei at room temperature, has also very small coercivity. However, the other samples may also have some nuclei, but if they are not very uniform distributed may not appear in the XRD. If the nuclei/nanocrystalls are small enough, i.e. below the magnetic exchange length, they cannot be put in evidence as well upon coercivity measurements. Moreover, if the sample is completely nanocrystalline, as for example in case of FINEMET® alloy [Yos88], the magnetocrystalline anisotropy is averaged out and the resultant coercivity is insignificantly small. (However, such crystals, even at the nanoscale, should be visible in the transmission XRD, which is not the case here).

Further, to confirm the previous suppositions, Figs. 5.16 and 5.17 show the high resolution TEM (HR-TEM) bright-field micrographs and their corresponding selected area diffraction patterns (SAED) taken for the sample BUH2121 and BUH2240. The BUH2121 sample is fully amorphous, but if one is really keen to see something, some ordering might be observed in the area marked with an ellipse. However, the SAED pattern is characteristic to an amorphous sample. The sample BUH2240, which has a slightly larger coercivity (i.e. 6 A/m) may indeed have some nanocrystalls, as seen in Fig. 5.17. Nevertheless, their dimensions are 5 to 8 nm, far below the magnetic exchange length of Fe [Yos88]. They should not produce any magnetic domain pinning and therefore not provoke an increase of the coercivity. The corresponding SAED pattern does not show any crystalline ring, which might indicate that there are only artefacts. Moreover, these entities were observed only at the margins of the TEM sample and the possibility that they appeared upon sample TEM sample preparation cannot be completely ruled out.

Concluding, the three samples made from three different master alloys are amorphous at RT, they have similar crystallization behavior, (with minimal differences) and only (or mainly) $Fe_{23}B_6$ type metastable phase forms there (or has the highest volume fraction). The existence of a small volume fraction of other phases cannot be ruled-out completely, but they are not unambiguously identified. However, amorphous samples show similar behavior and similar properties regardless the master alloy used for casting. The impurities which may affect the GFA are the ones which may trigger the formation of the observed nanocrystalls, i.e. which stabilize structures as t-Fe_2B, t-Fe_3B, α-Fe and γ-Fe.

Chapter 6

A new model alloy: $Fe_{74}Mo_4P_{10}C_{7.5}B_{2.5}Si_2$

6.1 Particularities and the investigated master alloys

Combining the achievements presented in literature, together with our own expertise, a new good glass-former alloy was chosen: $Fe_{74}Mo_4P_{10}C_{7.5}B_{2.5}Si_2$. This composition was presented by S.J. Pang at the ISMANAM 2007 Conference [Liu09] as being a composition which allows the preparation of BMGs up to 5 mm diameter and a length of 5 cm. The preliminary trials at IFW Dresden on this composition were successful and we found that the GFA is indeed very good, a **7 cm long rod** (therefore **longer than predicted** in scientific literature!) with a **diameter of 4 mm** can be reached upon copper mold injection casting. Further experiments, after compositional optimization, clearly shown that fully amorphous 5 mm diameter rod with length up to 5 cm can be produced. It is interesting to point out that, if for the $[(Fe_{0.5}Co_{0.5})_{0.75}B_{0.2}Si_{0.05}]_{96}Nb_4$ BMG-forming alloy the cleanness/purity of the master alloy plays a decisive role, the $Fe_{74}Mo_4P_{10}C_{7.5}B_{2.5}Si_2$ is not so sensitive. More, as it will be shown further, it requires small quantities of foreign elements to enhance its GFA!

If in the case of $[(Fe_{0.5}Co_{0.5})_{0.75}B_{0.2}Si_{0.05}]_{96}Nb_4$ the master alloy preparation does not put serious problems, in the case of $Fe_{74}Mo_4P_{10}C_{7.5}B_{2.5}Si_2$ the things are not so simple. The master alloy contains P and C, the first being toxic and difficult to work with and the second does not dissolve very easy in Fe. Therefore, several routes were tried, implying the use of different FeP pre-alloys and FeC pre-alloys. Several master alloys were prepared using laboratory pure and industrial ingredients and at different laboratories. The details are given in the following. The coding takes in account the name of the labs (i.e. IFW or OCAS), as well as their places (Dresden, Germany and Zwijnaarde, Belgium, respectively) and the used pre-alloys or pure elements.

In order to find out the influence of the constituents, **11 master alloys** were prepared using different ingredients: pure Fe lumps, pure Mo lumps, pure FeP pre-alloy created at IFW upon powder metallurgical routes (mechanically alloyed Fe powder with red P powder for 5 hours in a shaking mill, composition varying from eutectic FeP to Fe_2P, then compacted and induction-melted, the final composition assessed upon chemical analyses), pure FeC melted in IFW using Fe lumps and

graphite particles, Si single crystal, graphite particles, B crystalline, industrial FeP (OCAS or IFW), industrial FeB (OCAS), pure FeB (IFW), industrial FeSi (OCAS), industrial FeMo (OCAS). In all cases the master alloys were prepared by induction melting, in quantities which vary from 50 grams to 300 grams. After a carefully checking (optical and by comparing the input and the output mass) it was observed that **in all cases the master alloys were homogeneously** and there is **no influence on GFA related to the as-prepared quantities**. Also, there were no differences between alloys prepared with Fe and graphite lumps and the alloys prepared with FeC previously melt at IFW (which, as mentioned, was prepared as well from Fe and graphite lumps). This is very important to know, because even if the melting was in induction, the devices used for that are different: the 50 grams batches were produced with the help of laboratory equipment, while quantities > 200 grams were melt with the help of a semi-industrial device. Moreover, the FeC IFW pre-alloy is further regarded as “pure elements”. In the following is given the purity of the used ingredients and Table 6.1 shows the composition of the industrial pre-alloys from OCAS.

Fe: 99.99 % (lumps, electrolytic)
Fe:99.+% (powder, –200 mesh); used for mechanical alloying
P: 98.9 % (red, amorphous powder, –100 mesh); used for mechanical alloying
Mo: 99.9 % (lumps, electrolytic)
C: 99.99 % (particles)
B: 99 % (crystalline)
Si: 99.9999 % (single crystal)

Table 6.1 The composition of the used pre-alloys from OCAS, in wt.%. The empty cells indicate that the content of the searched elements were under the detection limit. The Fe content was not directly analyzed, it is obtained by balancing to 100.

	B	C	Al	Si	P	S	Cr	Mn	Cu	Mo	Fe
FeB	19.9	0.8	0.5	0.5							78.3
FeSi			1.24	75	0.02	0.06					23.68
FeP				0.85	25.7	0.004	0.26	3.52			69.66
FeMo		0.02		1.48	0.04	0.08			0.42	69.16	28.8

The nominal composition $Fe_{74}Mo_4P_{10}C_{7.5}B_{2.5}Si_2$ is given as usual in at.%. Transformed in wt. % it is:

82.66 Fe 7.68 Mo 6.20 P 1.80 C 0.54 B 1.12 Si

The 11 master alloys with this target composition were named simply from P1 to P10 and melted in induction. The preparation details are given in the following.

- **P1**- all pure elements, i.e. melting together in induction FeP obtained at IFW upon melting the mechanically alloyed Fe & P powders, FeC pre-alloy (also made in Dresden from pure electrolytic Fe lumps and graphite particles), pure Mo, crystalline B and crystalline Si.

- **P2**- three binary industrial ferroalloys FeP, FeB, FeSi from OCAS, pure Mo, graphite particles.

- **P3**- all binary industrial ferroalloys FeP, FeB, FeMo, FeSi from OCAS, graphite particles.

- **P4**- ordered outside IFW or OCAS (independent industrial supplier), no details available about casting procedure or ingredients. It was supplied as gas-atomized powder, which, despite the good GFA of this alloy, was not fully amorphous.

- **P5**- mechanically alloyed FeP at IFW, graphite particles, rest all pure elements.

- **Real-P2**- pure elements (including here FeC from IFW and mechanically alloyed FeP from IFW), but following the *as-analyzed* P2 composition, not the *nominal* composition.

- **P6**- industrial FeP from IFW, pure FeB from IFW, pure Mo, Si, C and Fe. Big ingot, not extracted from melting crucible

- **P7**- industrial FeP from IFW, pure FeB from IFW, pure Mo, Si, C and Fe. After melting the master alloys was cast as bar ϕ14 mm (so similar to P6 but extracted from melting crucible).

- **P8**- industrial FeP and FeB from OCAS, pure Mo, FeC IFW pre-alloy, crystalline Si.

- **P9**- industrial FeP from OCAS, FeC IFW pre-alloy, pure Fe and Mo, crystalline B, crystalline Si.

- **P10**- industrial FeB from OCAS, FeC IFW pre-alloy, FeP mechanically alloyed at IFW, pure Fe, pure Mo, Si-crystal.

The first master alloy which has shown good GFA was the **P2**. Therefore, the *real* chemical composition was analyzed and, using *only pure elements*, this *actual* composition was recreated. In this way the master alloy named **Real-P2** was designed. From the entire list of the master alloys, the best GFA was shown by **P2**, **P8** and **P9**. Here should be underlined that by **the best GFA** one refers to the possibility to cast BMGs as rods with **minimum 4 mm diameter** and a **length of 7 cm**. Otherwise, a few cm long rod with at least 3 mm diameter can be basically obtained from every master alloy, excepting the **P4** which is an "outsider".

The algorithm used to pin-point the best composition is described in the following, keeping the chronological development with the observations about GFA:

- **P1**, **P2**, **P3**- were made almost in the same time (at the beginning), to check the general behavior.
- **P4**- external supplier using industrial-grade raw materials, "ingredients" about which we don't have any information (gas atomized powders of that composition were used for a separate IFW project).
- **P5**- similar to **P1**, the purpose was to find out if there are differences between master alloys with pre-alloyed FeC and master alloys which were prepared by direct adding graphite particles in the melt.

In this moment is concluded that the best GFA has the **P2** alloy. The **P3** master alloy has also a good GFA, better than **P1** and far better than **P4** (from P4 was impossible

to cast something amorphous, excepting ribbons), but not as good as **P2**. The GFA of **P5** is similar to the one characteristic to **P1** and worse than **P3** or **P2**. The chemical composition of the **P2** (real composition) was known and then **Real-P2** alloy was produced, using pure elements (including traces, as revealed by chemistry).

- **P6** and **P7**- made to study the differences between 2 types of casting: ingot solidified in the ceramic crucible used for melting (= possible reaction with the crucible material) or evacuated (cast) in a mold.

Both **P6** and **P7** behave absolutely identical and have a limited GFA. So, the **casting paths are not very important**, but the use of the pure FeB from IFW did not help. It becomes clear that somewhere the **key ingredients** are linked with the use of **industrial FeP and FeB pre-alloys** from OCAS. In consequence, the new alloy **P8** was created:

- **P8**- which is different from **P2** through the use of crystalline Si instead of FeSi.

The GFA of **P8** is again very good, even better than **P2**. Now, in order to see which pre-alloy has the critical influence, **P9** and **P10** were created:

- **P9** with OCAS industrial FeP and the rest all pure elements
- **P10** with OCAS industrial FeB and the rest all pure elements (including pure FeP mechanically alloyed at IFW).

It was observed that from the last two master alloy, the **P9** is the one with better GFA. Thus the component which drastically enhances the GFA is contained in the FeP industrial pre-alloys supplied by OCAS. **P9** has a slightly better GFA than **P8**, but this is probably due by the fact that the B content is very small, so the used amount of FeB OCAS pre-alloy was in a small quantity. An alloy which would require a higher amount of FeB maybe would not have such good GFA. With other words, for this actual case there is no perceivable difference between the use of industrial FeB instead of more expensive crystalline B.

Tables 6.2 and 6.3 show the chemical composition of all $Fe_{74}Mo_4P_{10}C_{7.5}B_{2.5}Si_2$ master alloys studied, upon chemical analysis performed at IFW. The symbol "<" denotes contents less than 0.01% (detection limit), while "n.a." means not analyzed. The content is given in wt.%, excepting the O and S, which is given in wt. ppm. There one can see that the master alloys with the best GFA contain a small amount of Mn, as well as 180-200 ppm S. In fact, as it was further proved by several other casting experiments done in both labs (IFW and OCAS, exchange of other master alloys prepared at OCAS using industrial pre-aloys), the Mn seems to be the one which

drastically improve the GFA. However, its content should be still low enough, otherwise the GFA might be irreversible affected.

Table 6.2 The real chemical composition of all used master alloys (principal elements), chemical analysis performed at IFW.

Alloy	Fe	Mo	P	C	B	Si	O	S
Target composition	82.66	7.68	6.20	1.80	0.54	1.12	0	0
P1 (pure elements, FeC)	82.73	7.87	6.25	1.73	0.55	1.18	41	210
P2 (industrial FeP,FeB,FeSi)	82.10	7.77	6.76	1.76	0.47	1.21	75	200
P3 (all industrial)	80.97	8.11	6.47	1.78	0.52	1.32	60	90
P4 (outsider)	82.05	6.96	6.01	1.75	0.52	1.43	320	50
P5 (pure elements, C)	82.45	7.7	6.18	1.85	0.52	1.08	80	40
Real-P2	81.63	7.68	6.93	1.69	0.46	1.25	110	210
P6 (ingot)	81.12	7.65	6.24	1.80	0.51	1.14	60	30
P7 (cast)	80.20	7.59	6.56	1.72	0.53	1.23	140	180
P8 (industrial FeP & FeB)	81.95	7.70	6.49	1.74	0.47	1.17	60	180
P9 (industrial FeP)	82.10	7.55	6.48	1.73	0.55	1.15	50	190
P10 (industrial FeB)	82.76	7.63	5.99	1.73	0.47	1.23	80	210

Table 6.3 The real chemical composition of all used master alloys (secondary elements), chemical analysis performed at IFW.

Alloy	Mn	Ti	Al	Cr	Ni	Cu
Target composition	0	0	0	0	0	0
P1 (pure elements, FeC)	<	<	<	<	<	<
P2 (industrial FeP,FeB,FeSi)	0.11	<	n.a.	n.a.	n.a.	n.a.
P3 (all industrial)	0.71	0.16	n.a.	n.a.	n.a.	n.a.
P4 (outsider)	0.42	1.1	n.a.	n.a.	n.a.	n.a.
P5 (pure elements, C)	<	<	0.02	<	<	<
Real-P2	0.13	<	0.02	<	<	<
P6 (ingot)	0.67	0.25	0.02	0.05	0.04	0.03
P7 (cast)	0.87	0.76	0.02	0.09	0.04	0.03
P8 (industrial FeP & FeB)	0.12	0.06	0.02	0.02	0.04	0.08
P9 (industrial FeP)	0.11	0.06	0.02	0.03	0.03	0.06
P10 (industrial FeB)	0.03	<	0.02	0.02	0.03	0.02

In scientific literature many parameters which can characterize the GFA are defined. Not always they work, so as a rule of thumb it is preferred to judge the GFA through the possibility of casting samples with enlarged dimensions or with complicated geometries. For this reasons, we used as standards the copper mold in

which a 7 cm long cylinder may be cast. In this way, the maximum achievable diameter for which the sample is still amorphous was taken in consideration in order to quantify the GFA. For this $Fe_{74}Mo_4P_{10}C_{7.5}B_{2.5}Si_2$ alloy the predicted maximum diameter was 5 mm (for a 5 cm long cylinder); we easy cast long 4 mm diameter rods, we also cast 5 mm diameter rod and, with some efforts, it was possible to cast perfectly rings with dimensions: ϕ 29 mm x ϕ 19 mm x 2 mm. Few examples are presented in Figs. 6.1: rod with 3 mm diameter and a length of ~7 cm, rod with 4 mm diameter and a length of ~7.5 cm and the above mentioned rings. It should be underlined here that, to our best knowledge, the scientific literature **does not mention the possibility to directly cast a perfect ring-formed Fe-based BMG with such large dimensions.** This possibility opens the **direct gate toward the applications**. Such rings can be used straight forward as functional parts in different devices: magnetic sensors, actuators, magnetic clutches etc.

Fig. 6.1 Few examples of $Fe_{74}Mo_4P_{10}C_{7.5}B_{2.5}Si_2$ BMGs: rods with 3 mm diameter **P2** master alloy (upper side, left) and 4 mm diameter **P9** master alloy (above), as well as rings (**P9** master alloy) with dimensions ϕ 29 mm x ϕ 19 mm x 2 mm (left).

Due to the fact that all master alloys show a very good GFA, laborious structural studies must be performed in order to find out the effect of different impurities. Therefore, the amorphicity of all samples was carefully checked corroborating the data collected upon DSC measurements, XRD in transmission configuration using the synchrotron radiation and upon magnetic measurements (especially DC coercivity). Summarizing, the master alloys can be arranged in the following order, starting with the best GFA:

P9 = P8 ≈ P2 > P3 > P1 > P5 = P6 = P7 = realP2 = P10 >> P4

6.2 Thermal behavior for selected samples

As mentioned previously, all master alloys (except **P4**) have shown a relatively good GFA. In order to assess to possible influences of the different impurities presented in different master alloys, all samples were thoroughly investigated (DSC, XRD and magnetic measurements). The volume of the collected data is far too large to be summarized here. This is why only few selected data will be presented further. Anyway, to give a more accurate image, here samples cast from **P2**, **P3**, **P4** and **P5** master alloy were chosen. The GFA varies in this order (the worst is the first):

P4 < P5 < P3 < P2

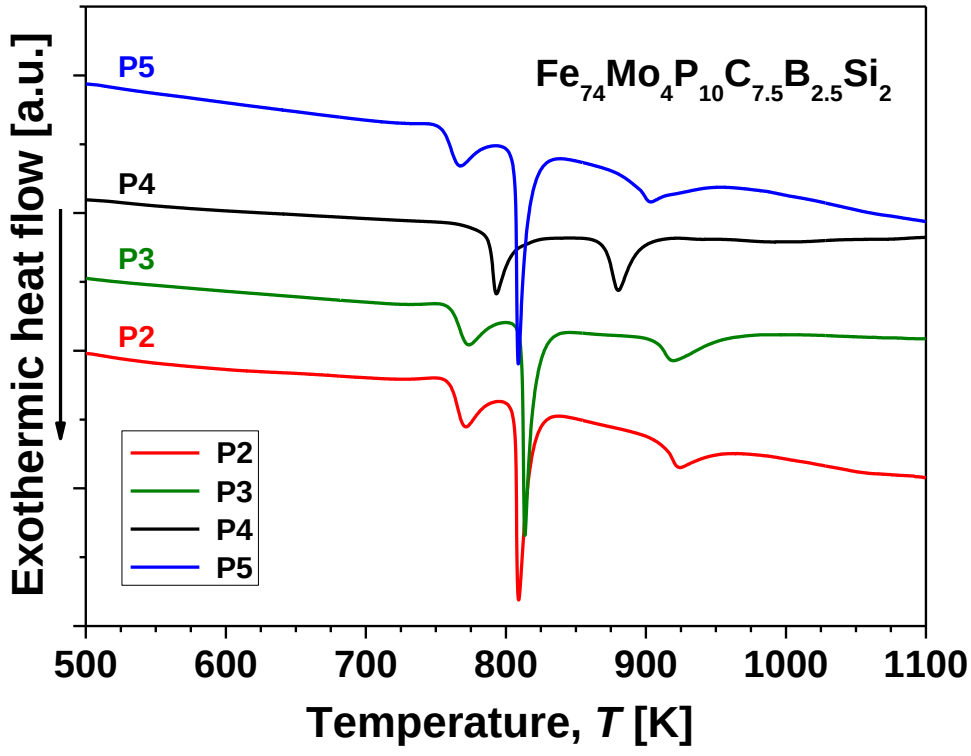

Fig. 6.2 DSC traces of several amorphous rod samples made using the alloys **P2**, **P3**, **P4** and **P5**. All samples are amorphous, excepting that made from **P4**.

In Fig. 6.2 one can remark that the sample cast using the **P4** master alloy is different. There no glass transition is apparent and only two small exothermic events

are present. In the following, Table 6.4 summarizes the main thermal characteristics. It is remarkable that the experimentally observed GFA variation is confirmed by the thermal parameters (which, anyway, are very close to each other- excepting the **P4** sample). The best gauge to judge here is the crystallization enthalpy.

Table 6.4 Thermal stability data and the main GFA parameters measured for glassy sample presented in Fig. 6.2: glass transition temperature T_g, crystallization temperatures T_{x1}, T_{x2} *and* T_{x3}, crystallization enthalpies ΔH_x, extension of the supercooled liquid region (SLR) $\Delta T_x = T_x - T_g$, liquidus temperature T_{liq}, reduced glass-transition temperature T_{rg} and parameter $\gamma = T_x / (T_g+T_{liq})$. The DSC data were measured upon isochronal heating with 20K/min heating rate.

Master alloy	T_g [K]	T_{x1} [K]	$-\Delta H_1$ [J/g]	ΔT_x [K]	T_{x2} [K]	T_{x3} [K]	T_{liq} [K]	T_{rg}	γ
P2	725	759	12.53	34	806	909	1266	0.57	0.381
P3	726	760	12.22	34	810	907	1274	0.57	0.380
P4		785	21.65		870		1257		
P5	721	754	11.52	33	806	891	1277	0.56	0.377

6.3 Crystallization behavior, corroboration of several methods

The crystallization behavior of $Fe_{74}Mo_4P_{10}C_{7.5}B_{2.5}Si_2$ BMGs is much more complicated as the one characteristic to $[(Fe_{0.5}Co_{0.5})_{0.75}B_{0.2}Si_{0.05}]_{96}Nb_4$ BMGs (the previous studied) BMGs. For the $[(Fe_{0.5}Co_{0.5})_{0.75}B_{0.2}Si_{0.05}]_{96}Nb_4$ samples it was found that only one crystalline phase forms upon heating, i.e. the $Fe_{23}B_6$-type phase. In the case of $Fe_{74}Mo_4P_{10}C_{7.5}B_{2.5}Si_2$ BMGs, several different phases form. This is not unusual and the concurrence of different crystalline phases in fact enhances the GFA. The formation of several types of crystalline phases is possible if the atoms have high mobility to diffuse upon long distances there. Therefore high temperatures are necessary to activate the diffusion. Consequently, the amorphous phase has enhanced thermal stability against crystallization and thus increased GFA.

Due to the complexity of crystallization, data from magnetic measurements, i.e. thermomagnetic curves, were put together with the DSC and XRD results. Thermal analyze was performed using the high-temperature DSC, samples being heated from room temperature above the melting point using 20 K/min constant heating rate. The cooling was registered as well, performed at the same rate of 20 K/min, and the traces

are shown in Fig. 6.3. There are also figured the main temperatures. The crystallization proceeds through 2 main exothermic events, followed after ~50K by another exothermic event. The melting interval extends over almost 80 K, while the solidification is typical for an eutectic alloy. This proves that several different phases form from the amorphous state and are thermodynamically metastable. Upon cooling, the solidification is eutectic, characteristic for a good glass former. The small "jump" which appears on the cooling curve at a temperature slightly below 800 K is just a measurements artifact- the alloy moved in the DSC pan during cooling. Upon solidification the solidified alloy drop remained stuck to the bottom of the pan. By cooling, its volume changed and this raised the internal mechanical tensions, which finally had as result violent separation of the alloy from the DSC pan. The same behavior was noticed for other samples too, so it is probably because the alloy slightly reacts with the alumina pan or superficially penetrates its micropores.

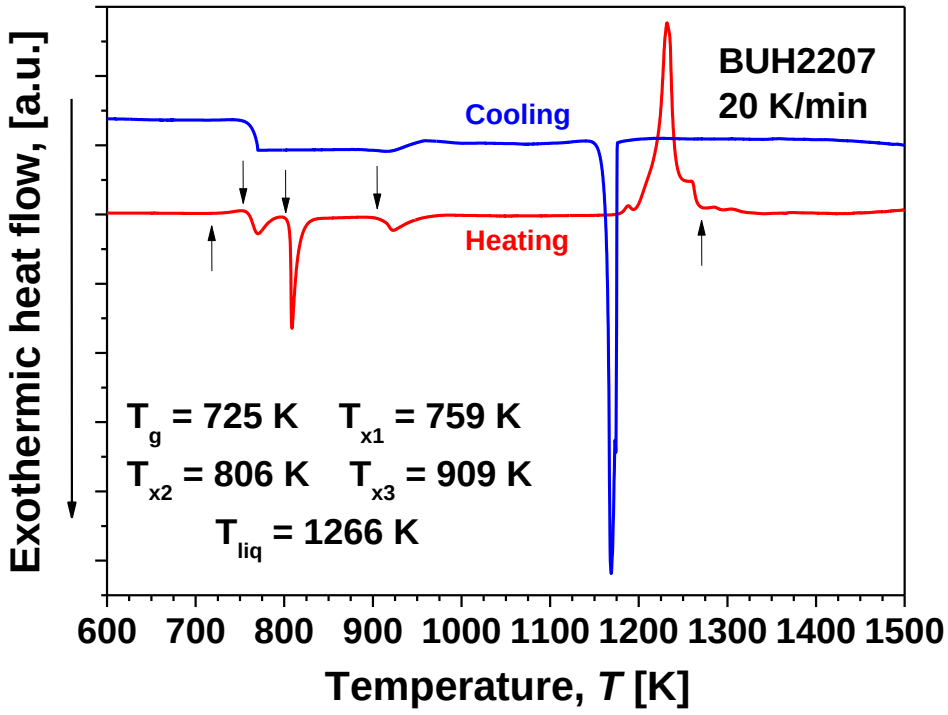

Fig. 6.3 DSC traces of an amorphous $Fe_{74}Mo_4P_{10}C_{7.5}B_{2.5}Si_2$ BMG rod made using the alloy **P2**. The main temperatures are marked by arrows.

For an Fe-based BMG, the glass transition temperature and the crystallization temperature are not extraordinary high. The extension of the supercooled liquid region (34 K), the reduced glass transition temperature (0.57) and γ parameter (0.381) indicate a relatively good GFA, almost normal for such kind of glasses (the thermal stability data and the main GFA parameters are summarized in Table 6.4).

In order to evaluate the crystallization behavior, few slices were cut from this sample and annealed in DSC up to temperatures immediately above the each exothermic event (i.e. at 795 K, 843 K and 983 K, respectively). The heating and especially the cooling was carefully monitored in the DSC, in order to rule-out the subsequent transformation of the partially crystallized slices. These curves are qualitatively presented in Fig. 6.4 (heat flow on the y axis, exothermic downward). From there it is clear that no additional transformation took place and the further investigation of those samples will bring information only about the respective metastable phases which form there.

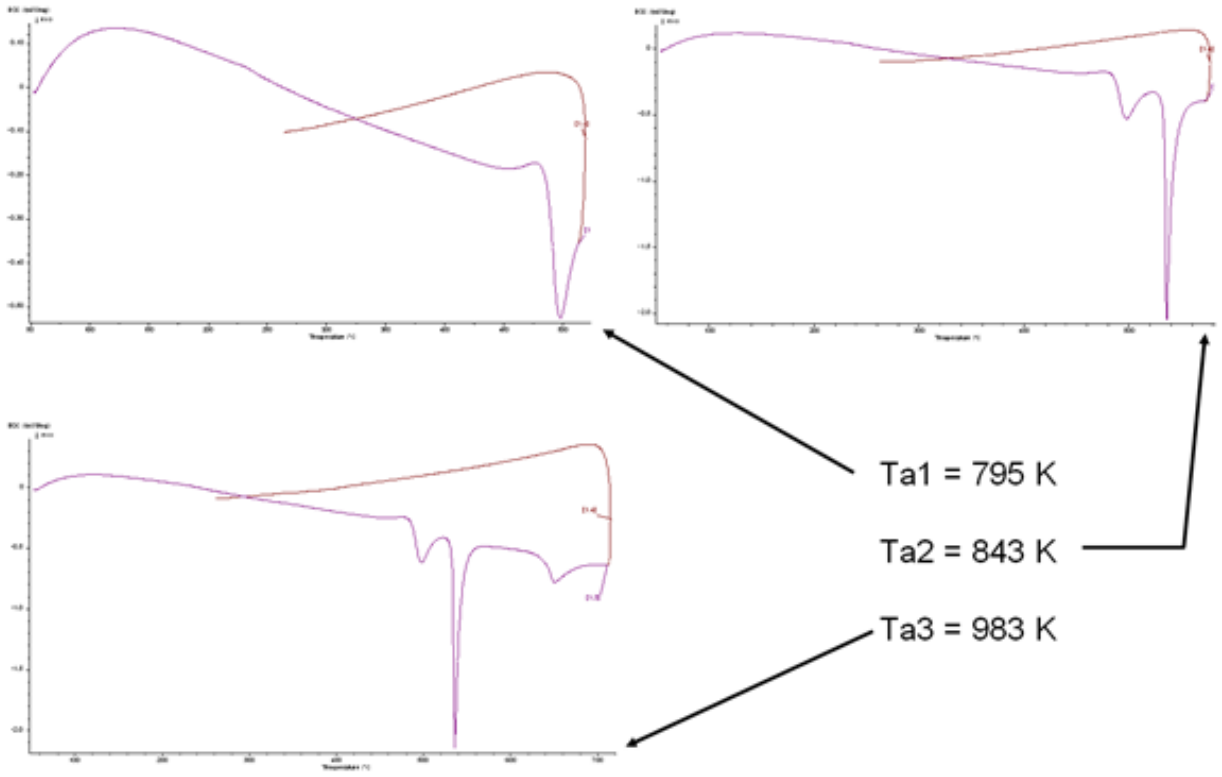

Fig. 6.4 The DSC heating and cooling curves (measured at 20 K/min) during the annealing of FeMoPCBSi BMG samples. The annealing temperatures are also indicated. The exothermic heat flow is on the vertical axis (y-axis) and points downward, as usual shown through this entire work.

Fig. 6.5 shows globally the entire crystallization behavior, as recorded by *in-situ* XRD, details for the first and second broad maxima. Fig. 6.6 shows the diffraction patterns corresponding to only 4 temperatures, i.e. room temperature and the three annealing temperatures. As it can be observed, the fully amorphous sample at room temperature shows upon heating an extremely complicated composite structure which cannot be simply resolved only upon XRD analysis. Anyway, the crystalline peaks can give at least some hints toward the possible phases.

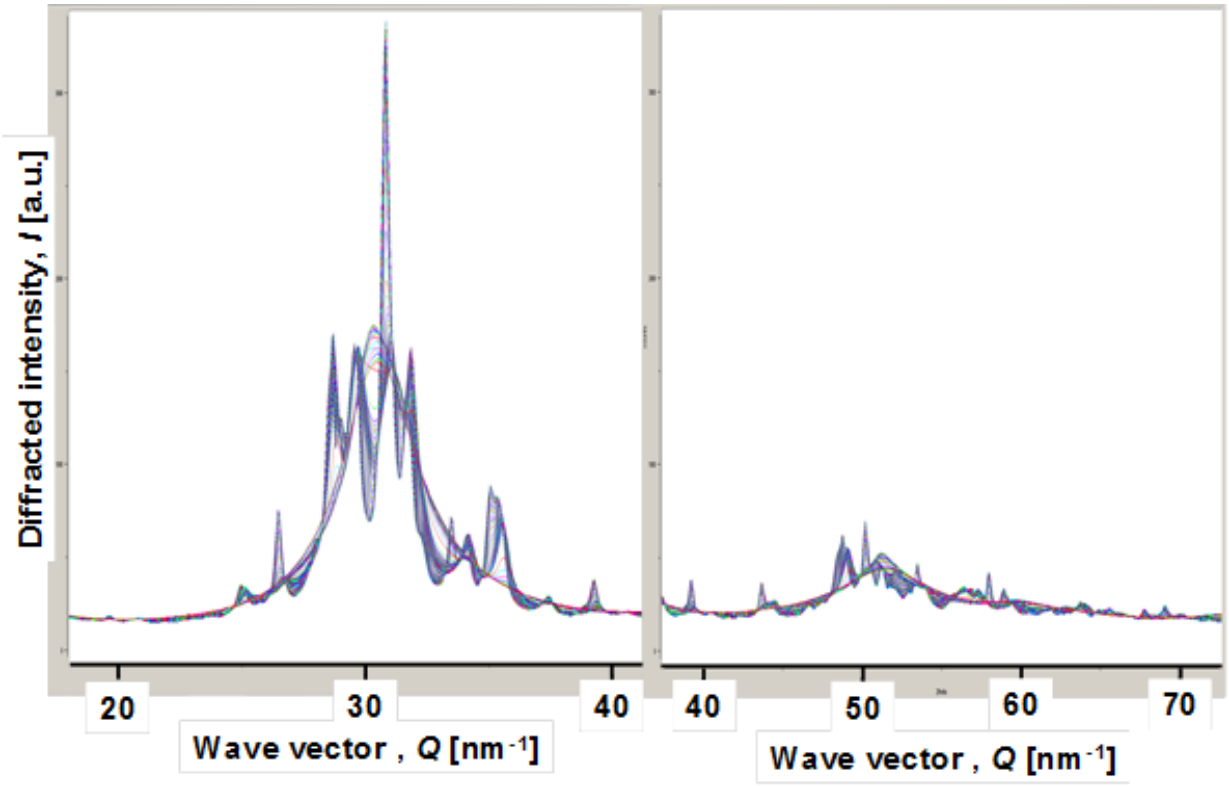

Fig. 6.5 $Fe_{74}Mo_4P_{10}C_{7.5}B_{2.5}Si_2$ BMG: in-situ crystallization behavior, details around the first and second broad maxima.

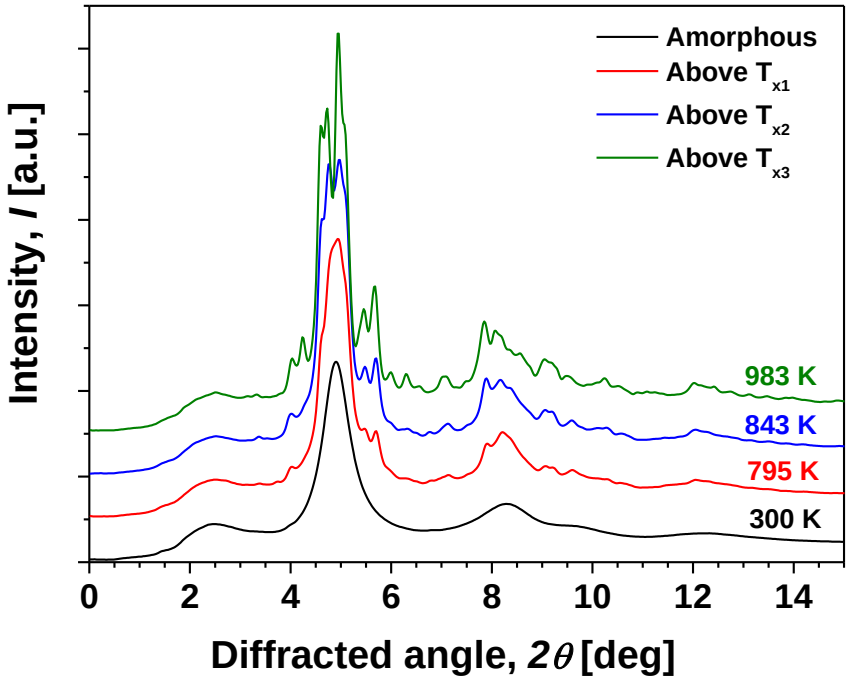

Fig. 6.6 Crystallization details of the RT and annealed samples. This time, for identification using the available databases, the patterns are presented as a function of 2θ. The used monochromatic X-ray has λ = 0.017615 nm. The annealing temperatures are also marked.

The HR-TEM would not bring too much light in this problem, because for such investigations only limited areas are available. So the next useful method is the thermomagnetic characterization. The samples annealed in DSC, as well as an as-cast samples, were heated in the Faraday balance and the curves are presented in Fig. 6.7. With X1, X2 and X3 are named the first, second and third crystallization events, respectively.

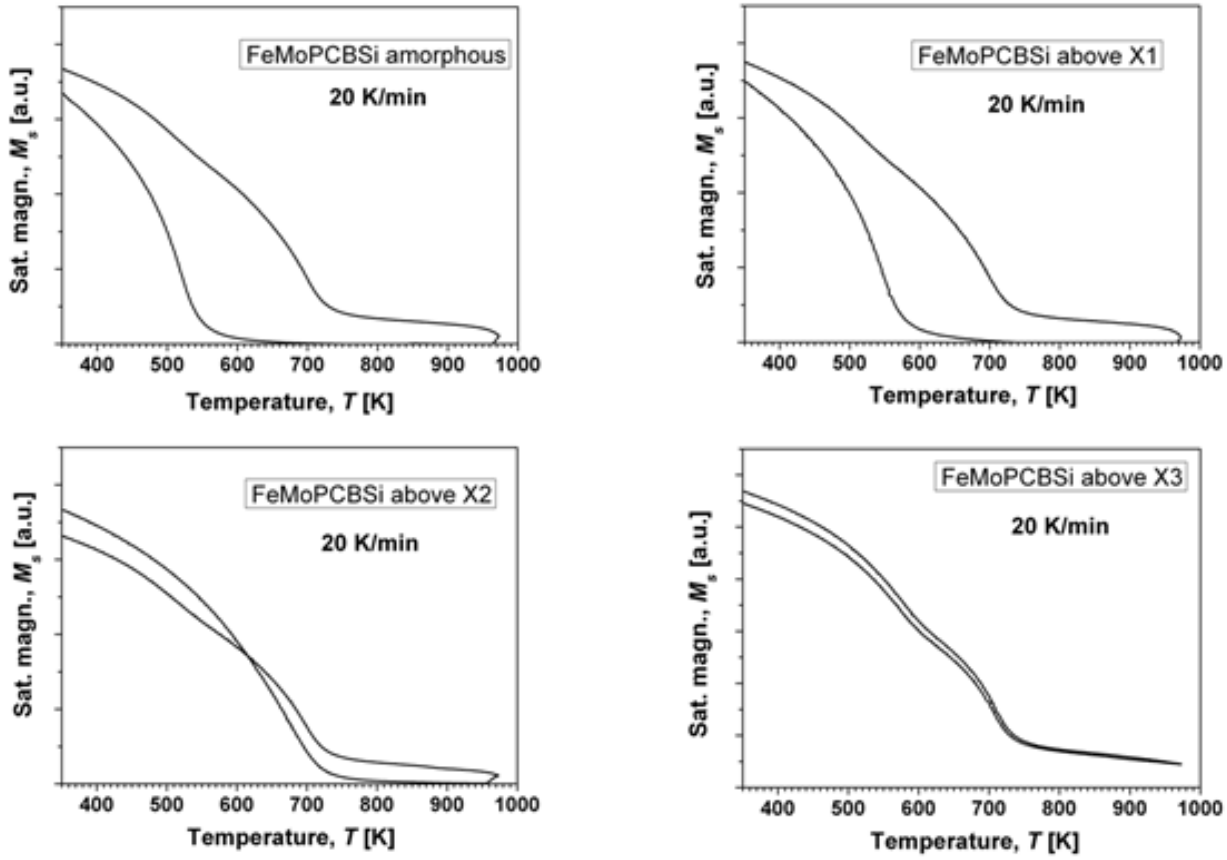

Fig. 6.7 The thermomagnetic curves recorded for as-cast and annealed samples.

Even for the sample annealed above the second crystallization event only one single ferro-paramagnetic transition can be observed. It means that if by crystallization other magnetic phases form, they have much lower Curie temperature- or there only non-magnetic phases form. The only other magnetic phase appears at ~970 K, which corresponds somehow to the (allotropic) transformation seen in the DSC (see Fig. 6.3). Most probably this phase is α-Fe. This is (again) consistent with the DSC measurements, because there around 1200 K, prior melting, it is an endothermic event which usually corresponds to the α to γ transition of Fe. The pure Fe has the ferrite-austenite transition at 912 °C = 1185 K. Most probably there is not a pure ferrite, because of large amount of metalloids in the composition- so is a bcc Fe solid solution.

The other magnetic phases which may be present there can be the tetragonal **Fe_3P** (***Tc* = 686-716 K**), orthorhombic **Fe_3C** (***Tc* = 470-485 K**) and the complex cubic (fcc) **$Fe_{23}B_6$-type phase** (which has a **wide distribution of *Tc*** values, depending on the number of the magnetic atoms in the unit cell). After last transformation, the cooling curves are identical and show 3 inflexion points indicating the presence of 3 different magnetic phases. The hysteresis behavior of all 4 samples (as cast and annealed immediately above each crystallization event) is shown in Fig. 6.8. There are two insets, showing in clear the behavior around origin and at the saturation. The slightly apparent shift of the curves around origin are caused by the detection limit of the VSM-basically its sensitivity is not better than 1 Oe, which is already almost 80 A/m, far more than the coercivity of the as-cast sample. From the entire hysteresis curves one can see that the main magnetic transformations take place during the second crystallization event, when most probably the rest of the amorphous matrix transforms. All magnetic data measured for all these sample (coercivity, magnetic saturation and Curie temperatures) are summarized in Table 6.5. Interesting is that after second crystallization t**he coercivity decreases**, from 10,000A/m to 8,000 A/m, most probably due by the formation of other soft magnetic phase(s). The behavior can be seen in the upper left corner inset in Fig. 6.8 and the values are given in Table 6.5.

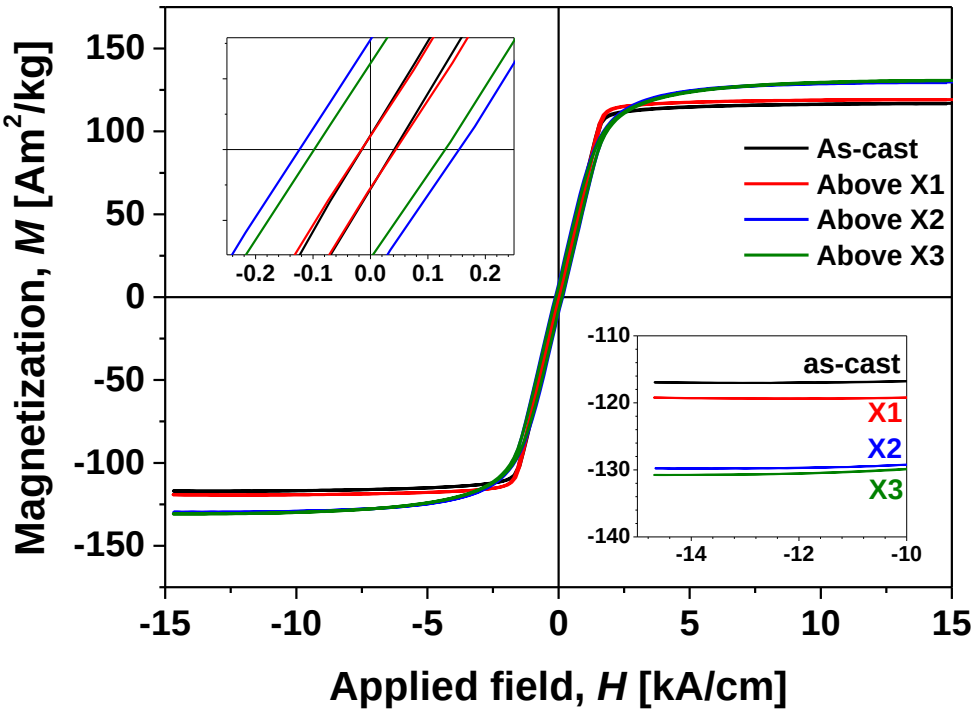

Fig. 6.8 Hysteresis curves for as cast and annealed BUH2207 glassy sample. The insets show the behavior around origin (inset in the second quadrant) and at the saturation (inset in the fourth quadrant).

Table 6.5 Summary of characteristic magnetic data- coercivity, magnetic saturation and Curie temperature.

		amorphous	above X1	above X2	above X3
H_c [A/m]		1.4	60	10,000	8,000
M_s [Am^2/kg]		117	119	130	130
T_c [K]	Heating	515	538	644	647 / 724
	1st cooling	much higher T_c (most probably α-Fe)			
	2nd cooling	692	691	696	722
	3rd cooling	626	628	621	644

Putting all results together, we can conclude that the thermal evolution is in the following way (for details the heating DSC curve is re-plotted in Fig. 6.9):

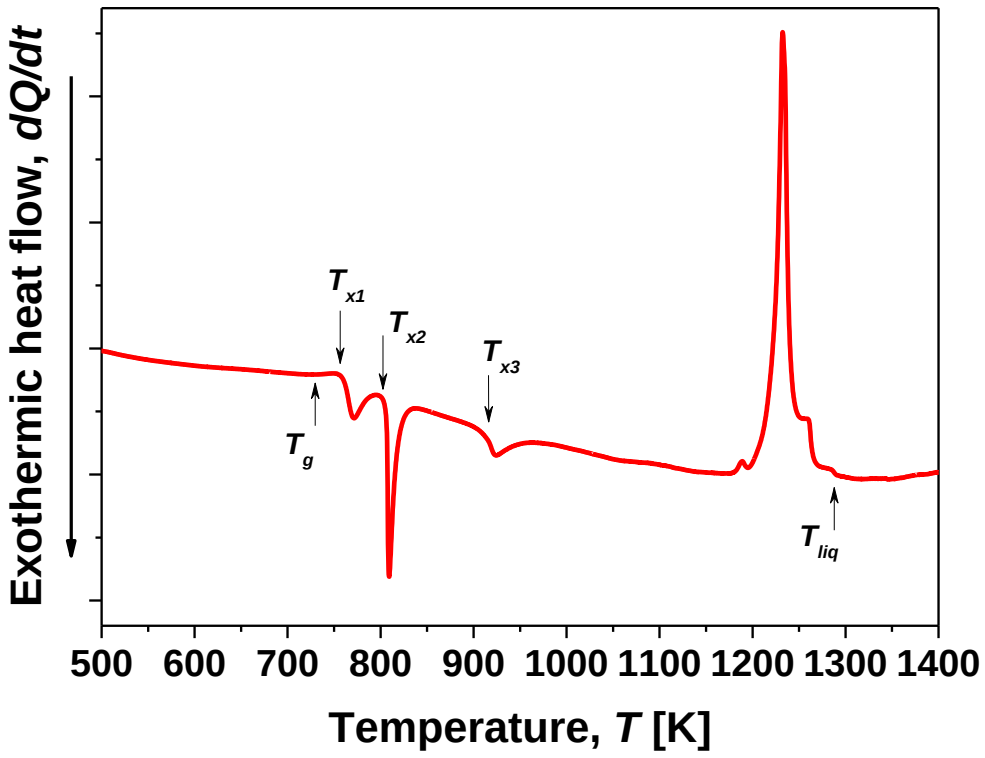

Fig. 6.9 Typical DSC thermogram measured at 20 K/min heating rate for a $Fe_{74}Mo_4P_{10}C_{7.5}B_{2.5}Si_2$ BMG rod.

- Start: fully amorphous (BMG)
- **First exothermic** event (partial crystallization): fcc γ-Fe forms, together with Mo-P, Mo-C, Mo-B and/or Mo-Si. All of them embedded in a residual amorphous matrix (with a different chemical composition than the starting one).
- **Second exothermic** event: crystallization of the remained amorphous matrix. There $(Fe,Mo)_3P$ forms from the residual amorphous matrix, which will coexist with already formed Mo-P, Mo-C, Mo-B and/or Mo-Si.
- **Third exothermic** event: that it is an allotropic transformation. The fcc γ-Fe will transform in bcc α-Fe (event clearly visible upon thermomagnetic measurements), the $(Fe,Mo)_3P$ will be depleted in Mo, $Fe_{23}B_6$ forms (consuming some of the γ-Fe) plus whatever quantities of Mo-P, Mo-C, Mo-B and/or Mo-Si.

And then approaching the melting:

- **First endothermic** event (small, at ~ 1180 K): the structural transformation of Fe from bcc α to fcc γ. The temperature for pure Fe is 1185 K, which fits well to the one measured by DSC.
- **Second endothermic** event: melting of almost everything is there, excepting some carbides/borides/silicides (with a very high melting point).
- **Third and last (small) endothermic** events: in this point there coexist Liquid + high melting Solid(s); the coexistence will make the Solid(s) (carbides/borides/silicides) to melt. The onset of the very last event is considered to be the *liquidus temperature*. Above this temperature the DSC trace still shows some small tremors, which are artefacts and may be due by a slight reaction between the melt and alumina crucible (pan).

The cooling curve (blue curve in Fig. 6.3) nicely show the nearly-perfect eutectic character of the studied composition (very sharp exothermic- i.e. solidification- peak). The solidification takes place at a temperature lower than Fe γ–α transition, so it is clear that the metastable austenite forms only upon heating from amorphous phase. The appearance of the fcc Fe phase can be triggered by the presence of a high amount of metalloids, especially C, which basically lower the transition from 1185 K to 1013 K and in the case of metastable alloys this phase may be frozen-in at RT upon rapid heating (similar with the case of austenitic steels).

Chapter 7
Developing new BMGs starting from $Fe_{77.5}P_{12.5}C_{10}$ composition

As the first investigated composition $[(Fe_{0.5}Co_{0.5})_{0.75}B_{0.2}Si_{0.05}]_{96}Nb_4$ at.% was obtained starting from the FeBSi heart, which allows to produce only thin amorphous ribbons, we tried to transfer this approach to FePC family. As starting point was considered the $Fe_{77.5}P_{12.5}C_{10}$ alloy, which was reported to be amorphous up to a thickness of 360 µm [Ino82]. Following the previous algorithm, the target compositions were set to $[(Fe_{0.5}Co_{0.5})_{77.5}P_{12.5}C_{10}]_{96}Nb_4$. The high content of P and C makes impossible the simultaneously use of FeC, FeP and FeNb pre-alloys. From the homogeneity reasons, at least FeP (P evaporates) and FeNb (Nb has extremely high melting point) pre-alloys must be used. First trials were with $(Fe_{77.5}P_{12.5}C_{10})_{96}Nb_4$ and $[(Fe_{0.9}Co_{0.1})_{77.5}P_{12.5}C_{10}]_{96}Nb_4$ compositions. The motivation of developing BMGs with the mentioned compositions resides in the fact that they should have a higher saturation magnetization and it can be **a new class of magnetic BMGs** (due to the difficulties in preparation, this composition is not mentioned in literature up to now). Meanwhile, playing with the ingredients and using the accumulated experience one can assess the effect of minor additions or impurities on the GFA.

7.1 $(Fe_{77.5}P_{12.5}C_{10})_{96}Nb_4$ master alloy

The knowledge accumulated during the preparation of the first master alloy was transferred to this new alloy. This new master alloy has the nominal composition of **82.87Fe 7.41P 2.30C 7.41Nb** in wt.%. The preparation route of the first 100 g of master alloy was:

- Eutectic pre-alloy 25Fe 75Nb wt.% by arc-melting pure elements (9.88 g).
- Eutectic pre-alloy 95.8Fe 4.2C wt.% by induction melting pure elements (Fe + graphite) (54.762 g)
- Pre-alloy FeP by induction melting of mechanically alloyed powders (33.681 g).

- All of the mentioned pre-alloys, plus some extra Fe (1.667 g), were induction melted.

The resulted master alloy **was not chemically analyzed** because it is supposed to be very pure and with the nominal composition (no elements lost). However, at a first glance, the alloy does not seem to be homogenous and the first attempts to cast amorphous rods completely failed. The preliminary investigations done by scanning electron microscope (SEM) shown interesting features: unreacted graphite and formation of carbides. The group of micrographs presented in Fig. 7.1 shows in detail these observations.

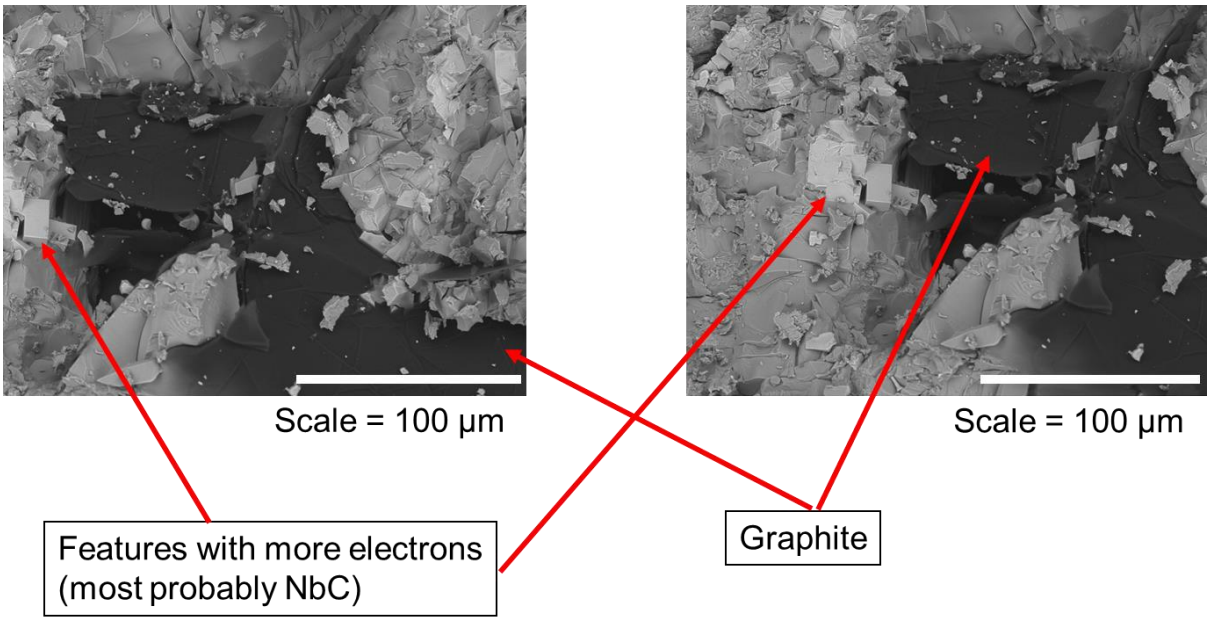

Fig. 7.1 SEM micrographs in back scattered mode showing the appearance of the master alloy $(Fe_{77.5}P_{12.5}C_{10})_{96}Nb_4$. There it is possible to observe the unreacted graphite and NbC.

The presence of the unreacted graphite and NbC is easily observable in Fig. 7.1. Details at higher magnifications are presented in Fig. 7.2. In fact, if for C there is no doubt, the carbides are questionable, but it is supposed to be pure NbC. First of all the images are taken with a detector sensitive to back scattered electrons, i.e. the images have a contrast upon composition. The lighter contrast indicates the presence of heavy elements (or elements with increased number of electrons), which in our case can be only Nb. Second, the heat of mixing between Nb and C is –102 kJ/mol, the highest among all constituents [Tak05]. The third aspect is linked to the geometrical consideration: NbC is fcc, and in the detailed micrographs (Fig. 7.2) one can observe

cleavage surfaces along the (111) plane. Therefore most probably the observed formations there are NbC. Unfortunately, NbC is very stable (–102 kJ/mol mixing enthalpy as compared, for example with –50 kJ/mol characteristic to FeC [Tak05]), with a very high melting point (~ 3600°C), which makes almost impossible to dissolve it once it was formed. But, for example, Nb is known to form silicates easily as well, which have also a very high melting point (over 1900 °C and reaching even 2520 °C), or in the $[(Fe_{0.5}Co_{0.5})_{0.75}B_{0.2}Si_{0.05}]_{96}Nb_4$ it was never observed to form. Most probably, the formation of NbC can be somehow avoided. The presence of unreacted graphite probably comes from the FeC pre-alloy, which in this case seems to be inhomogeneous. The presence of free C also promotes the formation of the NbC. The free C particles have irregular shapes, the grains have even more than 100 µm. The dimension of NbC crystals is arround 15-20µm.

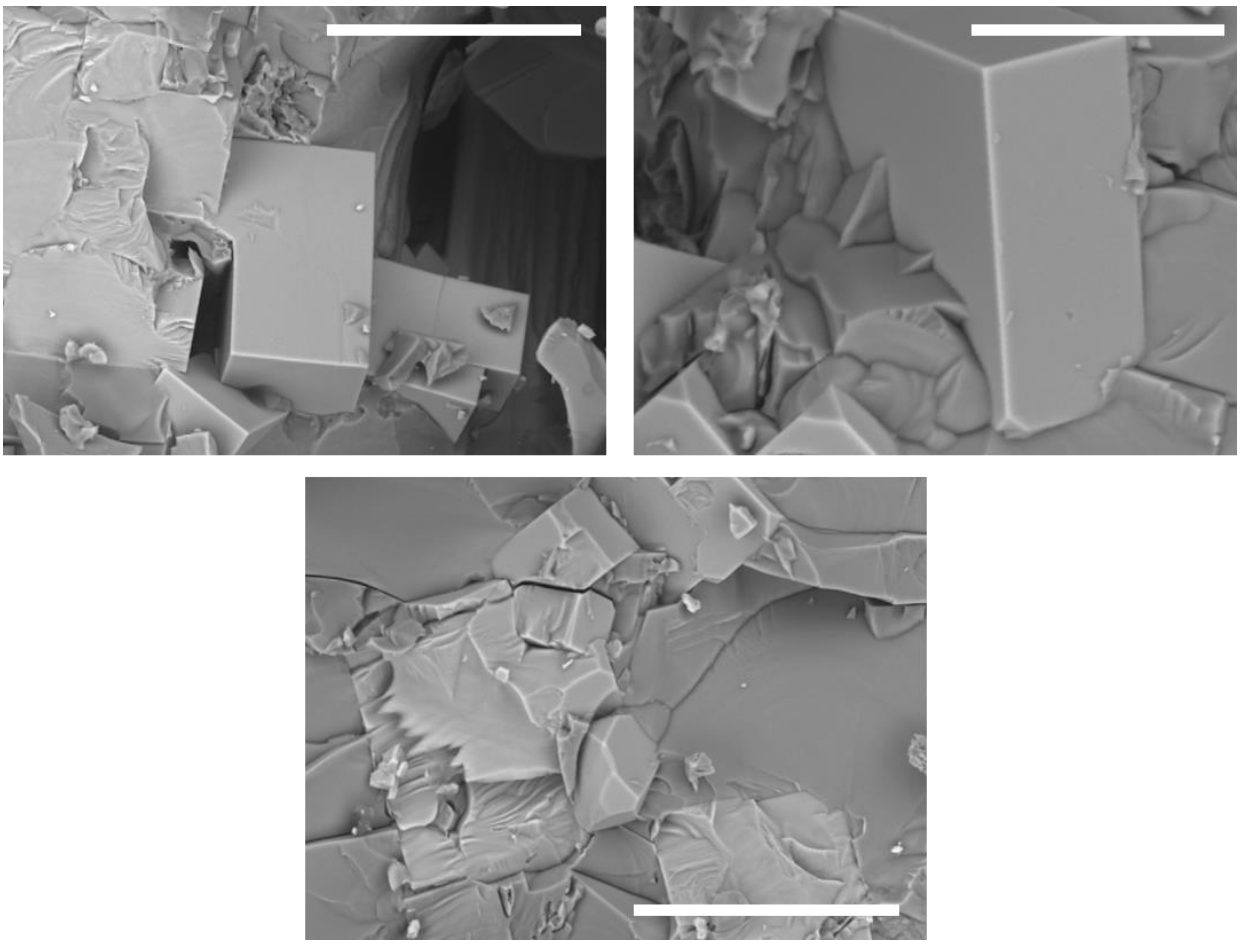

Fig. 7.2 Details at higher magnification clearly showing the NbC. The length of the white bar (the micrograph scale) is 20 µm (for clarity and better observation the micrographs were not overloaded with additional legends).

7.2 The $(Fe_{77.5}P_{12.5}C_{10})_{96}Nb_4$ master alloy, second attempt, and the new $[(Fe_{0.9}Co_{0.1})_{77.5}P_{12.5}C_{10}]_{96}Nb_4$ master alloy

Using this time other FeC pre-alloy, separately made in induction by melting together pure Fe and graphite particles and which is certainly homogeneous, two new master alloys were prepared. One has the previously shown composition $(Fe_{77.5}P_{12.5}C_{10})_{96}Nb_4$ and in the second Co replaces 10 % of Fe, obtaining in this way the $[(Fe_{0.9}Co_{0.1})_{77.5}P_{12.5}C_{10}]_{96}Nb_4$ composition.

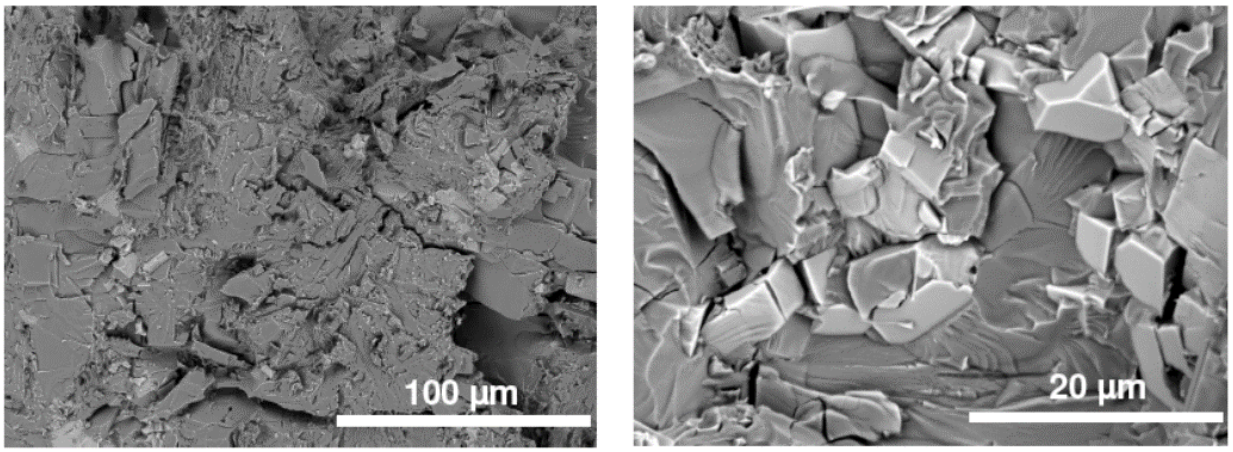

Fig. 7.3 SEM micrograph showing the appearance of $(Fe_{77.5}P_{12.5}C_{10})_{96}Nb_4$ master alloy made using pure FeP, FeC and FeNb pre-alloys.

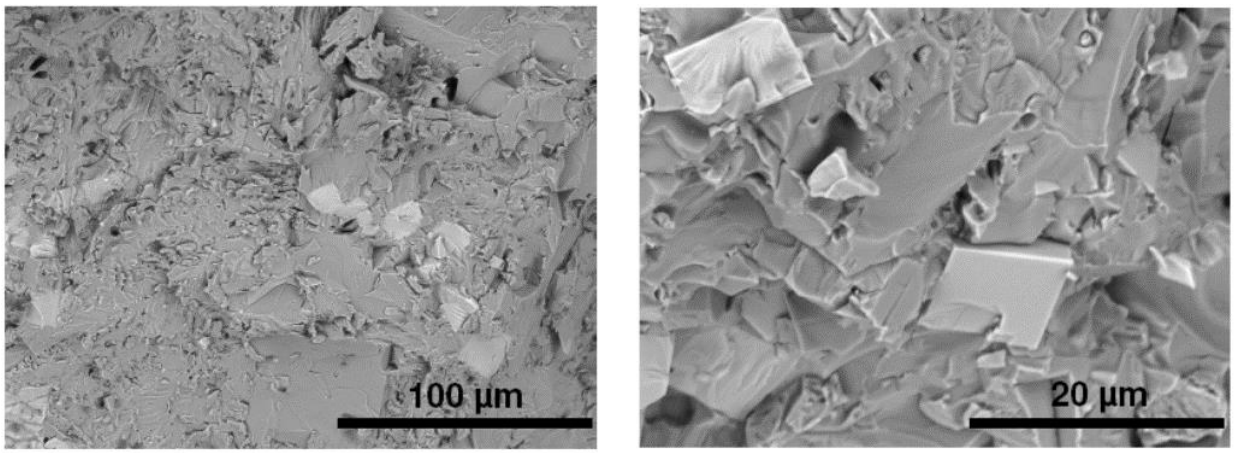

Fig. 7.4 SEM micrograph showing the appearance of $[(Fe_{0.9}Co_{0.1})_{77.5}P_{12.5}C_{10}]_{96}Nb_4$ master alloy made using pure FeP, FeC and FeNb pre-alloys, plus pure Co.

Both alloys were tested by copper mold casting. The results were better and the GFA seems to increase once the Co content increases. From the composition with 10 at.% Co it was possible to cast even a **1 mm diameter rod**, which is **mostly**

amorphous. This is an indication that the GFA is increased by replacing Fe with Co and such results, to our knowledge, **were not reported in literature** up to now. The SEM investigations (Figs. 7.3 and 7.4) proved only the presence of NbC in the master alloys (i.e. not unreacted graphite), but this time the crystals are much smaller in dimension and less volume fraction, and it is believed that during melting prior casting they dissolve completely in the molten alloy mass. Also, probably if the Co content will increase, their formation will be completely avoided. The global homogeneity of the both alloys is better than the previous case.

As a possible development toward industrial up-scaling the following route is proposed:

- clean FeP pre-alloy (i.e. mechanically alloyed) has to be used. It is impossible to bring controlled amount of P in the alloy in other way.

- The rest of the pure elements can be melted in arc, using the industrially known procedure of arc melting with a consumable electrode. In this way, by using a graphite electrode, a higher amount of C can be alloyed.

A second route is proposed, as follows:

- First an eutectic 25Fe 75Nb (wt.%) is made upon arc-melting.

- Then FeP pre-alloy together with pure Co, eutectic FeNb and graphite particles are melt in induction furnace.

Summary and conclusions

The bulk metallic glasses (BMGs) are a new class of materials, discovered around 1995. They are metallic alloys with amorphous structure. Due to their particular structure, they may achieve interesting properties, like high strength, high hardness, increased wear resistance, increased fatigue limit, increased corrosion resistance, as well as extremely good soft magnetic properties as low coercivity, high saturation magnetization, high permeability and low core losses. The ferromagnetic Fe-based glasses are not the very best glass formers, but they have the highest stability against crystallization, enhanced corrosion resistance and soft magnetic properties which cannot be attained by the regular crystalline alloys. All these properties make the Fe-based BMGs very attractive for industrial application.

The amorphous structure is metastable. In order to retain the amorphous structure at room temperature several conditions must be fulfilled. There are limitation regarding the composition and the cooling rate. Fe-based BMGs are of the type transition metals (75-80 at.%)-metalloid (25-20 at.%), with usually more than three components. The metals are mainly Fe, with substitution of Co or/and Ni, with small addition of Nb, Mo, Ta or Zr, and the metalloids are B, P, C, Si. The BMGs are usually obtained by rapid cooling the alloy from the melt. The critical cooling rate should be high enough to avoid the nucleation of the crystalline phase, in this specific case of Fe-based it is of the order of several hundreds of K/s.

The crystalline phase may form by homogeneous or heterogeneous nucleation. If the homogeneous nucleation can be avoided by rapid cooling, the heterogeneous nucleation usually lowers the energy barrier and can starts even at high cooling rates. The heterogeneous nucleation usually takes place around crystalline seeds which may be in the melt. These seeds are foreign inclusions like oxides or atoms which don't participate at the glass formation (impurities). This is why usually a very pure alloy is required for casting a BMG.

The current work started with literature alloy $[(Fe_{0.5}Co_{0.5})_{0.75}B_{0.2}Si_{0.05}]_{96}Nb_4$. Several master alloys using different raw materials (only pure elements, pure elements plus clean binary FeB pre-alloy, clean in-house made pre-alloys, industrial pre-alloys etc.) were prepared. The master alloys were done at IFW using pure, as well as industrial raw materials from OCAS. The foreign elements which are present in the master alloys, as well as impurities like O, C, N or S may influence the GFA, i.e. the

maximum achievable diameter for which the cast rod samples are still amorphous. Also, when an amorphous sample is made using an alloy with several impurities, its magnetic properties may change- especially the saturation magnetization become smaller and the coercivity increases. Therefore, besides the typical DSC and XRD investigations, the magnetic measurements, and especially the coercivity, was used as a gauge to analyze the amorphicity degree of the sample.

The $[(Fe_{0.5}Co_{0.5})_{0.75}B_{0.2}Si_{0.05}]_{96}Nb_4$ alloy is presented in literature as being one which assures the preparation of 5 mm diameter and 5 cm long fully amorphous samples, but here the maximum achievable diameter was 3.3 mm. It is believed that the oxygen content in the alloy may influence the GFA when the oxygen is bonded in oxides, which further may act as seeds for heterogeneously nucleation of crystalline nuclei. In order to check this influence, several amorphous rods with the composition $[(Fe_{0.5}Co_{0.5})_{0.75}B_{0.2}Si_{0.05}]_{96}Nb_4$ were prepared under different atmosphere, i.e. under different partial pressures of oxygen. The results were systematized and it seems that there does not exist a direct link between the GFA and oxygen content, or at least not as strong as in the case of other BMGs (for example in the case of Zr-based BMGs). **Most important for the GFA seems to be the actual composition of the master alloy**, i.e. a **deviation of 0.5-1 wt% from the nominal composition changes drastically the behavior**. The work done up to now leads toward the following aspects, which may explain the behavior of at least some classes of Fe-based BMGs.

- The $[(Fe_{0.5}Co_{0.5})_{0.75}B_{0.2}Si_{0.05}]_{96}Nb_4$ BMG may contain very small volume fraction of nanocrystalls, or even nuclei, which do not affect the macroscopic properties. This particular SRO is responsible for further appearance of $Fe_{23}B_6$-type phase upon heating (annealing).
- Amorphous $[(Fe_{0.5}Co_{0.5})_{0.75}B_{0.2}Si_{0.05}]_{96}Nb_4$ samples show similar behavior and similar properties, regardless the used master alloy.
- For amorphicity (and GFA), the most important fact is the cooling procedure (cooling rate) rather than the used alloy. However, more important than the impurities seems to be the actual composition of the master alloy. A deviation of 0.5 wt% from one or other element could drastically affect the GFA.
- When the $[(Fe_{0.5}Co_{0.5})_{0.75}B_{0.2}Si_{0.05}]_{96}Nb_4$ samples do not become fully amorphous upon casting, the crystalline phases which form there are the equilibrium phases, not the metastable $Fe_{23}B_6$-type. The foreign

elements which may deteriorate GFA are therefore those which stabilize the corresponding equilibrium crystalline phases.

- The resistance of the $[(Fe_{0.5}Co_{0.5})_{0.75}B_{0.2}Si_{0.05}]_{96}Nb_4$ BMGs against crystallization and the corresponding activation energy is very high. However, the incubation time is almost zero, once the glass transition temperature attained, the crystallization starts within seconds

The second literature composition studied here is $Fe_{74}Mo_4P_{10}C_{7.5}B_{2.5}Si_2$. This BMG was presented at the ISMANAM 2007 Conference as being a composition which allows the preparation of BMGs up to 5 mm diameter and a length of 5 cm. It was found out here that the GFA is really very high, rods with 4 mm diameter and 7 cm length can be easily reached upon casting, even when dirty raw materials are used. So, the advantage of such alloy is the good GFA, a good saturation magnetization due to the high Fe content and also it seems to have rather good mechanical properties (not very brittle, which may enhance the application field). At the first glance, the presence of Mo is a disadvantage (because of its price which is twice as high as the Co price) but in comparison with the FeCoBSiNb alloy it should be cheaper.

In order to study the GFA of the $Fe_{74}Mo_4P_{10}C_{7.5}B_{2.5}Si_2$ alloy, 11 types of master alloys with different ingredients were prepared. Further they were designated as P1, P2, …, P10 and RealP2. Summarizing, the alloys can be arranged in the following order, starting with the best GFA:

P9 = P8 ≈ P2 > P3 > P1 > P5 = P6 = P7 = realP2 = P10 >> P4

Crystallization studies, done *in-situ* using high-energy high intensity synchrotron beam at ESRF Grenoble, France, clearly shown that the crystallization mechanism of $Fe_{74}Mo_4P_{10}C_{7.5}B_{2.5}Si_2$ BMG is completely different from the one observed for the previously studied $[(Fe_{0.5}Co_{0.5})_{0.75}B_{0.2}Si_{0.05}]_{96}Nb_4$ BMGs- or other Fe-based compositions which usually develop upon crystallization the brittle $Fe_{23}B_6$-type crystalline phase. As a consequence, impurities which may affect the GFA of one composition could not affect the GFA of the other and vice-versa.

It was generally accepted that the oxygen content in the alloy may influence the GFA when the oxygen is present as oxides, which further may act as seeds for heterogeneously nucleation of crystalline nuclei. Moreover, the presence of other light elements as, for example, sulfur, was believed to hinder the glass formation. Our findings clearly show that in the case of $Fe_{74}Mo_4P_{10}C_{7.5}B_{2.5}Si_2$ the GFA is enhanced

when some foreign elements are present in the alloy. This is why such BMGs can be easily prepared used industrial-grade raw materials.

Up to now the BMGs are produced only at a small scale, due in principal by the fact that the composition must be very good controlled. It was found that in the case of the $[(Fe_{0.5}Co_{0.5})_{0.75}B_{0.2}Si_{0.05}]_{96}Nb_4$ a master alloy with high purity is required, while for $Fe_{74}Mo_4P_{10}C_{7.5}B_{2.5}Si_2$ the purity does not play such important role. Moreover, the master alloy needs a small content of foreign elements in order to retain the glassy state at room temperature. **These important findings were patented**, as for example in the following:

> Nele Van Steenberge, Daniel Ruiz-Romera, Mihai Stoica, Uta Kühn, Jürgen Eckert, world patent **WO 2013087627 A1** or European patent **EP2791376A1**

Moreover, transferring the knowledge accumulated by studying the role of the impurities on the glass-formation in the case of $[(Fe_{0.5}Co_{0.5})_{0.75}B_{0.2}Si_{0.05}]_{96}Nb_4$ and $Fe_{74}Mo_4P_{10}C_{7.5}B_{2.5}Si_2$ alloys, two **new BMG forming alloy compositions** were designed: $(Fe_{77.5}P_{12.5}C_{10})_{96}Nb_4$ and $[(Fe_{0.9}Co_{0.1})_{77.5}P_{12.5}C_{10}]_{96}Nb_4$. Also, the possible preparation routes, at laboratory and industrial scale, are proposed.

References

[Ana87] T. R. Anantharaman, C. Suryanarayana, *Rapidly solidified metals: a technological overview*, Trans Tech Publications, Switzerland-Germany-USA, (1987).

[ASM92] ASM Handbook: vol. 1,2 *Metals handbook*, vol. 3 *Alloy phase diagram*, ASM International, Materials Park Ohio, USA (1992).

[Avr39] M. Avrami, *J. Chem. Phys.* **7** (1939) 1103.

[Bec35] R. Becker, W. Döring, *Ann. Phys.* **24** (1935) 719.

[Bit06] T. Bitoh, A. Makino, A. Inoue, A.L. Greer, *Appl. Phys. Lett.* **88** (2006) 182510.

[Boe89] F.R. De Boer, R. Boom, W.C.M. Mattens, A.R. Miedema, A.K. Niessen: *Cohesions in metals*, North-Holland, Amsterdam, The Netherlands (1989).

[Buc60] E.R. Buckle, A.R.Ubbelohde, *Proc. Roy. Soc.* **259** A, (1960) 325.

[Cah93] W. Cahn: *Rapidly Solidified Alloys*, edited by H. H. Liebermann, Marcel Dekker, New York, (1993) 1–15.

[Che70] H.S. Chen, C.E. Miller, *Rev. Sci. Instrum.* **41** (1970) 1237.

[Coh59] M.H. Cohen, D. Turnbull, *J. Chem. Phys.* **31** (1959) 1164.

[Dav73] H.A. Davies, J. Aucote, J. B. Hull, *Nature Phys. Sci.* **246** (1973) 13.

[ESRF] Internet: European Synchrotron Radiation Facility, www.esrf.eu

[Fuj74] H. Fujimori, T. Masumoto, Y. Obi, M.Kikuchi, *Jpn. J. Appl. Phys*. **13** (1974) 1889.

[Ful25] G.S. Fulcher, *J. Am. Ceram. Soc.* **6** (1925) 339.

[Gli69] M.E. Glicksman, C.L. Vold, *Acta Met.* **17**, (1969) 1.

[Gre93] A.L. Greer, *Nature* **366** (1993) 303.

[Hag81] M. Hagiwara, A. Inoue, T. Masumoto, *Sci. Rep. Res. Inst. Tohoku University* **A-29** (1981) 351.

[Ham96] A.P. Hammersley, S.O. Svensson, M. Hanfland, A.N. Fitch, D. Häusetmann, *High Press. Res.* **14**, (1996) 235.

[Han76] C. O'Handley, R. Hasegawa, R. Ray, and C. P. Chou, *Appl. Phys. Lett.* **29** (1976) 330.

[Hei28] W. Heisenberg: "Zur Theorie des Ferromagnetismus", *Z. Phys.* **619** (1928).

[Her89] G. Herzer, *IEEE Trans. on Magn*. **25**, (1989) 3327.

[Her97] G. Herzer: *Handbook of magnetic materials, vol. 10*, K.H.J. Buschow, Elsevier, Amsterdam, (1997) 417-462.

[IFW] Internet: Leibniz Institute for Solid State and Materials Research Dresden, www.ifw-dresden.de, *publications.*

[Ima01] M. Imafuku, S. Sato, H. Koshiba, E. Matsubara, A. Inoue, *Scripta Mater*. **44** (2001) 2369.

[Ino82] A. Inoue, M. Hagiwara, T. Masumoto, *J. Mater. Sci.* **17** (1982) 580.

[Ino95a] A. Inoue, J. S. Gook, *Mater. Trans., JIM* **36** (1995) 1180.

[Ino95b] A. Inoue, Y. Shinohara, J. S. Gook, *Mater. Trans., JIM* **36** (1995) 1427.

[Ino97] A. Inoue, N. Nishiyama, *Mater. Sci. Eng. A* **226-228** (1997) 401.

[Ino00] A. Inoue, *Acta Mater.* **48** (2000) 279.

[Ino02] A. Inoue, B.L. Shen, *Mater. Trans.s* **43** (2002) 766.

[Ino03] A. Inoue, B. L. Shen, H. Koshiba, H. Kato, and A. R. Yavari, *Nat. Mater.* **2** (2003) 661.

[Ino04] A. Inoue, B.L. Shen, C.T. Chang, *Acta Mater.* **52** (2004) 4093.

[Ino06] A. Inoue, B.L. Shen, C.T. Chang, *Intermetallics* **14** (2006) 936.

[Kis57] H.E. Kissinger: “Reaction kinetics in differential thermal analysis”, *Anal. Chem.* **29** (1957) 1702.

[Kle60] W. Klement, R. H. Willens, P. Duwez, *Nature* **187** (1960) 869.

[Kne62] E. Kneller: *Ferromagnetismus*, Springer-Verlag Berlin, Germany, (1962).

[Kös80] U. Köster and U. Herold, *Crystallization of metallic glasses*, in *Glassy Metals I* (Springer-Verlag, Heidelberg, 1980), p. 225.

[Kur89] W. Kurz, D.J. Fisher: *Fundamentals of solidification*, Trans Tech Publications, Switzerland-Germany-UK-USA, (1989).

[Liu09] F. Liu, S. Pang, R. Li, T. Zhang, *J. Alloys Comp.* **483** (2009) 613

[Lu96] K. Lu, *Mater. Sci. Eng.* R **16** (1996) 161.

[Lu02] Z.P. Lu, C.T. Liu, *Acta Mater.* **50** (2002) 3501.

[Lu03a] Z.P. Lu, C.T. Liu, *Phys. Rev. Lett.* **91** (2003) 115505.

[Lu03b] Z.P. Lu, C.T. Liu, W.D. Porter, *Appl. Phys. Lett.* **83**, (2003) 2581.

[Lu04] Z.P. Lu, C.T. Liu, J.R. Thomson, W.D. Porter, *Phys. Rev. Lett*. **92** (2004) 245503.

[Mat01] E. Matsubara, S. Sato, M. Imafuku, T. Nakamura, H. Koshiba, A. Inoue, Y. Waseda, *Mat. Sci. Eng. A* **312** (2001) 136.

[Pau90] A. Paul: *Chemistry of glasses*, Kluwer Academic Publishers, 1990.

[Paw03] P. Pawlik, H. A. Davies, and M. R. J. Gibbs, *Appl. Phys. Lett*. **83** (2003) 2775.

[Pon04] V. Ponnambalam, S.J. Poon, *J. Mater. Res.* **19** (2004) 1320.

[Poo03] S.J. Poon, G.J. Shiflet, F.Q. Guo, V. Ponnambalam, *J. Non.Cryst. Solids* **317** (2003) 1

[Sco83] M. G. Scott, *Crystallization*, in *Amorphous metallic alloys*, edited by F. E. Luborsky (Butterworths, London, 1983), p. 144.

[She99] T. D. Shen, R. B. Schwarz, *Appl. Phys. Lett*. **75** (1999) 49.

[She02] B. L. Shen, A. Inoue, *Mater. Trans*. **43** (2002) 1235.

[She05] S. H. Sheng, C. L. Ma, S. J. Pang, T. Zhang, *Mater. Trans*. **46** (2005) 2949.

[She07] B.L. Shen, Y. Zhou, C. Chang, A. Inoue, *J. Appl. Phys.* **101** (2007) 09N101.

[Spe94] R.F. Speyer: *Thermal analysis of materials*, Marcel Dekker Inc., New York-Basel-Honk Kong, (1994).

[Sto05a] M. Stoica: *Casting and characterization of Fe-(Cr, Mo, Ga)-(P-C-B) soft magnetic bulk metallic glasses*, PhD Thesis, University of Technology, Dresden (Germany), (2005).

[Sto05b] M. Stoica, S. Roth, J. Eckert, L. Schultz, M. D. Baro, *J. Magn. Magn. Mater.* **290–291** (2005) 1480.

[Sto06] M. Stoica, K. Hajlaoui, A. Lemoulec, A.R. Yavari, *Phil. Mag. Letters* **86** (2006) 267.

[Sto09] M. Stoica, S. Kumar, S. Roth, S. Ram, J. Eckert, G. Vaughan, A.R. Yavari: *J. Alloys Comp.* **483** (2009) 632.

[Sto10a] M. Stoica, R. Li, A.R. Yavari, G. Vaughan, J. Eckert, N. Van Steenberge, D. Ruiz Romera, *J. Alloys Comp.* **504S** (2010) 123.

[Sto10b] M. Stoica, J. Das, J. Bednarčik, G. Wang, G. Vaughan, W.H. Wang, J. Eckert, *JOM* **62** (2010) 76.

[Str08] E.H. Strange, C.A. Pim: *Process of manufacuturing thin sheets, foil, strips, or ribbons of Zinc, lead, or other metal or alloy*, US Pat. 905758, (1908).

[Sur11] C. Suryanarayana, A. Inoue: *Bulk Metallic Glasses*, CRC Press, Taylor & Francis Group (2011).

[Tag13] A.H. Taghvaei, M. Stoica, K.G. Prashanth, J. Eckert, *Acta Mater.* **61** (2013) 6609.

[Tak05] A. Takeuchi, A. Inoue, *Mater. Trans. JIM* **46** (2005) 2817.

[Tur49] D. Turnbull, J.C. Fisher, *J. Chem. Phys.* **17** (1949) 71.

[Tur61] D. Turnbull, *Trans. Metall. Soc. AIME* **221**, (1961) 422.

[Tur69] D. Turnbull, *Contemp. Phys.* **10**, (1969) 473.

[Vol26] M. Vollmer, A. Weber, *Z. Phys. Chem.*, **119**, (1926) 227.

[Yav05] A.R. Yavari, A.L. Moulec, A. Inoue, N. Nishiyama, N. Lupu, E. Matsubara, W.J. Botta, G. Vaughan, M. Di Michiel, A. Kvick, *Acta Mater.* **53** (2005) 1611.

[Yos88] Y. Yoshizawa, Y.S. Oguma, K. Yamauchi", *J. Appl. Phys.* **64**, (1988) 6044.

[Zha91] T. Zhang, A. Inoue, T. Masumoto, *Mater. Trans. JIM* **32** (1991) 1005.

Acknowledgments

I wish first to express all my gratitude towards my family and especially to my wife, Liliana. She never lost her faith in this project and she sustained and encouraged me from the very beginning until the very end. Thank you, Liliana, for your trust, kindness, help, push and patience! Sincere thanks as well to my parents (unfortunately my father, Prof. Constantin Stoica, passed away far too early), they took care to set the underlying grounds of my education, fundaments without which today I would not have been here!

I am very grateful as well to my collaborators from Politehnica University of Timisoara, which in time became very close to me: Prof. Dr. Viorel Serban, Assoc. Prof. Dr. Mircea Nicoara, Assoc. Prof. Dr. Aurel Raduta and Lector Dr. Cosmin Locovei. Without their trust, help and push I would never had the courage to pursue such work.

Special thanks to my external collaborators from OCAS: Dr. Nele Van Steenberge, Dr. Daniel Ruiz Romera, Dr. Marc De Wulf, Dr. Serge Claessens. Thank you for your trust, for extremely interesting discussions and for your financial support.

The supportive atmosphere inherent to the whole group from IFW Dresden contributed essentially to the final outcome of my studies. In this context I would like to thank particularly to Prof. Dr. Jürgen Eckert, Dr. Uta Kühn, Dr. Flaviu Gostin, Dr. Sergio Scudino, Dr. Ivan Kaban, Assoc. Prof. Dr. Mariana Calin, Dr. Annett Gebert, Dr. Simon Pauly, without forgetting our technical support Sven Donath, Michael Frey, Birgit Opitz, Harald Merker- without them the master alloys, sample preparation and X-ray diffraction would have been more difficult!

During my work I had numerous collaborations with peoples from various countries and I visited other laboratories. I want to thank here especially Dr. Gavin Vaughan from ESRF Grenoble, Prof. Dr. Alain Reza Yavari and Dr. Konstantinos Georgarakis from INP Grenoble, France, as well as Assoc. Prof. Dr. Jerzy Antonowicz from Warsaw, Poland. It was and it will be always a pleasure to be in the same team for synchrotron measurements! Also, I want to thank Dr. Jozef Bednarčik from Hamburg synchrotron (DESY), who revealed and taught me many “tricks and secrets” regarding the work with synchrotron radiation.

Many other peoples should be listed here, including the temporary scientific guests and my former students. Even if their names do not appear here does not mean that I forgot them!